


國立交通大學

電子工程學系 電子研究所碩士班

碩士論文

具懸浮奈米線結構之新穎元件的  
製作與特性分析



**A Study on the Fabrication and  
Characterization of Novel Devices with  
Suspended Nanowire Structures**

研究生：許家維

指導教授：林鴻志 博士

黃調元 博士

中華民國九十九年九月

具懸浮奈米線結構之新穎元件的  
製作與特性分析

**A Study on the Fabrication and  
Characterization of Novel Devices with  
Suspended Nanowire Structures**

研究生：許家維

Student : Chia-Wei Hsu

指導教授：林鴻志 博士

Advisors : Dr. Horng-Chih Lin

黃調元 博士

Dr. Tiao-Yuan Huang



國立交通大學  
電子工程學系 電子研究所碩士班  
碩士論文

A Thesis

Submitted to Department of Electronics Engineering & Institute of Electronics

College of Electrical and Computer Engineering

National Chiao-Tung University

in Partial Fulfillment of the Requirements

for the Degree of

Master of Science

in

Electronics Engineering

September 2010

Hsinchu, Taiwan, Republic of China

中華民國九十九年九月

# 具懸浮奈米線結構之新穎元件的 製作與特性分析

研究生：許家維

指導教授：林鴻志 博士

黃調元 博士

國立交通大學

電子工程學系 電子研究所碩士班

## 摘要

在本論文中，我們成功地製作兩種新穎的元件結構，分別為具懸浮奈米線通道之薄膜電晶體(suspended-NW-channel TFTs)、與垂直式金氧半場效電晶體(VMOS)。其中，前者的懸浮奈米線通道、與後者的邊襯(sidewall spacer)閘極電極皆利用一簡單、低成本的反應式離子蝕刻(RIE)技術製作完成。此外，在後者的製作過程中，我們只使用兩個主要的微影光罩，以達到進一步降低成本的目的。

具懸浮奈米線通道之薄膜電晶體展現了極低的次臨界擺幅(subthreshold slope) (35 mV/dec.)、與相當大的遲滯窗口(hysteresis window) (3.7 V)。我們發現擺入(pull-in)汲極電流限制效應、汲極電流的似暫態行為、非對稱低次臨界擺幅與遲滯窗口打開的特性。除此之外，我們還發現，隨著幾何結構尺寸與閘極電壓掃描速率的改變，遲滯窗口、擺入電壓( $V_{pi}$ )、擺出電壓( $V_{po}$ )、擺入之低次臨界擺幅(S.S.F)與擺出之次臨界擺幅(S.S.R)都有特定的變化趨勢。最後，依據以上所有的發現，

我們提出一個觀念性的模型，用以描述元件操作時靜電力、彈性回復力與表面黏滯力之間的交互作用。

另一方面，當操作在順向操作模式時，垂直式金氧半場效電晶體展現了良好的開關電流比( $10^6$ )與可接受的抗貫穿能力(anti-punch through ability)。此外，我們也發現一個有趣的兩段式開啟特性，並且解釋為凸邊角效應的結果。



# **A Study on the Fabrication and Characterization of Novel Devices with Suspended Nanowire Structures**

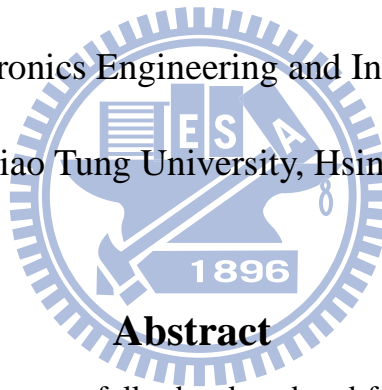
Student : Chia-Wei Hsu

Advisors : Dr. Horng-Chih Lin

Dr. Tiao-Yuan Huang

Department of Electronics Engineering and Institute of Electronics

National Chiao Tung University, Hsinchu, Taiwan



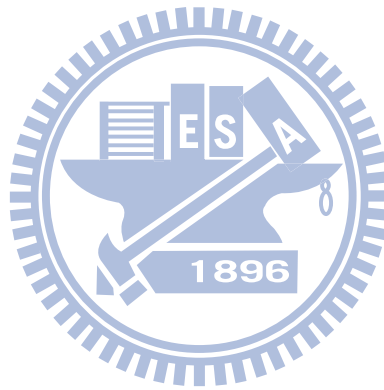
## **Abstract**

In this thesis, we have successfully developed and fabricated two kinds of novel device structures, including suspended-nanowire (NW)-channel thin film transistors (TFTs) and vertical metal-oxide-semiconductor field-effect transistors (VMOS). The suspended NW channels in suspended-NW-channel TFTs and the sidewall spacer gate electrode in VMOS are formed by a simple and low-cost reactive ion etch (RIE) technique. Especially, in VMOS, further cost down could be achieved as only two main photolithographic reticles are needed through the process.

The suspended-NW-channel TFTs with ultra-low subthreshold swing (S.S.) (35 mV/dec.) and considerable hysteresis window (3.7 V) are demonstrated. The limited pull-in drain current ( $I_D$ ), the transient-like behavior in  $I_D$ , the asymmetric S.S., and the

hysteresis window opening characteristics are also observed. Besides, the specific trends in hysteresis window,  $V_{pi}$ ,  $V_{po}$ ,  $S.S.F$  and  $S.S.R$  with the change of geometric structure dimensions and  $V_G$  sweeping rate are found and analyzed. Finally, based on all of the above observations, a conceptual model illustrating the interaction between the electrostatic force, the elastic recovery force and the surface adhesion forces during device operation is proposed.

On the other hand, the VMOS devices exhibit a good on-off ratio of  $10^6$  and acceptable anti-punch through ability. In addition, an interesting two-step turn-on characteristic is also observed and explained by the convex corner effect.



# Acknowledgment

走到這裡，我在這個實驗室已經待了整整 26 個月了，出入 NDL 也早已屆滿一週年，題目更是換了兩次。經歷了這麼多事情，一路上多虧許多貴人的相助，我才能夠走完這顛頗的碩士生涯。

首先，特別感謝指導教授 林鴻志 教授、黃調元 教授。不管是在學術成就的追求，或者實驗態度的分享，點點滴滴都帶給我許多的啟發。特別是在實驗不順利時，林老師適時的提醒、指正，讓我少走了許多冤枉路，而妙語如珠的黃老師更是讓壓力瞬間減少許多。謝謝你們。

當然 ADTL 的伙伴們，我是一定不會忘記你們的。感謝蔡子儀學長、蘇俊榮學長、徐行徽學長、林哲民學長、陳威臣學長、林政頤學長以及李克慧學姐，在實驗的設計、結果的分析都給我很大的幫助與指導。另外，在實驗進度捉襟見肘時、機台狀況不穩時，及時的建議與安慰都讓我倍感溫馨。不能不提的是郭嘉豪學長。老實說，我這一年多來的實驗並不怎麼順利，多虧你一路的幫忙才讓我能夠漸漸步上軌道，但是也很抱歉這一年來我並沒有完成既定的目標，反而讓你白白承受了不少壓力，雖然說什麼都沒辦法表達我的感謝，還是老話一句「謝謝」。631 的同伴們，有你們的陪伴，我才能度過這跌跌撞撞的 14 個月。每次實驗遇到問題，多虧你們的打氣讓我有繼續下去的動力；你們持續努力的精神更是我所仿效的楷模。感謝簡敏峰、羅正璋、劉禹伶、林庭輔、陳冠宇、陳冠智，你們讓枯燥的實驗有了火花；你們讓無聊的量測變得有趣；你們讓沈寂的空氣多了生氣。謝謝你們。

另外，感謝 NDL 與 NFC 的一切。實驗機台讓論文終究可以完成，操作小姐與工程師的配合，更讓進度得以前進。感謝 NDL 周家如小姐、范庭瑋小姐、魏耘婕小姐、林婉貞小姐、陳琇芝小姐、徐台鳳小姐、趙子綾小姐、李春杏小姐、蕭明娟小姐無數次的通融與協助，讓延宕的實驗進度得以加速。謝謝你們。

最後，感謝我的父母：許隆昌 先生、劉惠珍 女士，你們無私的付出讓我可以無後顧之憂的向前邁進；感謝哥哥，讓我的求學路上感受到親情的溫暖；感謝室友 Jefferson、蠻頭、砲哥，無限的包容與體諒，以及毫無怨言的聽我吐苦水、講心事，讓我有依靠的感覺；更要感謝小企鵝，妳的陪伴、分享與相互扶持是我最大的福份。謝謝你們。

此論文，謹獻給所有曾經幫助我、鼓勵我，以及我所敬重、珍惜的師長、朋友們。謝謝你們。

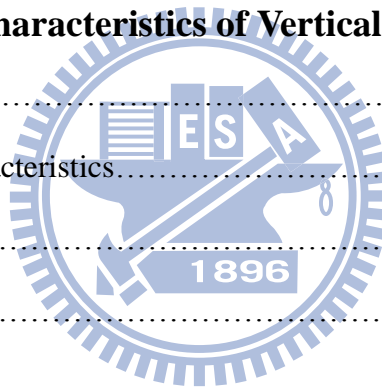
許家維  
誌於 風城交大  
2010 年 9 月

# Contents

<b>Abstract (Chinese)</b> .....	<b>i</b>
<b>Abstract (English)</b> .....	<b>iii</b>
<b>Acknowledgment (Chinese)</b> .....	<b>v</b>
<b>Contents</b> .....	<b>vi</b>
<b>List of Figure Captions</b> .....	<b>viii</b>
<b>List of Table Captions</b> .....	<b>xiv</b>
<b>Chapter 1 Introduction</b> .....	<b>1</b>
1-1 Overview of Vertical MOSFETs.....	1
1-2 Overview of Low Subthreshold-Swing Devices.....	3
1-2-1 Impact-ionization MOS (I-MOS).....	4
1-2-2 Tunneling FET (T-FET).....	6
1-2-3 Suspended-gate MOSFET (SG-MOSFET).....	7
1-2-4 Suspended-NW-channel Device.....	9
1-3 Motivation.....	10
1-4 Organization of this Thesis.....	11
<b>Chapter 2 Device Fabrication</b> .....	<b>12</b>
2-1 Device Structure and Process Flow of Suspended-NW-Channel TFTs.....	12
2-2 Device Structure and Process Flow of Vertical MOSFETs.....	13
2-3 Measurement Setup and Electrical Characterization.....	16
Table Captions.....	18



<b>Chapter 3 Electrical Characteristics of Suspended-NW-channel TFTs.</b>	<b>19</b>
3-1 Basic Electrical Characteristics.....	19
3-2 Hysteresis Phenomenon.....	20
3-2-1 Basic Hysteresis Characteristics.....	21
3-2-2 Effects of Structure Dimension.....	24
3-2-3 Effects of $V_G$ Sweeping Rate.....	27
3-2-4 Summary.....	28
3-3 Operation Mechanism.....	28
Table Captions.....	31
<b>Chapter 4 Electrical Characteristics of Vertical MOSFETs.....</b>	<b>32</b>
4-1 Background.....	32
4-2 Basic Electrical Characteristics.....	33
4-3 Discussion.....	35
Table Captions.....	37
<b>Chapter 5 Conclusion and Future Work.....</b>	<b>38</b>
5-1 Conclusion.....	38
5-2 Future Work.....	40
References.....	42
Figure Captions.....	46
Vita.....	87
Publication List.....	88



# List of Figure Captions

## Chapter 1

Fig. 1.1.	The progressive growth of Intel’s CPU transistor counts per microprocessor [3]. .....	46
Fig. 1.2.	The CPU transistor count and feature size trends [4]. .....	47
Fig. 1.3.	Evolution of device feature size and the resolution capability of exposure tools with various exposure wavelength [6]. .....	47
Fig. 1.4.	Three major structures for the design of vertical MOSFETs, based on (a) solid source diffusion, (b) epitaxial and (c) implantation, respectively. ....	48
Fig. 1.5.	The conduction mechanism of drain current at low drain bias [14]. .....	49
Fig. 1.6.	(a) Basic device structure and (b) band diagram in the ON/OFF state of the n-channel I-MOS [16]. .....	49
Fig. 1.7.	Carrier distribution in space- and energy-scale in a device with 50 nm-long high-field region obtained from 1D Monte-Carlo simulation, superimposed on the energy band diagram of the simulated structure. (a) One electron with low energy is injected from the left end of the high-field region at random time $\tau_1$ . (b) The first carrier then initiates the impact ionization avalanche, and carrier number multiplies. However, with initially small number of carriers in the device, a strong random fluctuation is expected, until a reasonable number of carriers are present and overcome the randomness in carrier multiplication. (c) The carrier multiplication continues at an average rate [23]. .....	50
Fig. 1.8.	Simulated and experimental source-drain breakdown voltage, $V_{Br}$ , versus gated channel length, $L_G$ , curves for both n-type and p-type I-MOS [24]. The difference between n-type and p-type I-MOS is originated from dopant diffusion. The p-type dopant usually diffuses more extensively than the n-type one. ....	50
Fig. 1.9.	Schematic view of T-FFT device structure. ....	51
Fig. 1.10.	Energy band diagram for gate-controlled BTBT in T-FET with 100 nm channel length [18]. .....	51

Fig. 1.11.	(a) Typical 3D structure of SG-MOSFET with anchors at both ends of SG suspended over the gate oxide layer [29]. (b) An equivalent electrical circuit of SG-MOSFET, <i>i.e.</i> , a combination of electrostatically actuated NEMS switch and inversion-mode MOSFET [30].	52
Fig. 1.12.	The 2D cross-section of SG-MOSFET. The SG-MOSFET is controlled by two competing forces, electrostatic force and elastic force [29].	53
Fig. 1.13.	The operation principle of SG-MOSFET. (a) As $V_G < V_{pi}$ , the electrostatic force is balanced by elastic force only. (b) As $V_G > V_{pi}$ , the electrostatic force overcomes the elastic force and the SG will be connected with gate oxide layer. There is no air gap anymore. [29].	53
Fig. 1.14.	Typical $I_D$ - $V_G$ characteristics of SG-MOSFET for $V_D = 50$ mV. Region 1 represents the weak inversion regime and Region 2 represents the electromechanical pull-in of mobile gate after reaching the non-equilibrium point. (Symbols: measurement results; Solid Line: analytical simulation). [30]	54
Fig. 1.15.	The mechanical hysteresis cycle of an SG-MOSFET [30].	54
Fig. 1.16.	The major fabrication steps of the suspended poly-Si NW channel device with side-gated configuration [20]. (a) Gate definition. (b) Gate dielectric deposition, poly-Si channel deposition and S/D implantation. (c) S/D definition. (d) Air gap formation.	55
Fig. 1.17.	The basic electrical characteristics of suspended NW channel device [20].	55

## Chapter 2

Fig. 2.1.	Key fabrication steps of suspended NW channel TFTs. (a) The top view of the suspended NW channel TFTs. (b) Formation of <i>in-situ</i> doped poly gate. (c) Deposition of silicon nitride, TEOS and $\alpha$ -Si channel with SPC. (d) Formation of S/D regions and sidewall spacer NW channels by RIE. (e) Channel region definition and S/D implantation. (f) Air gap formation. Note that, figures in (b) to (f) are cross-sectional view from the cutline $\overline{AB}$ in (a).	56
Fig. 2.2.	The cross-sectional TEM images of suspended NW channel from the cutline $\overline{AB}$ indicated in Fig. 2.1 (a) with different over-etch time. (a) 28	

	sec. (b) 22 sec. ....	57
Fig. 2.3.	The top view of suspended-NW-channel TFT taken by SEM. ....	58
Fig. 2.4.	Key fabrication steps of SG-VMOS devices. (a) The top view of SG-VMOS device. (b) Vertical channel patterning by anisotropic plasma etching. (c) Re-oxidation and tilt sidewall channel implantation. (d) Formation of dry oxide, silicon nitride and TEOS gate dielectric stack and <i>in-situ</i> doped poly gate. (e) Sidewall spacer gate electrode formation by RIE. (f) Removal of exposed TEOS layer by DHF wet etching and S/D implantation. (g) Air gap formation. Note that, figures in (b) to (g) are cross-sectional view from the cutline $\overline{AB}$ in (a). ....	59
Fig. 2.5.	The top view of patterns in SEM bar region (a) and device region (b) after vertical channel definition taken by in-line SEM. The physical channel length is 0.5 $\mu\text{m}$ . ....	60
Fig. 2.6.	The simulated total doping concentration profile in our SG-VMOS with 50 nm sacrificial TEOS layer. The device channel length is 0.5 $\mu\text{m}$ . (a) Along cutline $\overline{AB}$ shown in Fig. 2.1. (b) Along y direction with $x = -0.24 \mu\text{m}$ . (c) Along x direction with $y = 0.57 \mu\text{m}$ . ....	61
Fig. 2.7.	The ion implantation projection range (a) and standard deviation of projection range (b) of various common dopants in crystalline silicon tilted and rotated to simulate a random direction [39]. ....	62
Fig. 2.8.	The in-line SEM images of the device patterns after sidewall spacer gate definition and DHF wet etching. (a) and (b) show the right-hand side and left-hand side images of the device structure, respectively. The device channel length is 0.5 $\mu\text{m}$ . ....	63
Fig. 2.9.	The in-line SEM images of the patterns in the device region after sidewall spacer gate definition and DHF wet etching. (a) and (b) show the right-hand side and left-hand side images of the device structure, respectively. The device channel length is 1 $\mu\text{m}$ . ....	63

### Chapter 3

Fig. 3.1.	Figure 3.1. $I_D$ - $V_G$ curves of (a) conventional TFT and (b) suspended-NW-channel TFT. ....	64
Fig. 3.2.	The plot of S.S. versus $I_D$ for the devices with three different structures,	

	<i>i.e.</i> , without sacrificial TEOS layer, before stripping the TEOS layer and after stripping the TEOS layer. ....	65
Fig. 3.3.	The electrical parameters of a suspended-NW-channel TFT including the pull-in voltage ( $V_{pi}$ ), the pull-out voltage ( $V_{po}$ ) and the S.S. under the forward and reverse sweeping measurements. ....	65
Fig. 3.4.	Schematic showing the definition of structural parameters of the suspended-NW-channel TFTs including the channel length and the S/D extension length. ....	66
Fig. 3.5.	The hysteresis characteristics of a suspended-NW-channel TFT under consecutive forward and reverse sweeping measurements. ....	66
Fig. 3.6.	The plot of S.S. versus $I_D$ for a suspended-NW-channel TFT under consecutive forward and reverse sweeping measurements. ....	67
Fig. 3.7.	The endurance characteristics for a suspended-NW-channel TFT under consecutive cycling measurements. ....	67
Fig. 3.8.	The hysteresis curves of a suspended-NW-channel TFT measured before ( <i>i.e.</i> , as fresh) and after 120 times cyclings. ....	68
Fig. 3.9.	The hysteresis curves of the suspended-NW-channel TFTs with channel length of 0.4 $\mu\text{m}$ , 1 $\mu\text{m}$ and 5 $\mu\text{m}$ , respectively. ....	68
Fig. 3.10.	The hysteresis curves of the suspended-NW-channel TFTs with S/D extension length of 0.25 $\mu\text{m}$ and 0.5 $\mu\text{m}$ , respectively. ....	69
Fig. 3.11.	The plot of hysteresis window versus channel length for the suspended-NW-channel TFTs with S/D extension length of 0.25 $\mu\text{m}$ and 0.5 $\mu\text{m}$ , respectively. ....	69
Fig. 3.12.	The plot of $V_{pi}$ and $V_{po}$ versus channel length for the suspended-NW-channel TFTs with S/D extension length of 0.25 $\mu\text{m}$ and 0.5 $\mu\text{m}$ , respectively. ....	70
Fig. 3.13.	The plot of $S.S._F$ and $S.S._R$ versus channel length for the suspended-NW-channel TFTs with S/D extension length of 0.25 $\mu\text{m}$ and 0.5 $\mu\text{m}$ , respectively. ....	70
Fig. 3.14.	The hysteresis curves of the suspended-NW-channel TFTs with two different NW thicknesses. ....	71
Fig. 3.15.	The plot of hysteresis window versus channel length for the suspended-NW-channel TFTs with two different NW thicknesses. ....	71

Fig. 3.16.	The plot of $V_{pi}$ and $V_{po}$ versus channel length for the suspended-NW-channel TFTs with two different NW thicknesses. ....	72
Fig. 3.17.	The plot of $S.S._F$ and $S.S._R$ versus channel length for the suspended-NW-channel TFTs with two different NW thicknesses. ....	72
Fig. 3.18.	The hysteresis curves of the suspended-NW-channel TFTs with air gap thickness of 100 nm, 80 nm, 30 nm and 10 nm, respectively. ....	73
Fig. 3.19.	The plot of hysteresis window versus air gap thickness for the suspended-NW-channel TFTs. ....	73
Fig. 3.20.	The plot of $V_{pi}$ and $V_{po}$ versus air gap thickness for the suspended-NW-channel TFTs. ....	74
Fig. 3.21.	The plot of $S.S._F$ and $S.S._R$ versus air gap thickness for the suspended-NW-channel TFTs. ....	74
Fig. 3.22.	The hysteresis curves of the suspended-NW-channel TFTs operated at different sweeping speed by modulating the increment of $V_G$ per step. ....	75
Fig. 3.23.	The plot of hysteresis window versus the increment of $V_G$ per step during measurements for the suspended-NW-channel TFTs. ....	75
Fig. 3.24.	The plot of $V_{pi}$ and $V_{po}$ versus the increment of $V_G$ per step during measurements for the suspended-NW-channel TFTs. ....	76
Fig. 3.25.	The plot of $S.S._F$ and $S.S._R$ versus the increment of $V_G$ per step during measurements for the suspended-NW-channel TFTs. ....	76
Fig. 3.26.	Various operation states of the suspended NW channels for the suspended-NW-channel TFTs. (a) The NW channels are suspended and separated from the gate with the air gap. (b) As $V_G = V_{pi}$ , the central region of the NW channels begins to contact with the gate stack. (c) As $V_G$ is further increased to turn the device into the ON state, most of the NW channels are in contact with the gate stack. ....	77
Fig. 3.27.	Various operation states of the suspended-NW-channel TFTs. A: The NW channels are suspended. B: The central region of NW channels begins to contact with the gate stack. C: Portion of the NW channels in contact with the gate stack gradually increases. D: ON state. E: The surface adhesion forces maintain the contact of NW channels with the gate stack, and the drain currents remains relatively high. F: The NW channels gradually detach from the gate stack. ....	78

## Chapter 4

Fig. 4.1.	The bias configurations of our VMOS devices with no TEOS layer under the forward and reverse operation modes, respectively. ....	79
Fig. 4.2.	$I_D$ - $V_G$ curves of VMOS devices under forward operation mode with nominal channel length of (a) 0.5 $\mu\text{m}$ and (b) 1 $\mu\text{m}$ . ....	80
Fig. 4.3.	The top-view of the VMOS with convex corner regions circled. ....	81
Fig. 4.4.	(a) The equivalent circuit of VMOS with two different MOSFETs in shunt. The device 1 is with a lower $V_{th}$ and better S.S. than device 2. (b) The corresponding $I_D$ - $V_G$ curves of these two shunted MOSFETs. (c) $I_D$ - $V_G$ curves of the equivalent shunt circuit. ....	82
Fig. 4.5.	Output characteristics of the VMOS operated under forward mode with nominal channel length of (a) 0.5 $\mu\text{m}$ and (b) 1 $\mu\text{m}$ . ....	73
Fig. 4.6.	$I_D$ - $V_G$ curves of VMOS devices under forward and reverse operation modes with nominal channel length of (a) 0.5 $\mu\text{m}$ and (b) 1 $\mu\text{m}$ . ....	84
Fig. 4.7.	Output characteristics of the VMOS operated under the forward and reverse modes with nominal channel length of (a) 0.5 $\mu\text{m}$ and (b) 1 $\mu\text{m}$ . ...	85

## Chapter 5

Fig. 5.1.	The top-view of modified SG-VMOS device layout. ....	86
Fig. 5.2.	Schematic view of modified SG-VMOS device structure with epitaxial growth fabrication technique. ....	86

# List of Table Captions

## Chapter 2

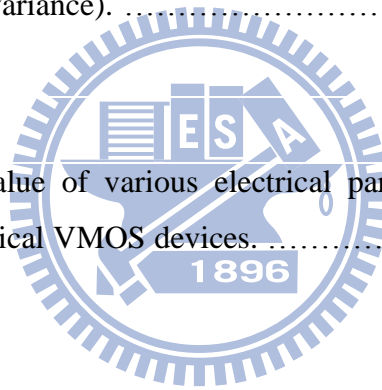
Table 2.1.	Split table for suspended-NW-channel TFTs. ....	18
Table 2.2.	Split table for SG-VMOS. ....	18

## Chapter 3

Table 3.1.	Comparisons of electrical parameters between the conventional NW TFTs and suspended-NW-channel TFTs. ....	31
Table 3.2.	Variance trend of electrical parameters with an change in structural parameters and $V_G$ sweeping rate. (Symbols: $\uparrow$ : increasing, $\downarrow$ : decreasing, $-$ : no obvious variance). ....	31

## Chapter 4

Table 4.1.	The average value of various electrical parameters extracted from 32 nominally identical VMOS devices. ....	37
------------	---	----





# ***Chapter 1***

---

## ***Introduction***

### **1-1 Overview of Vertical MOSFETs**

For decades, very-large-scale-integration (VLSI) metal-oxide-semiconductor field effect transistors (MOSFETs) are being continuously scaled down in critical dimensions (CDs) due to the needs of higher package density, higher device operation speed, better integrated circuit (IC) functionality and lower fabrication cost per unit. In 1965, the Intel's co-founder Gordon E. Moore observed and predicted, which later became the famous Moore's Law, "The complexity for minimum component costs has increased at a rate of roughly a factor of two per year [1]." The combination of Moore's Law and Dennard's scaling methodology [2] has provided industry with many generations of smaller, faster and higher performance microprocessors. According to the announcements from Intel Corporation, the number of transistors on microprocessor chips has grown explosively fast and is rising above the billion transistor level in recent years, as shown in Fig. 1.1 [3]. Figure 1.2 shows the central processing unit (CPU) transistor count and feature size trends [4].

In order to keep pace with the Moore's Law, conventional planar MOSFETs inevitably faces a lot of challenges, such as high leakage current, severe short channel effects (SCEs), threshold voltage adjustment and other parasitic issues. In addition to all the issues stated above, there is one intrinsic problem people have to overcome first,

that is the limitation of photolithography. According to the Rayleigh's theory, the resolution of a lithography system is proportional to the wavelength of light [5]. In other words, the shorter the light wavelength is, the higher resolution of lithography system is. Figure 1.3 shows device trends and resolution performance of exposure tools from 1970 to 2005 and beyond [6]. Starting with g-line of wavelength 436 nm, exposure tools have been shifting to shorter exposure wavelengths which agree with Rayleigh's theory. In past decades, many researchers have dedicated themselves to developing new lithographic techniques in order to succeed the old one for continuous scaling. Nonetheless, to this date, advanced or next generation photolithography, namely, the extreme UV (EUV) system, is too expensive and not mature yet [7]. Hence, some of the research activities have been shifted to finding alternative routes for maintaining the scaling trend. One of such brilliant ideas is the transformation of device structures, such as vertical channel MOSFETs, *i.e.*, vertical MOS (VMOS), to avoid the limitation of photolithography technology [8-11].

The major advantage of VMOS is that short channel length or small memory cell area could be achieved and well defined sub-lithographically by the film thickness. The reduction in reliance on advanced lithographic tools makes VMOS a promising candidate for future device structure constructed on a chip, whether in memory or logic application. Some research also had pointed out that the VMOS had an area advantage of 2.4 fold over equivalent planar MOS device [9]. In addition, VMOS combined with double gate or gate-all-around (GAA) structure could lead to a better gate control ability over the planar counterparts [12].

Figure 1.4 shows three main concepts for the design of vertical MOSFETs. In Figs. 1.4 (a) and (b), VMOS based on outdiffusion of dopants from deposited layers and on epitaxial layers are shown. However, in these approaches the fabrication

processes become much more complex due to the needs of complicated layer sequences. Another shortcoming for the structure shown in Fig. 1.4 (b) is the lack of substrate body contact to avoid kink effects. In contrast, different from the former two approaches, the one shown in Fig. 1.4 (c) based on implantation has some unique advantages. First, it has a simpler process comparable to planar device. Besides, substrate body contact is available to avoid floating body effect.

## 1-2 Overview of Low Subthreshold-Swing Devices

As mentioned above, the IC development trend follows the Moore's Law. Hence, the power supply voltage should go down with the scaling of CDs due to the reliability and power consumption issues. Under this situation, a device with a low subthreshold swing (S.S.) is imperative to sustain a high on-state current ( $I_{on}$ ) with an acceptable low off-state current ( $I_{off}$ ). Furthermore, from the point of view of power consumption, it is also very important to improve S.S. In modern IC chips, there are millions of devices in a single circuit. Such a huge IC chip implies an extremely large off-state current may exist, resulting in serious concern with power wasting [13].

However, for conventional planar MOS transistors, the S.S. encounters some physical limitation. The following equation describes the mathematical definition and analytical form of S.S. based on well-established MOS theory,

$$S.S. \equiv \frac{\partial V_G}{\partial \log I_D} \approx 2.3 \frac{kT}{q} \frac{\partial V_G}{\partial \psi_s} = 2.3 \frac{kT}{q} \left( 1 + \frac{C_d}{C_{ox}} \right), \quad (\text{Eq. 1-1})$$

where  $V_G$  is the gate voltage,  $I_D$  is the drain current,  $k$  is the Boltzmann factor,  $T$  is the temperature,  $q$  is the quantity of electric charge,  $\psi_s$  is the surface potential of semiconductor substrate,  $C_d$  is the depletion capacitance, and  $C_{ox}$  is the gate oxide

capacitance [14].

It is well known that there are two main drain current ( $I_D$ ) conduction mechanisms in MOSFETs, namely, diffusion and drift [15]. As we can see from Fig. 1.5 [14], in the subthreshold regime, the diffusion one dominates. In this regime, inversion carriers at the source side may overcome the potential barrier between source and channel region and then diffuse to the drain side. Moreover, the number of inversion carriers that could overcome the barrier and involve in the following process are limited by a thermodynamic factor " $\frac{kT}{q}$ " originated from Fermi-Dirac distribution [15]. Based on this conduction mechanism, the subthreshold current is exponentially proportional to the gate voltage ( $V_G$ ) which is certainly consistent with the above equation. In ideal case, at room temperature, the S.S. of conventional planar MOSFETs cannot be lower than 60 mV/decade.

In recent studies, some novel devices structure have been proposed to achieve a sub-60 mV/decade S.S., such as impact-ionization MOS (I-MOS) devices [16-17], tunneling FET (T-FET) [18], suspended-gate MOSFET (SG-MOSFET) [19] and suspended-nanowire (NW)-channel devices [20-22]. In the following part of this section, these devices are briefly reviewed.

### **1-2-1 Impact-ionization MOS (I-MOS)**

One of the interesting ultra-low S.S. device structures is impact-ionization MOS, denoted as I-MOS, and its corresponding band diagrams in ON/OFF operation states are shown in Fig. 1.6 [16]. As we could observe from Fig. 1.6, there are three major differences between I-MOS and conventional MOSFETs. First, the doping types in source and drain region are opposite for I-MOS. Second, the conduction channel is essentially intrinsic. Third, for the channel in I-MOS, there are two electrically

different regions, gated and non-gated region.

The operation principle of I-MOS is based on the impact ionization mechanism. At the OFF state, the gate bias is lower than threshold voltage and the leakage current is dominated by the reverse current of the P-I-N diode. As the gate bias is higher than threshold voltage, I-MOS is operated at ON state. The gate bias lowers the potential level in the gated region of channel and develops a high-field junction near the source side, as shown in Fig. 1.6 (b). At this moment, the electrons injecting from source side would obtain enough energy to trigger the impact ionization process and lead to avalanche breakdown. Since the switch mechanism of I-MOS is not dominated by p-n junction barrier lowering, the S.S. could theoretically be reduced to below 60 mV/decade.

However, there exist some intrinsic issues for I-MOS. One is about time delay. Figure 1.7 shows the whole process for carrier multiplication in I-MOS from OFF state to ON state [23]. From this figure, we could comprehend that it indeed requires certain amount of time for device to fully turn on. And this time delay is related to the number of initial carriers at OFF state which is proportional to OFF state current level. The lower OFF state current level implies less initial carriers and results in longer time delay for carrier multiplication and turning on of the device. Therefore, the time delay for an I-MOS would become an obstacle for high speed dynamic switch application.

The other critical issue for I-MOS is non-scalable operation voltage. Figure 1.8 shows the source-drain breakdown voltage,  $V_{Br}$ , versus gated channel length,  $L_G$ , for both n-type and p-type I-MOS [24]. For long-channel devices, the  $V_{Br}$  decreases linearly with  $L_G$ . But as  $L_G$  shrinks to 50 nm or shorter,  $V_{Br}$  becomes a constant and do not vary with  $L_G$ . In order to explain this phenomenon, we need to know the key competing factors influencing the impact ionization probability, namely, the electrical

ionization boundary and ionization coefficients. For long-channel devices, as  $L_G$  shrinks, the exponentially increase in ionization coefficients due to the rising of field strength is predominant over the linearly decreased boundary and causes  $V_{Br}$  to fall with reducing  $L_G$ . In the case of short-channel devices, however, free carriers do not have enough space to generate a sufficient number of impact ionization events to trigger breakdown. Hence, the only way for effectively increasing the average carrier energy is to increase the bias. Some simulation results have declared that  $V_{Br}$  may bounce back as  $L_G$  is shorter than 20 nm [24]. The concern is that I-MOS probably loses its transistor function as the channel length is scaled to such ultra-short dimension.

### 1-2-2 Tunneling FET (T-FET)

The device structures for I-MOS and T-FET are similar, both with a reverse biased P-I-N diode structure. For T-FET, the intrinsic channel is completely overlapped by the gate, however, so there is no non-gated channel region. Figure 1.9 shows a schematic view of T-FET.

Contrary to the I-MOS which uses the impact ionization as the current control mechanism, the major conduction process for on-state operation of T-FET is gate-controlled band-to-band-tunneling (BTBT) at the source side. The surface tunnel junction is at or near the cross-point of gate oxide/channel/source region. Figure 1.10 shows the energy band diagram of T-FET operated at ON (dashed line) and OFF (solid line) states [18]. With sufficiently high positive gate bias, so called n-type T-FET operation, the potential in the channel region will be pulled downward, electrons will tunnel from the valence band of  $p^+$  source region to the conduction band in the channel and flow to the  $n^+$  drain region. Similarly, as gate bias is sufficiently negative, the

T-FET will operate at p-type mode and the surface tunnel junction is shifted from  $p^+$  side to  $n^+$  side. At this time, the potential in the channel region will be pulled upward, electrons will tunnel from the valence band in the channel to the conduction band of  $n^+$  doped region (drain) and the generated holes will flow to the  $p^+$  doped region (source). This is for p-type T-FET operation, and highlights the ambipolar operation capability of the T-FET device. For the OFF state when the gate voltage is in the intermediate value between the p- and n-type operations so the surface band bending of the channel is not significant, due to the nature of intrinsic substrate, the field strength in the channel region is weak and thus a wide tunneling barrier is formed for both holes and electrons, as shown in Fig.1.10. The wide tunneling barrier limits not only direct tunneling but also thermal emission, making it difficult for electrons to move from the  $p^+$  region to the  $n^+$  region and therefore a low leakage current than conventional MOSFETs.

Simulation results show that T-FET can be scaled to at least 20 nm channel length with a slightly increased leakage current [25]. Moreover, the tunneling effect and the velocity overshoot may enhance the operation speed. However, the limited drive current density of T-FET becomes the biggest problem for its future application, owing to the fact that the depth of the surface tunneling junction is in the range of 10 nm or below [25]. There are some possible methods that could relieve this drawback, such as using higher source doping concentration, thinner gate oxide, more abrupt doping profile, and SiGe/Ge material [26-28].

### **1-2-3 Suspended-gate MOSFET (SG-MOSFET)**

Another kind of low-subthreshold swing device is the SG-MOSFET. A typical 3D structure of SG-MOSFET is shown in Fig. 1.11(a), with anchors on both ends of the

gate which is suspended over the gate oxide layer [29]. The major difference between regular MOSFET and SG-MOSFET is that the latter has an air gap between the suspended gate (SG) and real gate oxide layer. Equivalently, it could be viewed as a combination of an electrostatically actuated nanoelectromechanical system (NEMS) switch and an inversion-mode MOSFET [29]. An equivalent electrical circuit is shown in Fig. 1.11(b).

Next, we use Fig. 1.12 and Fig. 1.13 to illustrate the operation principle of SG-MOSFET. Because of the low dielectric constant of air gap and thus large effective oxide thickness (EOT), the SG-MOSFET has an extremely low gate leakage current as the transistor is operated at OFF state. When we apply a positive gate bias (for n-type SG-MOSFET) and increase it gradually, a positive charge will gradually build up in the gate electrode, and, for charge neutrality, there are also some negative charges induced on the substrate surface. Such a charge distribution forms an attractive electrostatic force between them which tends to pull the gate toward the gate oxide layer, as shown in Fig. 1.13(a), resulting in a narrowing of air gap thickness. One particular feature of the SG-MOSFET is that air-gap reduction provides a non-constant increment of gate capacitance with  $V_G$ , so that  $I_D$  increases super-exponentially in weak inversion regime [30]. A typical  $I_D$ - $V_G$  characteristic of n-type SG-MOSFET for  $V_D = 50$  mV is shown in Fig. 1.14. Note that there is an intrinsic elastic force for each material that may balance such an electrostatic force. Owing to this elastic force, SG will not connect with the channel until the electrostatic force becomes larger than some critical value. This critical value in gate voltage bias is called pull-in voltage ( $V_{pi}$ ). As the gate bias is larger than  $V_{pi}$ , the electrostatic force overcomes the elastic one, and the SG will collapse onto the gate oxide layer, and an abrupt increase of drain current happens due to the increase of gate capacitance and the lowering of threshold voltage



[31], as shown in Fig. 1.13(b). Another outstanding feature of SG-MOSFET is its mechanical dynamic threshold voltage: high in the pull-in state and low in the pull-out state leading to a mechanical hysteresis phenomenon as shown in Fig. 1.15 [30].

These interesting behaviors of SG-MOSFET make it attractive for future device structure. Many researchers have worked on it and tried to apply it to many different areas, such as MEMS [19], memories [19, 30] and sensors [32-34].

#### **1-2-4 Suspended-NW-channel Device**

In the last part of this section, we introduce the suspended-NW-channel devices which were originally proposed by our group, Advanced Device Technology Laboratory (ADTL), at National Chiao-Tung University (NCTU). As shown in Fig. 1.16 [20], the fabrication process is simple, low-cost and compatible with nowadays CMOS technologies, compared with the three previously mentioned low-subthreshold swing devices because no advanced lithography tools or processes are involved.

The basic device structure of suspended-NW-channel devices, shown in Fig. 1.16 (d) [20], and the operation principle are similar to the SG-MOSFETs [22]. Both of them are with a suspended object over the air gap and operated mainly by the competition of electrostatic force and elastic force which are modulated by the gate bias exerted on the suspended object. However, the electrical characteristics are slightly different from the SG-MOSFETs [20-22], shown in Fig. 1.17 [20]. For example, the abrupt transition between ON and OFF states is not so straightforward in the suspended NW channel devices [20]. The structural differences in terms of the composition and dimensions of the suspended object are postulated to be the causes for the above disparity. Nevertheless, the suspended-NW-channel devices appear to be a promising idea. The major advantage includes its simple, self-aligned and gate-first

process. Besides, the suspended-NW-channel devices can be formed with sub-100 nm air gap simply by a buffered oxide etchant (BOE) wet etching step. Such a thin air gap is conducive to further scaling of the operation voltage.

### **1-3 Motivation**

As we have learned from previous sections, issues in both the CD scaling and the non-scalability of S.S. have become major challenges for nowadays CMOS technology. To deal with the above issues, in this thesis, we divide our study into two main parts, *i.e.*, the investigation of the suspended-NW-channel thin film transistors (TFTs) and the development of a novel SG-type device.

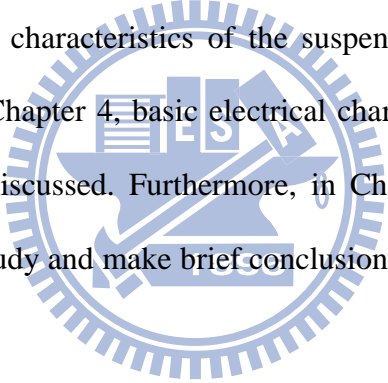
First, we focus on examining and clarifying the unique electrical characteristics of the suspended-NW-channel TFTs. In our previous works, devices with ultra-low S.S. were fabricated successfully [20-22]. However, many interesting characteristics the devices exhibit, such as the gradual turn-on behavior, oscillation of S.S., effects of NW channel dimensions, the asymmetric S.S. in hysteresis measurements and so on, are not clear and worth exploring [20-22]. Hence, in this thesis, we try to make some inductive inference from our data. In addition, the air gap thickness effect and some other interesting characteristics which are similar to the behaviors displayed by the SG-MOSFETs are also investigated.

Second, we also take advantage of the ultra-low S.S. in SG-MOSFETs and the exemption from advance lithography systems in VMOS to develop a new device structure. Here, we call it suspended-gate vertical channel MOSFET (SG-VMOS), a device structure combining the features of VMOS and SG-MOSFET. In addition to the intrinsic advantage of SG-VMOS, in our work, further cost down could be achieved thanks to the proper design of process flow which uses only two main

photolithographic reticles. Note that, compared with the suspended NW channel devices, we have changed the suspending material from undoped poly-Si to the conductive heavily doped one in the SG-VMOS. In this thesis, we will examine the basic electrical characteristics of VMOS and propose process adjustment suggestions to improving the basic characteristics of VMOS and SG-VMOS.

## **1-4 Organization of This Thesis**

In this thesis, a general background of VMOS and low S.S. devices are introduced in Chapter 1. In Chapter 2, complete device fabrication process flows of suspended NW channel TFTs and SG-VMOS, and relevant measurement setup are described. In Chapter 3, some interesting characteristics of the suspended NW channel TFTs are examined and clarified. In Chapter 4, basic electrical characteristics of the fabricated VMOS are presented and discussed. Furthermore, in Chapter 5, we summarize the major observations in this study and make brief conclusions. Finally, some suggestions are given for future work.



## ***Chapter 2***

---

# ***Device Fabrication***

### **2-1 Device Structure and Process Flow of Suspended-NW-channel TFTs**

Figure 2.1 (a) shows the top view of the device. The cross-sectional views of the device along the cutline  $\overline{AB}$  indicated in Fig. 2.1(a) in key fabrication steps of the fabrication are shown in Figs. 2.1 (b) to (f). All the devices in this section are fabricated on 6-inch bare silicon substrates capped with a 250 nm wet oxide.

First, a 150 nm *in-situ*  $n^+$  doped polycrystalline silicon layer was deposited by low pressure chemical vapor deposition (LPCVD) at 550 °C and defined as the gate electrode [Fig. 2.1 (b)]. After a standard clean process, a 20 nm silicon nitride layer and a 10 nm, 30 nm, 80 nm or 100 nm sacrificial TEOS oxide layer were deposited at 780 °C and 700 °C, respectively. Next, a 100 nm amorphous silicon layer ( $\alpha$ -Si) was deposited at 550 °C successively. All these films were deposited with LPCVD. Afterwards, a solid phase crystallization (SPC) treatment was performed at 600 °C in  $N_2$  ambient for 24 hours to transform the silicon film from amorphous phase into polycrystalline phase [Fig. 2.1 (c)]. With a photolithography step and the over-etching-time-controlled reactive ion etching (RIE) technique, the source/drain (S/D) regions and sidewall NWs were defined simultaneously [Fig. 2.1 (d)]. Here, the

over etching time is the major parameter for determining the dimensions of NW channels. Figures 2.2 (a) and (b) show the cross-sectional transmission electron microscopy (TEM) images of suspended NW channel from the cutline  $\overline{AB}$  indicated in Fig. 2.1 (a) with over-etch time of 28 sec (thin NW) and 22 sec (thick NW), respectively. Thereafter, an additional photoresist (PR) layer was covered on the suspended-channel region followed by the phosphorous S/D ion implantation at 15 keV with a dose of  $5 \times 10^{15} \text{ cm}^{-2}$  [Fig. 2.1 (e)]. Note that, the PR-covered channel region became the effective NW channels in our devices. For the dopant activation and the device passivation, a 400 nm TEOS layer was deposited on the entire wafer by LPCVD at  $700 \text{ }^\circ\text{C}$ . After a contact hole opening step with the aid of  $160 \text{ }^\circ\text{C}$  hot  $\text{H}_3\text{PO}_4$  and BOE wet etching processes to remove the surface capping nitride and oxide, respectively, typical device fabrication was accomplished.

To further suspend the NW channels, a BOE wet etching process was performed to remove the sacrificial TEOS layer between the NW channels and the silicon nitride gate dielectric layer. Here, the high BOE etching selectivity between LPCVD TEOS and LPCVD silicon nitride could avoid the direct contact of NW channels and the gate electrode after the wet etching step. As a result, an air gap was formed and the suspended-NW-channel TFTs were accomplished [Fig. 2.1 (f)]. Table 2.1 summarizes the split conditions of our suspended-NW-channel TFTs. Figure 2.3 shows the top view of suspended-NW-channel TFT taken by scanning electron microscope (SEM).

## **2-2 Device Structure and Process Flow of Vertical MOSFETs**

As a quick start, Fig. 2.4 (a) shows the top view of VMOS layout and the remaining figures shown in Fig. 2.4 are the cross-sectional views along the cutline

$\overline{AB}$  indicated in Fig. 2.4(a).

First, we used 6-inch n-type (100) bare silicon as starting wafers. The resistivity of substrates was in the range of 2 to 7  $\Omega \cdot \text{cm}$ . After a conventional photolithography process, we applied a  $\text{Cl}_2/\text{HBr}/\text{O}_2$ -based anisotropic plasma etching step [35-38] to define the vertical channel [Fig. 2.4 (b)]. The etched depth would roughly determine the dimension of the channel length. But the real electrical channel length would depend on the S/D junction depth and sidewall spacer gate width, as we would mention later. Certain amount of polymer would be formed on the sidewalls of patterns during the dry etching process, so a post-SC-1 clean was used to clean the sidewalls. Figure 2.5 shows the in-line SEM images of our patterns in the SEM bar region and device region just after the vertical channel definition. Because any surface roughness and etch-induced damage left on the sidewalls may cause severe mobility degradation and lead to a reduction in on-current, a 30 nm sacrificial thermal oxide was grown on the surface to smooth the channel surface and remove the damage sites.

Before removing the sacrificial oxide layer, we performed a phosphorous ion implantation at 170 keV with a dose of  $4 \times 10^{12} \text{ cm}^{-2}$  to dope the channel [Fig. 2.4 (c)]. In this step, the sacrificial oxide layer mentioned above served as a screen oxide to prevent channeling effect in single-crystalline substrates. Note that, the above ion implantation step was carried out at a tilt angle of  $45^\circ$ , a twist angle of  $72^\circ$ , and the wafer was rotated 4 times to realize sidewall implantation. Afterwards, the sacrificial (screen) oxide was removed.

Thereafter, we performed the RCA clean and formed the gate stack on the surface. First, a 4 nm dry oxide was grown at  $800^\circ \text{C}$  on the channel surface as a buffer layer. Next, a 9 nm silicon nitride layer was deposited by LPCVD at  $780^\circ \text{C}$ . And then a sacrificial TEOS oxide layer with thickness of 50 nm or 80 nm was deposited at  $700^\circ \text{C}$

by LPCVD successively. Finally, a 150 nm *in-situ* n<sup>+</sup> doped polycrystalline silicon layer was deposited at 550 °C as the gate material [Fig. 2.4 (d)]. Note that, all the high temperature and long thermal processes above may enhance the diffusion of channel dopants. Figure 2.6 shows the simulation results of total doping concentration profile in our devices with 50 nm TEOS sacrificial layer. In this simulation, we took into account all thermal budgets including subsequent S/D annealing.

Afterwards, the second mask of our process was applied to define gate electrode [Fig. 2.4 (e)]. By using the Cl<sub>2</sub>/HBr-based RIE technique combined with an etching endpoint detector, we could form the sidewall spacer gate electrode which would serve as the suspended gate later in our SG-VMOS. Before S/D ion implantation, a diluted hydrofluoric acid (DHF) wet etching was performed to etch the exposed TEOS oxide layer. Note that it was a delicate step for lowering the S/D implantation energy and acquiring much abrupt S/D junctions. As shown in Fig. 2.7, too high an implantation energy would result in a broader doping profile and deeper S/D junction depth [39]. Figures 2.8 and 2.9 show the in-line SEM images of our patterns in the device region after sidewall spacer gate definition and DHF wet etching. Subsequently, a self-aligned S/D ion implantation was carried out by implanting BF<sub>2</sub><sup>49+</sup> ions vertically with energy of 25 keV and dose of 5×10<sup>15</sup> cm<sup>-2</sup>, and activated by a spike rapid thermal annealing (RTA) at 1000 °C [Fig. 2.4 (f)]. Next, for device passivation, a 400 nm TEOS layer was covered on the entire wafer by plasma enhanced chemical vapor deposition (PECVD). Finally, contact hole opening was accomplished by a series of wet etching steps. The top passivation layer, silicon nitride gate dielectric and thermal oxide buffer layer were removed by immersing wafers in BOE, 160 °C hot H<sub>3</sub>PO<sub>4</sub> and BOE solutions in sequence, and a typical VMOS was thus accomplished. Table 2.2 summarizes the split conditions of our VMOS devices.

Note that to form our SG devices, an additional step was necessary. Specifically, a BOE wet etching process was performed to remove the TEOS layer between the sidewall spacer gate and gate dielectric layer. As mentioned previously in Section 2-1, the silicon nitride layer between the thermal buffer oxide and the TEOS oxide layer served as an etching stop layer by taking advantage of the high BOE etching selectivity between LPCVD TEOS and LPCVD silicon nitride. After that, an air gap was formed and the gate was suspended over the vertical channel [Fig. 2.4 (g)]. Note, in this step, the TEOS overlapped by the gate pad region was also etched simultaneously. However, the area overlapped by the gate pad was much larger than that covered by the sidewall spacer gate, so that a well-controlled etching time would remove the TEOS area covered by the sidewall gate completely, while leaving most of the TEOS under the gate pad region untouched. Thus a SG-VMOS was finally realized.

### **2-3 Measurement Setup and Electrical Characterization**

The current-voltage (I-V) characteristics were evaluated by an automated measurement setup constructed by an HP 4156A precision semiconductor parameter analyzer, an Agilent TM 5250A switch, and the Interactive Characterization Software (ICS). During all measurements, the temperature was controlled at a stable value by temperature-regulated chuck.

For the electrical characterization, some important electrical parameters could be extracted from the  $I_D$ - $V_G$  curves according to their definitions [15]. Here, we will illustrate the definitions of the subthreshold slope (S.S.), transconductance ( $g_m$ ) and threshold voltage ( $V_{th}$ ).

First, the S.S. can be calculated from the subthreshold currents in the weak inversion region by



$$S.S. \equiv \frac{\partial V_G}{\partial \log I_D}. \quad (\text{Eq. 2-1})$$

Second, the  $g_m$  is extracted by the differentiation of drain currents over gate voltages, *i.e.*,

$$g_m \equiv \left. \frac{\partial I_D}{\partial V_G} \right|_{V_D = \text{const}}. \quad (\text{Eq. 2-2})$$

Third, the  $V_{th}$  is calculated by the  $g_m$  maximum method with drain bias of -50 mV to ensure device operating in the linear region. As we know, the  $I_D$ - $V_G$  curves deviate from a straight line at gate voltages below  $V_{th}$  due to subthreshold currents and above  $V_{th}$  due to series resistance and mobility degradation effects. So, it is common practice to find the point of maximum slope on the  $I_D$ - $V_G$  curves by the maximum in the transconductance. In practice, we fit a straight line to the  $I_D$ - $V_G$  curve at that point and extrapolate to  $I_D = 0$ . The intersect point is defined as  $V_{Gi}$ . Next we apply the following equation to calculate  $V_{th}$  [40].

$$V_{th} \equiv V_{Gi} - V_D / 2. \quad (\text{Eq. 2-3})$$

# *Table Captions*

Table 2.1. Split table for suspended-NW-channel TFTs.

Wafer Number		01	02	03	04	05	06	07	08
Over Etching Time (sec)	22	☆	☆	☆	☆	☆			
	28						☆	☆	☆
Air Gap (TEOS) Thickness (nm)	N/A	☆					☆		
	10		☆						
	30			☆				☆	
	80				☆				
	100					☆			☆

Table 2.2. Split table for SG-VMOS.

Wafer Number		01	02	03	04	05	06
Nominal Channel Length ( $\mu\text{m}$ )	0.5	☆	☆	☆			
	1				☆	☆	☆
Air Gap (TEOS) Thickness (nm)	N/A	☆			☆		
	50		☆			☆	
	80			☆			☆

## ***Chapter 3***

---

# ***Electrical Characteristics of Suspended-NW-channel TFTs***

### **3-1 Basic Electrical Characteristics**

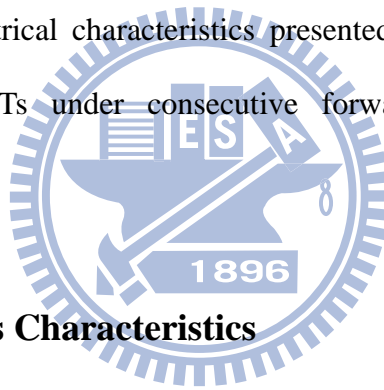
Figures 3.1 (a) and (b) show the  $I_D$ - $V_G$  curves of a conventional NW TFT and suspended-NW-channel TFT. As indicated in Figs. 3.1 (a) and (b), the conventional TFT and the suspended-NW-channel TFT refer to the one without and with the air gap structures, respectively. It can be seen that the suspended-NW-channel TFT depict a surprisingly low minimum S.S. of 35 mV/dec. compared with a mediocre 928 mV/dec. for the conventional counterpart. Apparently, the minimum S.S. is significantly improved for devices with suspended structure, despite their larger nominal EOT due to the lower dielectric constant of air over the TEOS oxide. Specifically, the suspended-NW-channel TFTs are having a gate dielectric stack of 30 nm air/ 20 nm silicon nitride and the nominal EOT of 128.14 nm. In contrast, for the conventional TFTs, the gate dielectric stack consists of 30 nm TEOS/ 20 nm silicon nitride with a nominal EOT of 41.14 nm. Figure 3.2 shows the plot of S.S. versus subthreshold  $I_D$  for a device without sacrificial TEOS layer (i.e., with 20 nm silicon nitride only), and devices before and after stripping the TEOS layer (i.e., the conventional TFT and

suspended-NW-channel TFT, respectively). Among these three device structures, the suspended-type one shows the best minimum S.S. throughout the subthreshold regime which further implies that the operation mechanism is not that straightforward. According to our previous results [20-22], such unusually small S.S. is referred to the electro-mechanical action of the suspended NW channels. The operation principle of NW channels in the suspended-NW-channel TFTs are mentioned in Subsection 1-2-4 and our previous work [20-22]. A detailed discussion will be presented later in Sections 3-2 and 3-3. In addition, such an unusually small S.S. also results in the lowering of  $V_{th}$ , extracted by the constant current method [40], between the conventional devices and the suspended-NW-channel ones shown in Figs. 3.1 (a) and (b). Furthermore, the suspended-type devices exhibit a lower OFF state current, defined as the corresponding  $I_D$  at  $V_G = 0$  V, which is advantageous in terms of reliability and power consumptions. Table 3-1 shows the comparisons of electrical parameters between the conventional TFTs and suspended-NW-channel TFTs including nominal EOT,  $V_{th}$  and minimum S.S.

## 3-2 Hysteresis Phenomenon

In order to investigate the operation principle of the devices, in this section, detailed discussion on the hysteresis phenomenon in the suspended-NW-channel TFTs under consecutive forward and reverse sweeping measurements is presented including the examination of the effects of the structure dimensions, gate voltage sweeping rate, and other factors that may affect the hysteresis characteristics. Before starting our discussions, some electrical and structural parameters are defined in Fig. 3.3 in which typical hysteresis curves of the suspended-NW-channel TFTs are shown. These electrical parameters include the pull-in voltage ( $V_{pi}$ ), pull-out voltage ( $V_{po}$ ), forward

sweep S.S. (S.S.<sub>F</sub>), reverse sweep S.S. (S.S.<sub>R</sub>) and the hysteresis window. Among them, the hysteresis window is defined as the  $V_{th}$  difference between the forward and reverse sweeping measurements extracted by constant current method [40] at a constant drain current of  $5 \times 10^{-10}$  A, and  $V_{pi}$  and  $V_{po}$  are defined as the  $V_G$  corresponding to the occurrence of pull-in and pull-out, respectively, of the suspended NW channels. Finally, S.S.<sub>F</sub> and S.S.<sub>R</sub> are extracted from the forward and reverse subthreshold regions, respectively, with a roughly stable value, different from the minimum S.S. mentioned previously. For the structural parameters, the definitions of the S/D extension length and channel length are shown in Fig. 3.4. With the aids of the following observations, the operation mechanism of the suspended-NW-channel TFTs is illustrated in Section 3-3. Note that, all the electrical characteristics presented in this section are for the suspended-NW-channel TFTs under consecutive forward and reverse sweeping measurements.



### 3-2-1 Basic Hysteresis Characteristics

Figure 3.5 shows typical hysteresis curves for the suspended-NW-channel TFT with channel length of 0.4  $\mu\text{m}$  and air gap thickness of 80 nm under specified operation conditions. An ultra-low minimum S.S. of 58 mV/dec. and a hysteresis window of 3.7 V are recorded. In the forward sweeping measurement, as  $V_G$  increases and reaches  $V_{pi}$ , a jump in  $I_D$  is observed. This is an indication of pull-in action that the suspended NW channels begin to contact the gate nitride due to the attractive electrical force exerted by the gate voltage. This leads to a dramatic decrease in EOT and thus a large increase in  $I_D$ . However, dissimilar to most previous works in the SG-MOSFETs [19] that the S.S. can be smaller than 10 mV/dec., in the present case, the S.S. is only slightly smaller than the ideal 60 mV/dec. due to the fact that the increase in  $I_D$  is limited, so

the transition between the ON state and the OFF state is not abrupt. In other words, the turn-on behavior in our devices is gradual, in contrast to the sudden switching phenomenon presented in previous studies [19]. Based on such observation, it is postulated that, in the beginning of the contacting action, only the central region of the NW channels are in contacted with the gate stack, so the potential barrier away from the central region of the NW channels are still high resulting in a limited  $I_D$  and a non-abrupt transition behavior.

When  $I_D$  reaches a level between  $1 \times 10^{-7}$  A and  $1 \times 10^{-9}$  A, the variances of  $I_D$  with the  $V_G$  modulation become non-smooth in both the forward and reverse sweeping directions, as shown in Fig. 3.5. This feature is in strong contrast to the characteristics of the conventional device shown in Fig. 3.1(a). As we will illustrate and explain later, in the suspended-NW-channel TFTs, the variances of  $I_D$  with the  $V_G$  modulation are dependent on two completing mechanisms, i.e., the mechanical action of the suspended NW channels and the field-effect action of the conventional TFTs. In this case, for the devices operated at the current level below  $1 \times 10^{-9}$  A, the former one is dominating. For the devices operated at the current level higher than  $1 \times 10^{-7}$  A, the later one becomes the dominant mechanism. However, in the inter-level, both mechanisms are comparable in strength leading to a transient-like behavior in  $I_D$ - $V_G$  curves. This phenomenon was also referred to as the S.S. oscillation phenomenon in our previous work [22]. An example is given in Fig. 3.6 which shows the plot of S.S. versus  $I_D$  for devices under the forward and reverse sweeping measurements, respectively.

Another interesting phenomenon in the suspended-NW-channel TFTs is the asymmetric S.S. between the forward and the reverse sweeping measurements. As we can see from Fig. 3.6, the  $S.S._F$  ( $\sim 230$  mV/dec.) extracted in the  $I_D$  range from  $10^{-11}$  A to  $10^{-10}$  A is much steeper than the reverse one ( $\sim 330$  mV/dec.). From the point of view

of the static force balance, for the pull-in action of the suspended NW channels, only the elastic recovery force and the electrostatic force are involved. However, as we sweep the  $V_G$  in reverse, the pull-out action of the NW channels is impeded further by the additional adhesion forces [29, 41], resulting in the worse S.S. in the reverse sweeping measurement.

Figure 3.7 shows the endurance characteristics for the suspended-NW-channel TFTs under cycling measurements. Apparently, after 120 times of operation cycles, the hysteresis window is enlarged. Besides, the hysteresis window opening is observed in our measurements from 1.82 V to 2.7 V. Figure 3.8 shows the  $I_D$ - $V_G$  curves of the fresh device and the device after 120 times of operation cycles. There is no obvious S.S. degradation in both forward and reverse sweep measurements, so the  $V_{th}$  shift is not originating from the variances of the S.S. As reported by various groups [42-44], the shift of  $V_{th}$  is a signature of the charge trapping in the dielectric layer. As  $V_G$  reaches  $V_{pi}$ , the suspended NW channels are pulled in and make contact with the gate stack, a sudden increase in  $I_D$  occurs. After cycles of operation electrons are trapped in the nitride layer. This would result in an increase in  $V_{pi}$ . This means it needs a larger gate voltage to induce electrons in the channel for pull-in action. Such a result is reasonable since the nitride is a well-known electron trapping layer for SONOS flash devices. However, the above inference seems not reasonable in explaining the decreasing  $V_{po}$  after cycles of operation. That is, the electrically attractive force between the channel and the gate is weakened with the aforementioned electron trapping phenomenon and thus  $V_{po}$  should increase as  $V_{pi}$  does, rather than decrease. The exact reason for the  $V_{po}$  is still under investigation. One possible explanation is the decline in force constant of the suspended channel with increasing operation cycles. Fatigue of the movable object's elasticity will reduce the restore force and therefore, a delay in pull-out action

is resulted.

### 3-2-2 Effects of Structure Dimensions

In this subsection, we will present a detailed discussion about the influences of device dimensions on the hysteresis characteristics in the suspended-NW-channel TFTs. The device dimensions with which we are dealing include the channel length, the S/D extension length, the NW thickness and the air gap thickness.

Figures 3.9 and 3.10 show the hysteresis curves of the suspended-NW-channel TFTs with different channel length and S/D extension length, respectively. For the devices with a given 0.5  $\mu\text{m}$  S/D extension length and 100 nm air gap, as the channel length increases from 0.4  $\mu\text{m}$  to 5  $\mu\text{m}$ , the  $V_{\text{pi}}$ , hysteresis window and the ON current decrease accordingly, as shown in Fig. 3.9. The elastic constant of the NW channels in the devices with shorter channel length is larger, leading to a larger  $V_{\text{pi}}$  and the earlier detachment of the NW channels from the gate stack. However, it is difficult to find out the specific  $V_{\text{G}}$  corresponding to the starting moment of the NW channel's pull-out action, i.e., the pull-out point, simply from the electrical characteristics. Note that, the  $V_{\text{po}}$  is treated as the corresponding  $V_{\text{G}}$  at the moment of fully detachment of NW channels from the gate stack. In Fig. 3.9,  $V_{\text{po}}$  is defined as the  $V_{\text{G}}$  when the  $I_{\text{D}}$  drops to the level dominated by the off-state leakage. It is found that the  $V_{\text{po}}$  is smaller as the channel becomes shorter. In addition, the smaller contact area between the NW channels and the gate stack during operation in the devices with shorter channel length also results in the worse S.S.<sub>F</sub> and S.S.<sub>R</sub>. Figures 3.11, 3.12 and 3.13 show the plots of hysteresis window,  $V_{\text{pi}}$ ,  $V_{\text{po}}$ , S.S.<sub>F</sub> and S.S.<sub>R</sub>, respectively, versus channel length for devices with two different S/D extension lengths (see Fig. 3.4). Apparently, as the S/D extension length shrinks to 0.25  $\mu\text{m}$ , the variance in the hysteresis window,  $V_{\text{pi}}$ ,  $V_{\text{po}}$ ,



S.S.<sub>F</sub> and S.S.<sub>R</sub> with channel length become unobvious. Despite these facts, there are significant differences in various electrical parameters between devices with the S/D extension length of 0.5 μm and 0.25 μm, as shown in Fig. 3.10. The device with S/D extension length of 0.25 μm is with a higher  $V_{pi}$  and worse S.S. in both sweep directions than its counterpart with 0.5 μm S/D extension length. Note that the total length of the suspended object is roughly the sum of the length of the suspended channel and the S/D extension. The difference between the two devices shown in Fig. 3.10 is postulated to be originated from the larger elastic constant and the smaller contact area in the device with shorter (0.25 μm) S/D extension, therefore it needs a larger electrically attractive force to overcome the elastic force. Furthermore, the 0.25 μm one is also with a lower ON current. This implies that the portion of the 2-μm-long undoped suspended channels in contact with the gate nitride in the ON state is smaller for the device with shorter (0.25 μm) S/D extension.

Figure 3.14 shows the hysteresis curves of devices with different NW dimensions which are controlled by the over-etching time. The longer over-etching time will form NWs with smaller dimension (denoted as “thin” in the figure). Figures 3.15, 3.16 and 3.17 show the plots of hysteresis window,  $V_{pi}$ ,  $V_{po}$ , S.S.<sub>F</sub> and S.S.<sub>R</sub>, respectively, versus channel length for devices with two different NW dimensions. Apparently, the devices with thinner NW channels are with better S.S. in both the forward and reverse sweeping measurements due to the larger contacted area compared with the ones with thicker NW channels, as shown in Fig. 3.17. In addition,  $V_{pi}$  in the devices with thinner NW channels is also slightly lower, as shown in Fig. 3.16. These two observations imply that the thinner NW channels are with smaller elastic constant and thus smaller elastic forces as compared with the thicker counterparts. The higher flexibility of the thinner NW channels also result in a slightly higher ON current despite the larger

channel width of the thicker one. It implies that the effective EOT, which is determined by the contact area of channel and gate nitride in ON-state, becomes the dominating factor in the magnitude of ON current instead of the channel width when the devices are operated at the ON state. However, there is no apparent difference in the hysteresis window and the  $V_{po}$  between the devices of two different NW dimensions, as shown in Figs. 3.15 and 3.16. Owing to the larger elastic constant in the thicker NW channels, the pull-out action may occur slightly earlier than the ones with thinner NW channels. In these comparisons, the most obvious difference occurs in the S.S.<sub>R</sub>. The reason is not clear, but is presumably related to the smaller channel/gate contact area during the ON-state mentioned above.

Figure 3.18 shows the hysteresis curves of devices with different air gap thickness. Clearly, the air gap thickness indeed affects the electrical characteristics of the suspended-type devices including the suspended-NW-channel TFTs and the SG-MOSFETs [29]. The corresponding plots of hysteresis window,  $V_{pi}$ ,  $V_{po}$ , S.S.<sub>F</sub> and S.S.<sub>R</sub> versus air gap thickness are shown in Figs. 3.19, 3.20 and 3.21, respectively. As we could see from Fig. 3.19, the devices with a thicker air gap show a larger hysteresis window which is similar to and confirmed with the simulation results of the SG-MOSFETs [29]. A thicker air gap corresponds to a larger displacement when the NW channels contact with the gate stack, and leads to a larger elastic recovery force and  $V_{pi}$ , as shown in Figs. 3.18 and 3.20. Furthermore, as the air gap thickness increases, the contacted area is limited due to the larger elastic recovery force, so both the S.S.<sub>F</sub> and S.S.<sub>R</sub> are worse than those with a thinner air gap, as shown in Fig. 3.21. As explained in pervious section that, in the beginning of the channel-gate nitride contacting process, the region contacted with the gate stack is limited to the central region of the NW channels only. Hence, we could postulate that the two ends of the

NW channels are not contacted with the gate stack and the area of the non-contacted region increases with the air gap thickness. Furthermore, the potential barrier at the two ends of the NW channels also limits the flowing out of inversion carriers. Such a phenomenon reflects on the worse S.S.<sub>R</sub> and larger  $V_{po}$ .

### 3-2-3 Effects of $V_G$ Sweeping Rate

The results shown above were obtained through measurements performed with a fixed  $V_G$  sweeping rate with increment of 50 mV per step. In order to investigate the dependence of the  $V_G$  sweeping rate on the hysteresis characteristics of the suspended-NW-channel TFTs, we change the increment of  $V_G$  per step ( $\Delta V_G$ ) in a sequence of 100 mV, 50 mV, 25 mV, 20 mV and 10 mV, and the results are shown in Fig. 3.22. Figures 3.23, 3.24 and 3.25 show the plot of hysteresis window,  $V_{pi}$ ,  $V_{po}$ , S.S.<sub>F</sub> and S.S.<sub>R</sub> versus  $\Delta V_G$ , respectively. Apparently, as  $\Delta V_G$  decreases, the hysteresis window is narrowed while the S.S.<sub>F</sub> and S.S.<sub>R</sub> are improved, as shown in Figs. 3.23 and 3.25, respectively. The lowering in both  $V_{pi}$  and  $V_{po}$  further evidences such dependence, as shown in Fig. 3.24. In addition, as shown in Fig. 3.22, the anomalous variances of  $I_D$  with the  $V_G$  modulation or the subthreshold oscillation phenomenon mentioned in Subsection 3-2-1, becomes less significant as  $\Delta V_G$  decreases. Note that the change of electric force during the measurement is slowed down with a smaller  $\Delta V_G$ , the mechanically restoring force which corresponds to the amount of channel deformation or the size of the channel-gate nitride contact area can respond accordingly, thus the above anomalous I-V characteristics can be suppressed. Such trend convinces our previous postulation that the oscillation phenomenon is a transient-like behavior originated from the unbalance of the competition between the mechanical action of the suspended NW channels and the electrical behavior of the

conventional TFTs.

### 3-2-4 Summary

Based on previous observations, we make an inductive inference in this subsection. Briefly speaking, the structure dimensions and sweeping rate indeed influence device characteristics of the suspended-NW-channel TFTs through the modulation of the contact area of NW channels and the gate stack as well as the competition between the electrostatic force and the restoring force. Table 3.2 summarizes the variance trend of various electrical parameters with an increase in structural parameters and  $V_G$  sweeping rate.

### 3-3 Operation Mechanism

According to the observations shown above and in our previous published papers [20-22], a conceptual model is proposed to explain the operation mechanism and the hysteresis phenomenon exhibited by the suspended-NW-channel TFTs. Figures 3.26 (a), (b) and (c) show the states of the suspended NW channels corresponding to specific bias conditions.

At first, the devices are operated in the OFF state with a low  $I_D$  under a low  $V_G$ , as indicated by point A in Fig. 3.27. In this state, the NW channels are suspended and separated from the stack of silicon nitride gate dielectric and polycrystalline silicon gate electrode by the air gap, as shown in Fig. 3.26 (a). When the  $V_G$  is swept forward, for charge neutrality, the positive  $V_G$  tends to induce a certain amount of negative charged electrons in the NW channels which results in an attractive electrostatic force between the NW channels and the gate stack. In the beginning, such electrostatic force may be balanced by the elastic recovery force arising from the bending of NW

channels and the NW channels remain suspended. When the attractive force becomes sufficiently large with increasing  $V_G$ , the electrostatic force may surpass the elastic recovery force and pull the NW channels toward the silicon nitride layer. Eventually, the NW channels contact with the silicon nitride layer, resulting in a sudden increase in  $I_D$ . This occurs when  $V_G = V_{pi}$ , as indicated by point B in Fig. 3.27. Such a dramatic change in  $I_D$  is originated from the significant reduction in effective dielectric layer thickness. However, at this moment, in our devices, only the central region of NW channels is in contact with the gate dielectric layer, as shown in Fig. 3.26 (b), which explains why the increase in  $I_D$  is limited. As the  $V_G$  increases further, the portion of NW channels connecting to the gate dielectric layer widens gradually and the  $I_D$  increases further, as shown in Fig. 3.26 (c) and indicated by point C in Fig. 3.7. Finally, the devices are operated in the ON state, as indicated by point D in Fig. 3.27. Note that, when the devices transfer the operation states from C to D, the dominating operation mechanism changes accordingly from the mechanical one to the electrical one. Between state C and D, an oscillation phenomenon in S.S. noted in Section 3-1 occurs because the two competing mechanisms are of approximately equal strength.

For the reverse sweep, in the beginning, the electrostatic force with the aid of surface adhesion forces such as van der Waals force and capillary force [45] will hold most of the NW channels in contact with the gate dielectric layer for a while. Hence, in this state, a relatively high  $I_D$  is sustained, as indicated by point E in Fig. 3.27. However, the attractive electrostatic force still decreases with decreasing  $V_G$  due to the repelling of the electrons stored in the NW channels and leading to a decrease in effective attractive force between the NW channels and the gate stack. As the elastic recovery force becomes larger than the weakened effective attractive force, the NW channels may gradually depart from the gate stack and the  $I_D$  decreases with decreasing

$V_G$  in this state, as shown in Fig. 3.26 (b) and indicated by point F in Fig. 3.27. Finally, the NW channels are back into the suspended state, the electrons residing in the NW channels are released and the devices are turned off, as shown in Fig. 3.26 (a) and indicated by point A in Fig. 3.27.

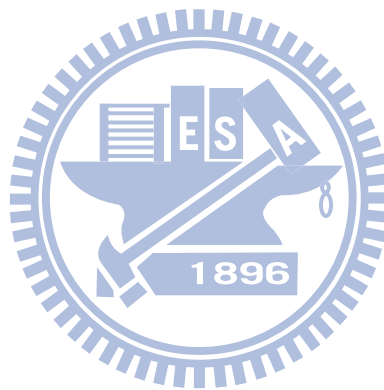


## *Table Captions*

Table 3.1. Comparisons of electrical parameters between the conventional NW TFTs and suspended-NW-channel TFTs.

	EOT (nm)	Minimum S.S. (mV/dec)	V <sub>th</sub> (V)
<b>Conventional NW TFTs</b>	41.14	928	4.83
<b>Suspended-NW-Channel TFTs</b>	128.14	35	1.67

Table 3.2. Variance trend of electrical parameters with an change in structural parameters and V<sub>G</sub> sweeping rate. (Symbols: ↑: increasing, ↓: decreasing, –: no obvious variance)

	Channel Length	S/D Extension Length	NW Thickness	Air Gap Thickness	V <sub>G</sub> Sweeping Step Size
	↑	↑	↑	↑	↑
<b>Hysteresis Window</b>	↓	↓	–	↑	↑
V <sub>pi</sub>	↓	↓	↑	↑	↑
V <sub>po</sub>	↓	↓	–	↑	↑
<b>S.S.F</b>	↓	↓	↑	↑	↑
<b>S.S.R</b>	↓	↓	↑	↑	↑

## ***Chapter 4***

---

# ***Electrical Characteristics of***

# ***Vertical MOSFETs***

### **4-1 Background**

In Chapter 3, we have investigated the dependences of several structural and operational parameters on the electrical characteristics of the suspended-NW-channel TFTs. Based on these observations and analysis, it is shown that the electrical hysteresis characteristics are strongly related to applied  $V_G$  sweep rate. The results indicate that the switching speed is not fast, anyway. One of the possible reasons for this outcome is related to the tiny undoped suspended-NW channels. Because of its undoped nature, during operation the induced carriers require certain time to diffuse into the channel region. To clarify this argument, we propose an alternative device structure in Chapter 2 (Fig. 2.2), called SG-VMOS, which changes the suspending material from undoped poly-Si to heavily-doped conductive one. In this structure, the induced charges in the bulk channel should have much faster response time. We intend to investigate such new device, unfortunately the present mask set designed for fabricating suspended-NW-channel TFTs is not suitable for the new device. Hence, in this study, we just fabricate and characterize VMOS and examine the process



conditions which form the basis for future SG-VMOS construction.

## 4-2 Basic Electrical Characteristics

In order to streamline our discussion on the electrical characteristics of the fabricated asymmetric VMOS devices, we define the operation modes first. Figure 4.1 shows the bias configurations of the VMOS devices under the forward and reverse operation modes. For the forward mode, the drain bias is applied to the top terminal while the bottom terminal (source) is grounded. For the reverse mode, the drain and source biases are interchanged.

Figures 4.2 (a) and (b) show the  $I_D$ - $V_G$  curves of VMOS devices operated under the forward mode with nominal channel length of 0.5  $\mu\text{m}$  and 1  $\mu\text{m}$ , respectively. It is obvious that both devices exhibit robust anti-punch-through ability. As the drain bias increases from -50 mV to -1.5 V, there is no significant degradation in S.S. Such good characteristics are attributed to the tilted channel implantation step shown in Fig. 2.2 (c). In this step, we rotate the ion beam direction 4 times and make the resultant doping concentration in the channel near the top surface region about 4 times higher than the remaining portion of the sidewall channel region, as shown in Figs. 2.4 (a) and (b). Hence, there is a halo-like heavily doped region near the top terminal which can reduce the off-state leakage current including the surface and bulk punch-through current apparently [46].

In the subthreshold region, all of the fabricated VMOS devices exhibit a unique two-step turn-on phenomenon, i.e., two subthreshold regions with distinctly different S.S., as shown in Figs. 4.2 (a) and (b). According to a previous work [47], this phenomenon may originate from the convex corner effect. Figure 4.3 shows the convex corners in the VMOS. Note that, the effective channel width of the convex

corner region is much narrower than the width sum of the normal transistor component with the four flat drain edges seen from the top view (Fig. 4.3). It has been shown that [48], at the convex corner region, the oxidation rate is non-uniform and dependent on the stress-dependent surface reaction and the stress-dependent viscosity. As a result, the local oxide thinning and the sharpening of the silicon/oxide interface occur [48]. The thinner oxide at the corner regions results in a much higher electrical field strength at the channel/oxide interface, lower  $V_{th}$ , and steeper S.S. Especially, the curvature of the corners also plays an important role in this phenomenon. At the convex corner, the oxide electric field at the neighborhood of the silicon surface is much higher as compared with that inside the oxide, and decreases in a rate of  $1/r$  [47]. Based on these facts, we propose a conceptual model to explain this phenomenon. First, we divide the VMOS into two different shunted MOSFETs, as shown in Fig. 4.4 (a). The device 1 represents the one built in the convex corner region with lower  $V_{th}$  and steeper S.S. (S1). The device 2 represents the normal one with higher  $V_{th}$  and worse S.S. (S2), which is located at the flat channel regions. Second, we take Fig. 4.4 (b) to illustrate the origin of two-S.S. phenomenon in the VMOS. In region A, both MOSFETs are operated in the subthreshold regime. In principle, owing to the better S.S. and the lower  $V_{th}$  in device 1, it dominates the output characteristics in this region. Note that, in the shunted circuit, the output current is the summation of currents in each branch. In region B, the device 1 has been turned on, but the device 2 is still operated at the subthreshold regime. As aforementioned, owing to the much larger channel width in device 2, the  $I_{D2}$  surpasses the  $I_{D1}$  in this region. In other words, the  $I_D$  is dominated by  $I_{D2}$  in region B. Similarly, in region C, the  $I_D$  is also dominated by  $I_{D2}$  while both devices are turned on. In short, the measured  $I_D$ - $V_G$  curve is a summation of respective  $I_D$ - $V_G$  curves in these two shunted devices throughout the operation, as shown in Fig.

4.4 (c).

For the on-state characteristics of the VMOS under drain bias of -50 mV, the  $I_D$  are slightly pinned to a specific level regardless of the channel length, as shown in Figs. 4.2 (a) and (b). It is a direct evidence of series resistance effect. For the devices with shorter channel length, it becomes much more obvious. This phenomenon can be further examined by the output characteristics, shown in Figs. 4.5 (a) and (b).

Table 4.1 summarizes the average electrical characteristics of the VMOS measured from 32 nominally identical devices. In general, our devices exhibit a good on-off ratio of  $10^6$  and acceptable anti-punch through ability.

Next, we examine the electrical characteristics of devices operated under reverse mode to investigate the influences of doping concentration profile and geometric structure differences on electrical characteristics further, as mentioned in Chap. 2 and illustrated in Fig. 2.4 (a). As shown in Figs. 4.6 (a) and (b), the off-state leakage currents increase dramatically accompanied by severe S.S. degradation for the devices operated under reverse operation mode and a drain bias of -1.5 V, in strong contrast to the characteristics illustrated by the forward mode. The non-saturated  $I_D$  characteristics verify its poor anti-punch-through ability further which is in agreement with previous results, as shown in Figs. 4.7 (a) and (b). As we have mentioned previously, due to the much heavier doping concentration near the top terminal (drain side) which can more effectively suppress the penetration of electric field under forward operation mode, thus a better anti-punch-through ability is resulted.

### **4-3 Discussion**

So far, we have successfully fabricated VMOS featuring implanted S/D with acceptable device characteristics. These process conditions can be further applied for

realization of SG-VMOS once the appropriate mask design is made. However, the minimum channel length we made in this work is 0.5  $\mu\text{m}$ . For devices with shorter channel length, such as 0.3 $\mu\text{m}$  or shorter, process window for the implantation conditions and subsequent annealing treatments becomes smaller and hard to control. Such concern can be lifted as epitaxial process is employed for forming the source, drain and channel regions.



# Table Captions

Table 4.1. The average value of various electrical parameters extracted from 32 nominally identical VMOS devices.

$L_{\text{nominal}}$ ( $\mu\text{m}$ )	$V_{\text{th}}$ (V)	S1 (mV/dec.)	S2 (mV/dec.)	DIBL (mV/V)
0.5	-2.37	199.32	501.62	72.72
1	-2.67	222.99	570.04	75.68
$L_{\text{nominal}}$ ( $\mu\text{m}$ )	$I_{\text{on, lin}}$ (A)	$I_{\text{on, sat}}$ (A)	$I_{\text{off, lin}}$ (A)	$I_{\text{off, sat}}$ (A)
0.5	$1.15 \times 10^{-4}$	$3.14 \times 10^{-3}$	$4.94 \times 10^{-11}$	$1.49 \times 10^{-9}$
1	$7.96 \times 10^{-5}$	$2.29 \times 10^{-3}$	$3.40 \times 10^{-11}$	$5.19 \times 10^{-10}$



## ***Chapter 5***

---

# ***Conclusion and Future Work***

### **5-1 Conclusion**

In this thesis, we have successfully developed and fabricated two kinds of novel devices, including the suspended-NW-channel TFTs and the VMOS. The suspended NW channels in the suspended-NW-channel TFTs and the sidewall spacer gate electrode in the VMOS are formed by the simple over-etching-time-controlled RIE technique. The major advantage of this work lies in its ingenious process flow design. There is no advanced lithography tool or process involved and the devices are accomplished simply by low cost fabrication processes. Especially, in the VMOS, further cost down could be achieved as only two main photolithographic reticles are needed through the process.

For the suspended-NW-channel TFTs, after forming the air gap, an ultra-low minimum S.S. of 35 mV/dec. is achieved successfully, which is much better than 928 mV/dec. exhibited by the device before the sacrificial oxide was stripped off to form the air gap. The suspended-channel device is also accompanied with a lowering in  $V_{th}$  and a reduction in  $I_{OFF}$ . For the hysteresis characteristics of the devices under consecutive forward and reverse sweeping measurements, a hysteresis window of 3.7 V is recorded. The limited pull-in  $I_D$ , the transient-like behavior in  $I_D$ , the asymmetric S.S., and the hysteresis window opening characteristics are also observed and analyzed.

The first characteristic is related to the limited contact area of the suspended NW channel and the gate stack. The transient-like behavior in  $I_D$  is due to the competition in strength of two operation mechanisms, i.e., the field-effect action for conventional TFTs and the mechanical action for suspended NW channels. The asymmetric S.S. characteristic is attributed to the presence of additional adhesion forces impeding the detachment of channels further in reverse sweepings. And the hysteresis window opening characteristic in the endurance experiment is explained by the electron trapping in forward sweepings and the elastic fatigue in reverse sweepings. Besides, the specific trends in hysteresis window,  $V_{pi}$ ,  $V_{po}$ , S.S.<sub>F</sub> and S.S.<sub>R</sub> with the variances of geometric structure dimensions and  $V_G$  sweeping rate are studied. Our results show that the longer channel length and the S/D extension length is beneficial for scaling down the  $V_{pi}$ ,  $V_{po}$  and getting steeper S.S.<sub>F</sub>, S.S.<sub>R</sub>. Similarly, the scaling down of air gap thickness is also conducive to lowering  $V_{pi}$ ,  $V_{po}$  and improving S.S.<sub>F</sub>, S.S.<sub>R</sub>. Besides, the S.S.<sub>F</sub> and S.S.<sub>R</sub> can be optimized further by implementing thinner NW channels. In the  $V_G$  sweeping rate experiments, a decrease in  $V_G$  step size leads to a lower  $V_{pi}$ ,  $V_{po}$  and better S.S.<sub>F</sub>, S.S.<sub>R</sub>. In addition, the transient-like behavior in  $I_D$  also reduces as the  $V_G$  sweeping rate is reduced. Nevertheless, the scaling down of  $V_{pi}$ ,  $V_{po}$  and improving of S.S.<sub>F</sub>, S.S.<sub>R</sub> are always accompanied with the shrinking in hysteresis window. Finally, based on all of above observations, a conceptual model illustrating the interaction between the electrostatic force, elastic recovery force and surface adhesion forces during device operation is proposed.

Second, the VMOS, operated under forward mode bias configuration, shows reduced off-state leakage current as compared with the one operated under reverse mode. At high drain bias, the punch-through currents are effectively restrained by the halo-like region. Generally, the fabricated VMOS exhibits a good on-off ratio of  $10^6$

and acceptable anti-punch through ability when devices are operated under forward operation mode. In addition, an interesting two-step turn-on characteristic is also observed and explained by our conceptual model, which is related to the convex corner effect and the difference of effective channel width between the convex corner region and the rest parts of the channel.

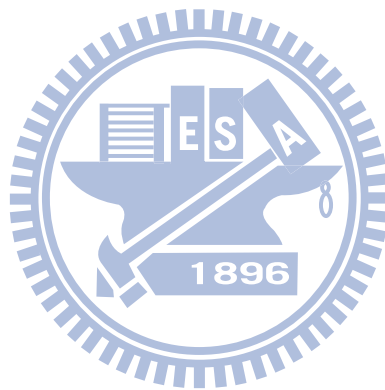
In conclusion, the fabrication and characterization of suspended-NW-channel TFTs with ultra-low S.S. and considerable hysteresis window are demonstrated. Our results show that the device characteristics of the suspended-NW-channel TFTs are indeed affected by structure dimensions and  $V_G$  sweeping rate through the modulation of the contact area of NW channels and the gate stack as well as the competition between the electrostatic force and the restoring force. Furthermore, the operation mechanism of them is clearly illustrated. With the aids of these observations, we can fabricate an optimized ultra-low S.S. suspended-type device depending on its applications. In addition, with proper process adjustments and the experiences from the suspended-NW-channel TFTs, the SG-VMOS with ultra-low S.S. can be fabricated successfully and achieve the goals of area saving further to fulfill the demands in the future.

## **5-2 Future Work**

The development and characterization of VMOS have been carried out in this work. To further fabricate the SG-VMOS with ultra-low S.S., a new device layout is required, as described previously in Section 4-1. Figure 5.1 shows the top view of modified SG-VMOS device layout. Clearly, the gate patterns and drain patterns are not fully overlapping each other. In this way, the influence of limited S/D ion implanted area and high-resistance region under the gate electrode patterns will be minimized.



Besides, to scale down the channel length in VMOS, we suggest the implementation of other techniques, such as epitaxial growth technique, to avoid the issues encountered in implantation method, as shown in Fig. 5.2.



# References

- [1] G. Moore, "Cramming more components onto integrated circuits," *Electronics*, vol. 38, pp. 114-117, 1965.
- [2] R. H. Dennard, F. H. Gaensslen, V. L. Rideout, E. Bassous, and A. R. LeBlanc, "Design of ion-implanted MOSFET's with very small physical dimensions," *IEEE Journal of Solid-State Circuits*, vol. 9, pp. 256-268, 1974.
- [3] S. Chou, "Integration and innovation in the nanoelectronics era," *ISSCC Tech Dig.*, vol. 1, pp. 36-41, 2005.
- [4] M. Bohr, "The new era of scaling in an SoC world," *ISSCC Tech Dig.*, pp. 23-28, 2009.
- [5] H. Xiao, *Introduction to semiconductor manufacturing technology*: Prentice Hall, 2001.
- [6] K. Ushida, "Future lithography challenges," presented at the International Symposium on Semiconductor Manufacturing, 2006.
- [7] C. Rittenhouse, W. Mansfield, A. Kornblit, R. Cirelli, D. Tomes, and G. Celler, "Sub-0.1  $\mu\text{m}$  NMOS transistors fabricated using laser-plasma point-source X-ray lithography," *IEEE Electron Device Letters*, vol. 16, pp. 322-324, 1995.
- [8] T. Rodgers and J. Meindl, "VMOS: high speed TTL compatible MOS logic," *IEEE Journal of Solid-State Circuits*, vol. 9, pp. 239-250, 1974.
- [9] L. Risch, W. H. Krautschneider, F. Hofmann, H. Schafer, T. Aeugle, and W. Rosner, "Vertical MOS transistors with 70 nm channel length," *IEEE Transactions on Electron Devices*, vol. 43, pp. 1495-1498, Sep 1996.
- [10] J. Hergenrother, D. Monroe, F. Klemens, A. Komblit, G. Weber, W. Mansfield, M. Baker, F. Baumann, K. Bolan, and J. Bower, "The vertical replacement-gate (VRG) MOSFET: a 50-nm vertical MOSFET with lithography-independent gate length," *IEDM Tech. Dig.*, pp. 75-78, 1999.
- [11] T. Schulz, W. Rosner, L. Risch, T. Aeugle, U. Langmann, and A. Korbel, "130nm vertical PMOS transistors with P<sup>+</sup> poly-gate," in *ESSDERC*, Bordeaux, France, 1998, pp. 168-171.
- [12] B. Roberds, E. Whang, A. Rudolph, and B. Doyle, "Investigation of a novel self-aligned dual gate MOSFET structure," in *IEEE International SOI Conference*, Stuart, FL, 1998, pp. 109-110.
- [13] D. A. Neamen, *Semiconductor physics and devices: basic principles, 3rd Edition*: McGraw-Hill Science Engineering, 2002.
- [14] Y. Taur and T. H. Ning, *Fundamental of modern VLSI devices*: Cambridge University Press, 1998.

- [15] S. M. Sze and K. K. Ng, *Physics of semiconductor devices, 3rd Edition*. Hoboken, New Jersey: John Wiley & Sons, Inc., 2007.
- [16] W. Y. Choi, J. Y. Song, J. D. Lee, Y. J. Park, and B. G. Park, "100-nm n-/p-channel I-MOS using a novel self-aligned structure," *IEEE Electron Device Letters*, vol. 26, pp. 261-263, Apr 2005.
- [17] K. Gopalakrishnan, P. Griffin, and J. Plummer, "I-MOS: a novel semiconductor device with a subthreshold slope lower than  $kT/q$ ," *IEDM Tech. Dig.*, pp. 289-292, 2002.
- [18] P. Wang, K. Hilsenbeck, T. Nirschl, M. Oswald, C. Stepper, M. Weis, D. Schmitt-Landsiedel, and W. Hansch, "Complementary tunneling transistor for low power application," *Solid State Electronics*, vol. 48, pp. 2281-2286, 2004.
- [19] N. Abele, R. Fritschi, K. Boucart, F. Casset, P. Ancey, and A. Ionescu, "Suspended-gate MOSFET: bringing new MEMS functionality into solid-state MOS transistor," *IEDM Tech. Dig.*, pp. 479-481, 2005.
- [20] H. C. Lin, C. H. Kuo, G. J. Li, C. J. Su, and T. Y. Huang, "Operation of a novel device with suspended nanowire channels," *IEEE Electron Device Letters*, vol. 31, pp. 384-386, May 2010.
- [21] C. H. Kuo, H. C. Lin, G. J. Li, H. H. Hsu, C. J. Su, and T. Y. Huang, "A novel thin-film transistor with suspended nanowire channels and side-gated configuration," presented at the International Conference on Solid-State Devices and Materials, 2009.
- [22] G. J. Li, "Fabrication and characterization of a novel device with suspended nanowire channels," Master Thesis, Department of Electronics Engineering and Institute of Electronics, College of Electrical and Computer Engineering, National Chiao-Tung University, Hsinchu, 2009.
- [23] C. Shen, J. Lin, E. Toh, K. Chang, P. Bai, C. Heng, G. Samudra, and Y. Yeo, "On the performance limit of impact-ionization transistors," *IEDM Tech. Dig.*, pp. 117-120, 2007.
- [24] A. Savio, S. Monfray, C. Charbuillet, and T. Skotnicki, "On the limitations of silicon for I-MOS integration," *IEEE Transactions on Electron Devices*, vol. 56, pp. 1110-1117, May 2009.
- [25] P. F. Wang, T. Nirschl, D. Schmitt-Landsiedel, and W. Hansch, "Simulation of the Esaki-tunneling FET," *Solid-State Electronics*, vol. 47, pp. 1187-1192, Jul 2003.
- [26] J. Knoch, "Optimizing tunnel FET performance - Impact of device structure, transistor dimensions and choice of material," presented at the VLSI TSA, Hsinchu, 2009.
- [27] K. K. Bhuvalka, J. Schulze, and I. Eisele, "Scaling the vertical tunnel FET with tunnel bandgap modulation and gate workfunction engineering," *IEEE*

- Transactions on Electron Devices*, vol. 52, pp. 909-917, May 2005.
- [28] Y. Khatami and K. Banerjee, "Steep subthreshold slope n- and p-type tunnel-FET devices for low-power and energy-efficient digital circuits," *IEEE Transactions on Electron Devices*, vol. 56, pp. 2752-2761, Nov 2009.
- [29] K. Akarvardar, C. Tsamados, D. Chauhan, Y. Wan, G. Ionescu, A. Howe, R. Wong, and H. SP, "Analytical modeling of the suspended-gate FET and design insights for low-power logic," *IEEE Transactions on Electron Devices*, vol. 55, pp. 48-59, 2008.
- [30] N. Abele, A. Villaret, A. Gangadharaiah, C. Gabioud, P. Ancey, and A. Ionescu, "1T MEMS memory based on suspended gate MOSFET," *IEDM Tech. Dig.*, pp. 1-4, 2006.
- [31] A. Ionescu, V. Pott, R. Fritschi, K. Banerjee, M. Declercq, P. Renaud, C. Hibert, P. Fluckiger, and G. Racine, "Modeling and design of a low-voltage SOI suspended-gate MOSFET (SG-MOSFET) with a metal-over-gate architecture," in *ISQED*, 2002, pp. 496-501.
- [32] F. Bendriaa, F. Le-Bihan, A. C. Salaun, T. Mohammed-Brahim, C. Tlili, N. Jaffrezic, and H. Korri-Youssoufi, "DNA detection by suspended gate polysilicon thin film transistor," in *IEEE Sensors Conference*, 2005, pp. 412-415.
- [33] I. Eisele and M. Zimmer, "Hybrid-gate suspended field-effect transistors for gas-sensing," in *Device Research Conference*, 2002, pp. 113-116.
- [34] H. Mahfoz-Kotb, A. Salaun, T. Mohammed-Brahim, and O. Bonnaud, "Air-gap polycrystalline silicon thin-film transistors for fully integrated sensors," *IEEE Electron Device Letters*, vol. 24, pp. 165-167, 2003.
- [35] D. K. Kim, Y. K. Kim, and H. Lee, "A study of the role of HBr and oxygen on the etch selectivity and the post-etch profile in a polysilicon/oxide etch using HBr/O<sub>2</sub> based high density plasma for advanced DRAMs," *Materials Science in Semiconductor Processing*, vol. 10, pp. 41-48, Feb 2007.
- [36] L. Vallier, J. Foucher, X. Detter, E. Pargon, O. Joubert, G. Cunge, and T. Lill, "Chemical topography analyses of silicon gates etched in HBr/Cl<sub>2</sub>/O<sub>2</sub> and HBr/Cl<sub>2</sub>/O<sub>2</sub>/CF<sub>4</sub> high density plasmas," *Journal of Vacuum Science & Technology B*, vol. 21, pp. 904-911, Mar-Apr 2003.
- [37] I. Tepermeister, N. Blayo, F. P. Klemens, D. E. Ibbotson, R. A. Gottscho, J. T. C. Lee, and H. H. Sawin, "Comparison of advanced plasma sources for etching applications. I. Etching rate, uniformity, and profile control in a helicon and a multiple electron-cyclotron-resonance source," *Journal of Vacuum Science & Technology B*, vol. 12, pp. 2310-2321, Jul-Aug 1994.
- [38] F. H. Bell and O. Joubert, "Polysilicon gate etching in high density plasmas. V. Comparison between quantitative chemical analysis of photoresist and oxide

- masked polysilicon gates etched in  $\text{HBr}/\text{Cl}_2/\text{O}_2$  plasmas," *Journal of Vacuum Science & Technology B*, vol. 15, pp. 88-97, Jan-Feb 1997.
- [39] J. Plummer, M. Deal, and P. Griffin, *Silicon VLSI technology - fundamentals, practice and modeling*: Prentice Hall, 2000.
- [40] D. Schroder, *Semiconductor material and device characterization*: Wiley-IEEE Press, 2006.
- [41] M. Collonge, M. Vinet, S. Deleonibus, and G. Ghibaudo, "Nano accumulation-mode suspended-gate MOSFET: Impact of adhesion forces on electro-mechanical characteristics," in *Ultimate Integration of Silicon*, Udine, 2008, pp. 53 - 56.
- [42] D. Molinero, N. Abele, L. Castaner, and A. Ionescu, "Oxide charging and memory effects in suspended-gate FET," in *Micro Electro Mechanical Systems*, Tucson, AZ, 2008, pp. 685-688.
- [43] W. M. van Spengen, R. Puers, R. Mertens, and I. De Wolf, "A comprehensive model to predict the charging and reliability of capacitive RF MEMS switches," *Journal of Micromechanics and Microengineering*, vol. 14, pp. 514-521, Apr 2004.
- [44] Z. Peng, X. B. Yuan, J. C. M. Hwang, D. I. Forehand, and C. L. Goldsmith, "Superposition model for dielectric charging of RF MEMS capacitive switches under bipolar control-voltage waveforms," *IEEE Transactions on Microwave Theory and Techniques*, vol. 55, pp. 2911-2918, Dec 2007.
- [45] W. A. de Groot, J. R. Webster, D. Felnhofer, and E. P. Gusev, "Review of device and reliability physics of dielectrics in electrostatically driven MEMS devices," *IEEE Transactions on Device and Materials Reliability*, vol. 9, pp. 190-202, Jun 2009.
- [46] A. Bansal and K. Roy, "Asymmetric halo CMOSFET to reduce static power dissipation with improved performance," *IEEE Transactions on Electron Devices*, vol. 52, pp. 397-405, Mar 2005.
- [47] K. Yamabe and K. Imai, "Nonplanar oxidation and reduction of oxide leakage currents at silicon corners by rounding-off oxidation," *IEEE Transactions on Electron Devices*, vol. 34, pp. 1681-1687, Aug 1987.
- [48] H. Umimoto, S. Odanaka, and I. Nakao, "Numerical simulation of stress-dependent oxide growth at convex and concave corners of trench structures," *IEEE Electron Device Letters*, vol. 10, pp. 330-332, Jul 1989.

## Figure Captions

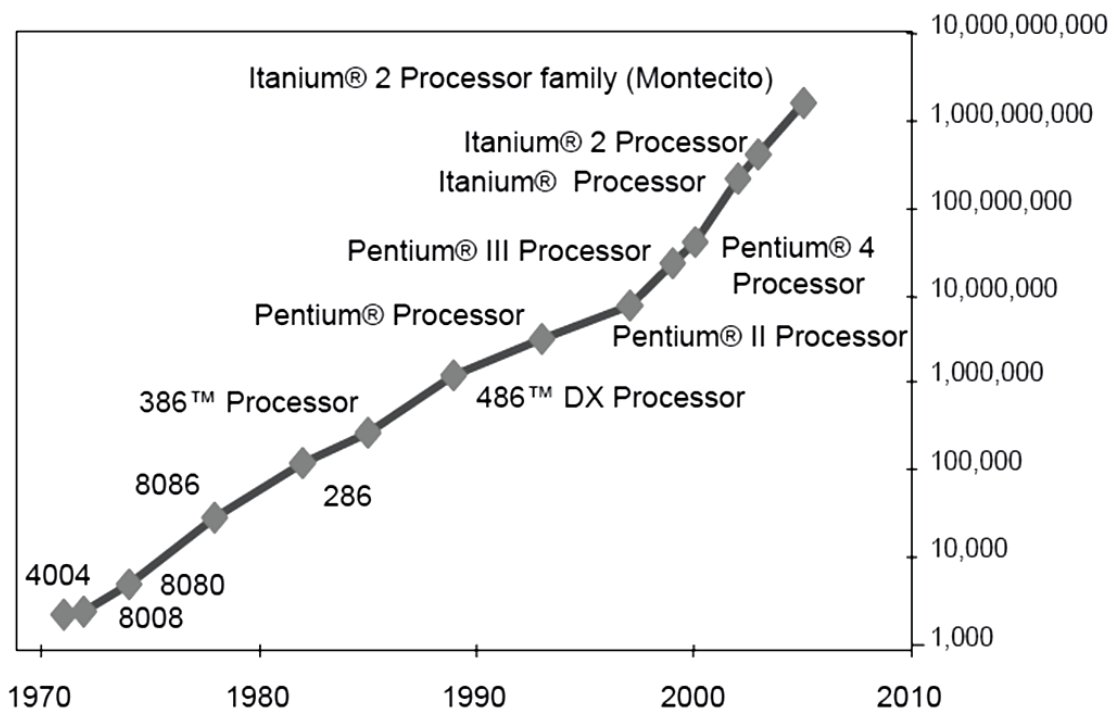


Figure 1.1. The progressive growth of Intel's CPU transistor counts per microprocessor [3].

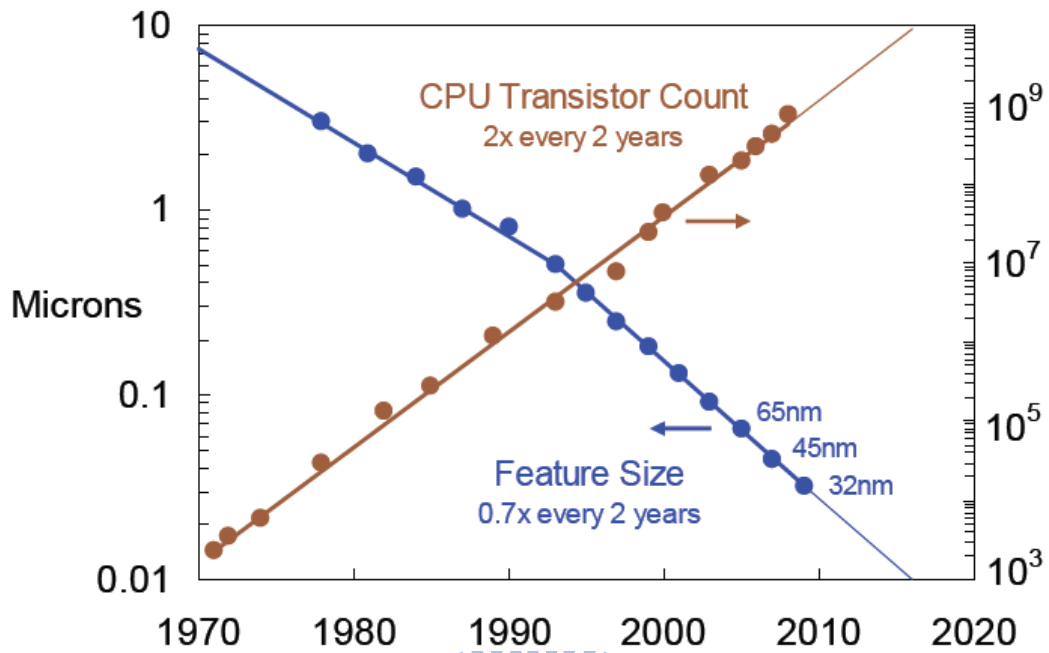


Figure 1.2. The CPU transistor count and feature size trends [4].

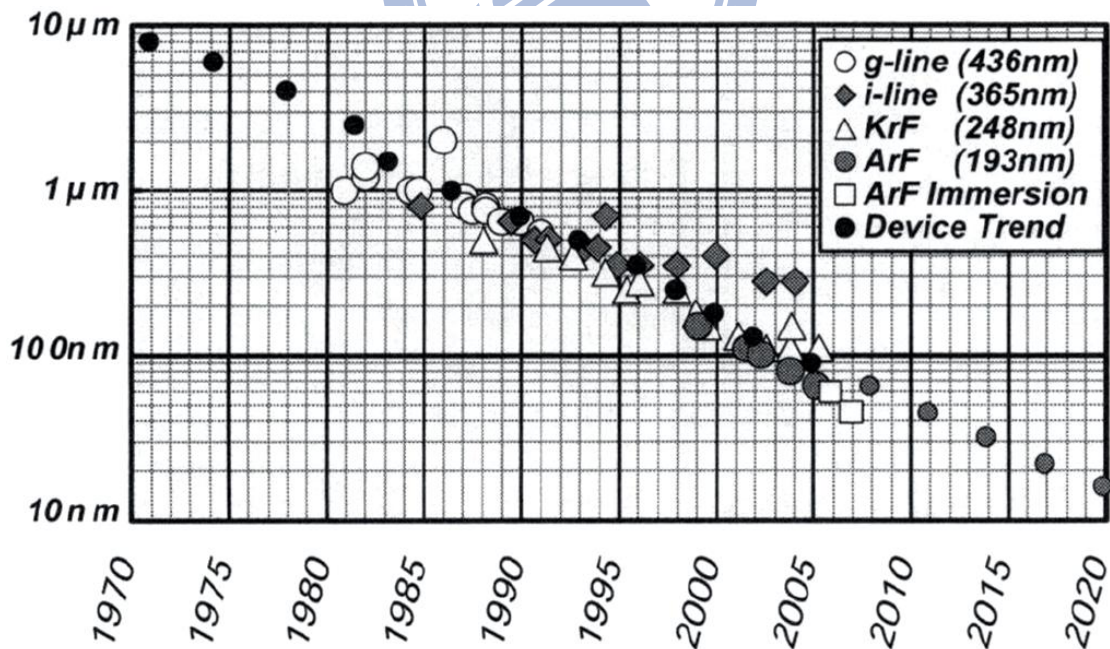
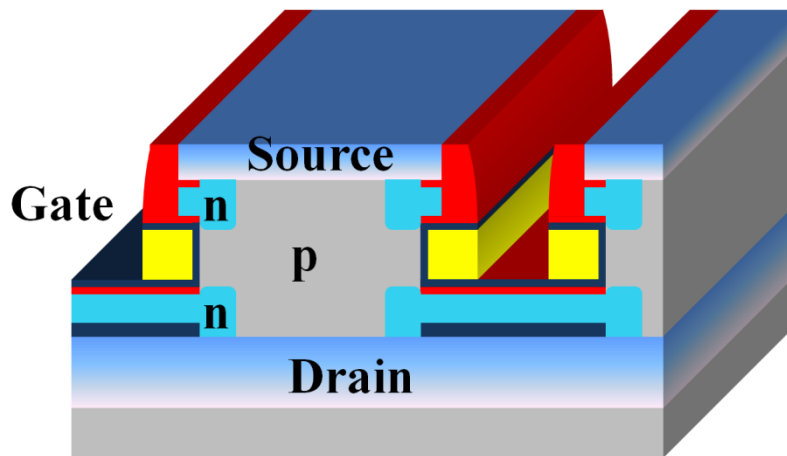
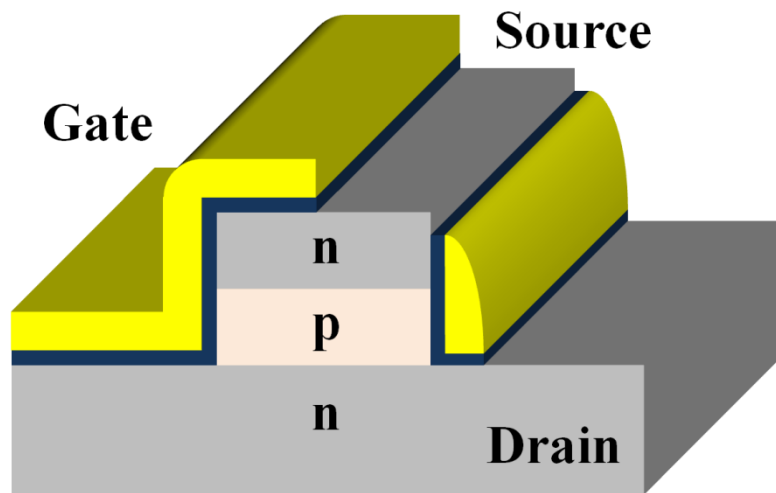


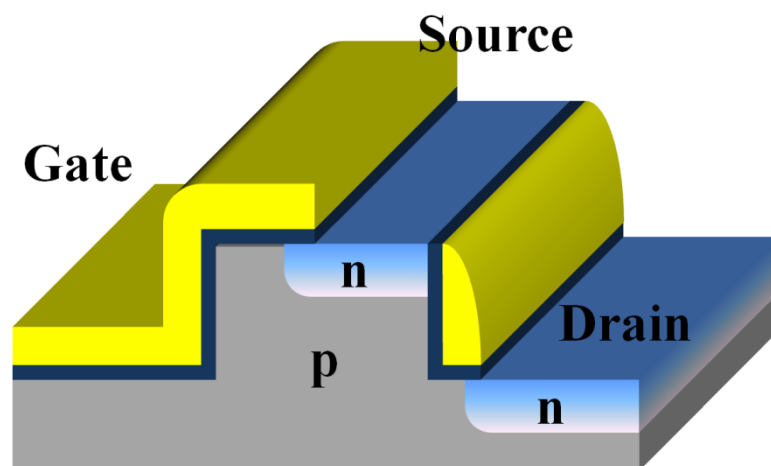
Figure 1.3. Evolution of device feature size and the resolution capability of exposure tools with various exposure wavelength [6].



(a)



(b)



(c)

Figure 1.4. Three major structures for the design of vertical MOSFETs, based on (a) solid source diffusion, (b) epitaxial and (c) implantation, respectively.



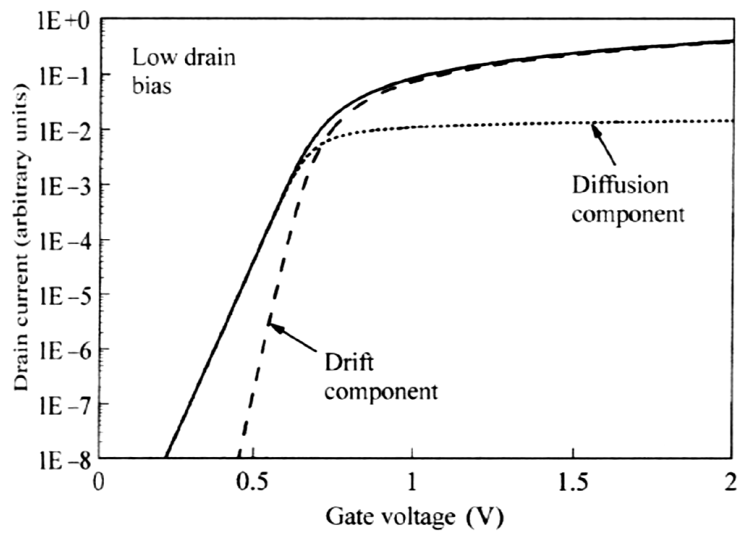


Figure 1.5. The conduction mechanism of drain current at low drain bias [14].

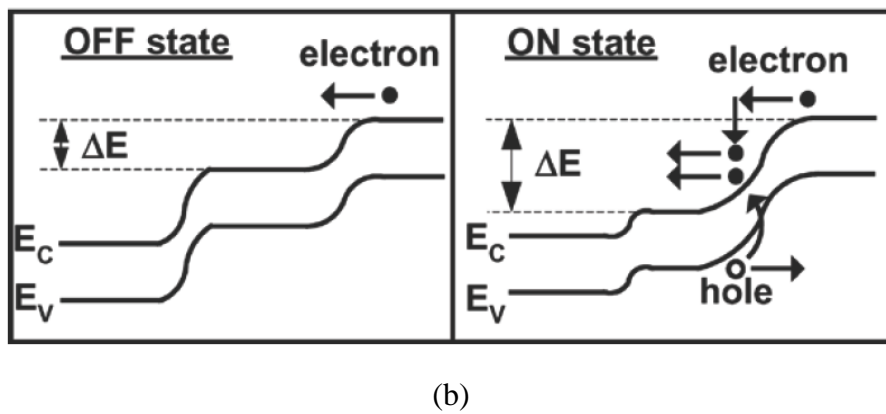
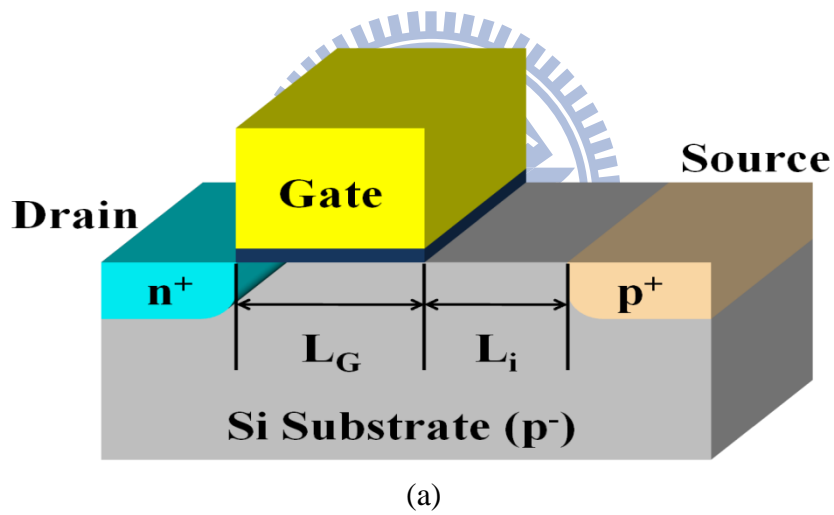


Figure 1.6. (a) Basic device structure and (b) band diagram in the ON/OFF state of the n-channel I-MOS [16].

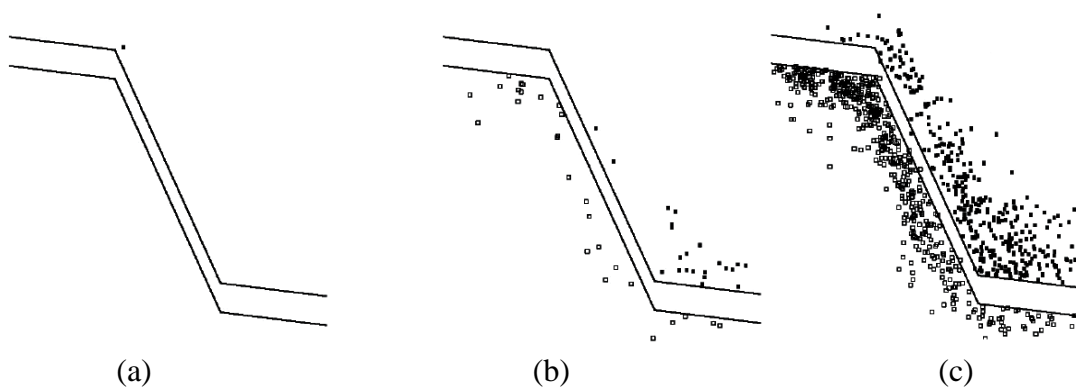


Figure 1.7. Carrier distribution in space- and energy-scale in a device with 50 nm-long high-field region obtained from 1D Monte-Carlo simulation, superimposed on the energy band diagram of the simulated structure. (a) One electron with low energy is injected from the left end of the high-field region at random time  $\tau_1$ . (b) The first carrier then initiates the impact ionization avalanche, and carrier number multiplies. However, with initially small number of carriers in the device, a strong random fluctuation is expected, until a reasonable number of carriers are present and overcome the randomness in carrier multiplication. (c) The carrier multiplication continues at an average rate [23].

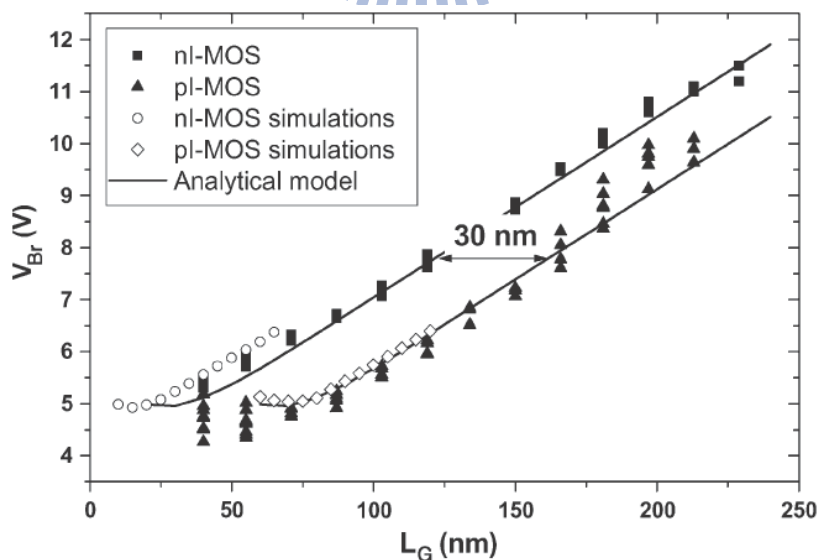


Figure 1.8. Simulated and experimental source-drain breakdown voltage,  $V_{Br}$ , versus gated channel length,  $L_G$ , curves for both n-type and p-type I-MOS [24]. The difference between n-type and p-type I-MOS is originated from dopant diffusion. The p-type dopant usually diffuses more extensively than the n-type one.

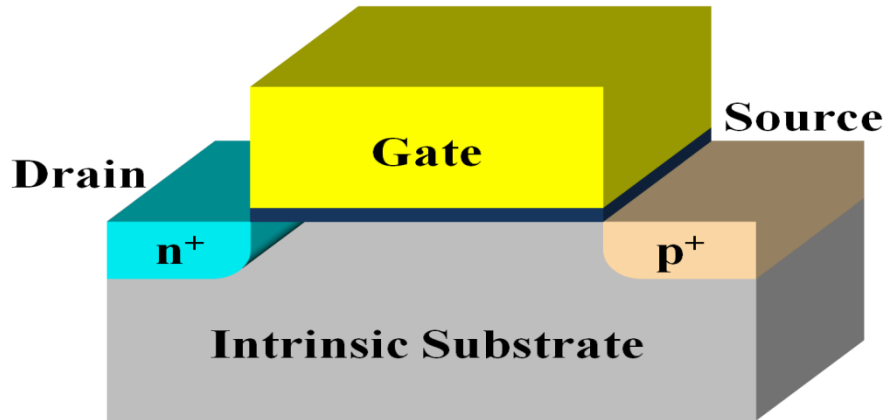


Figure 1.9. Schematic view of T-FET device structure.

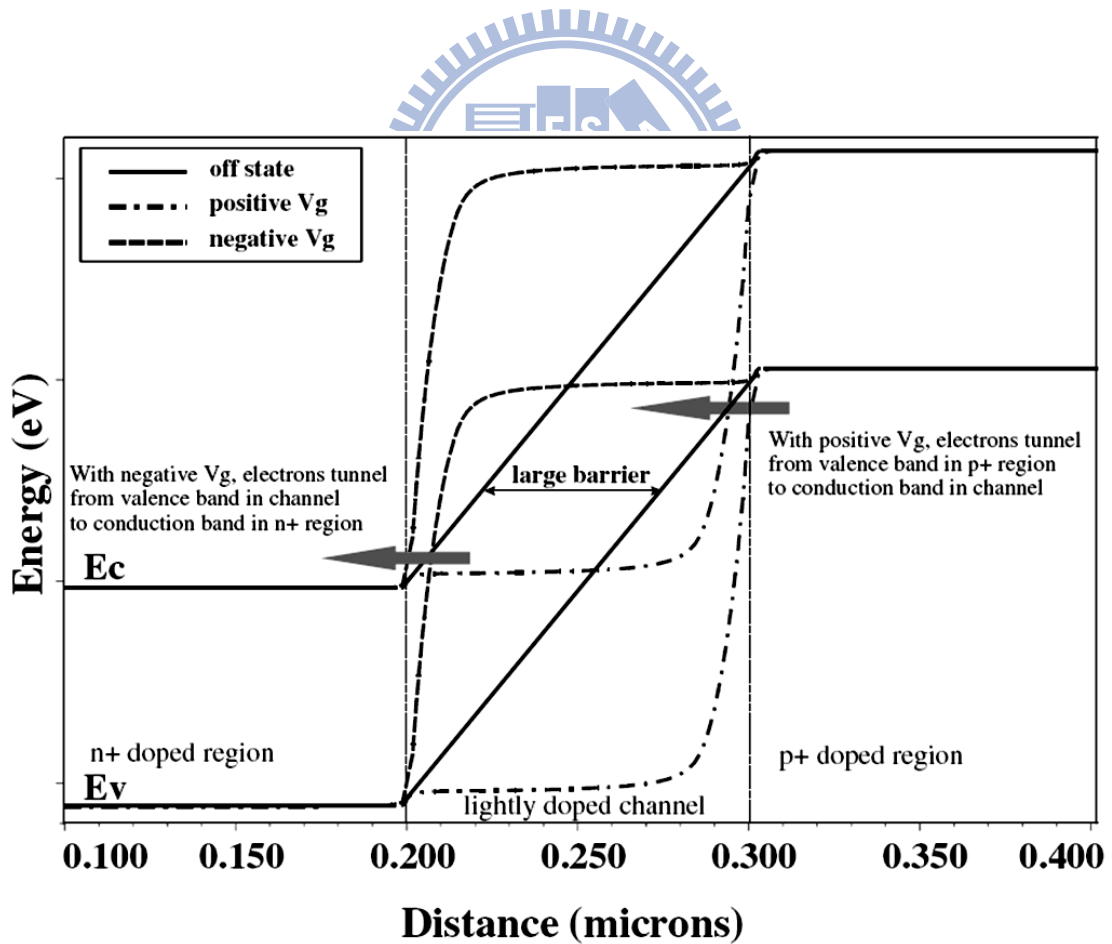
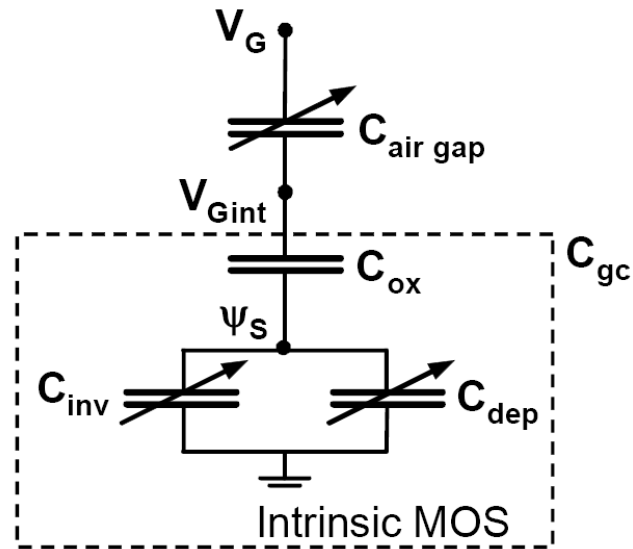
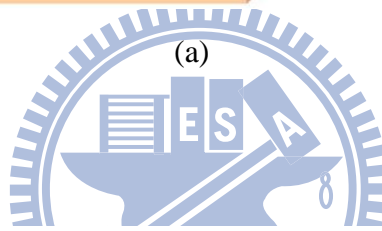
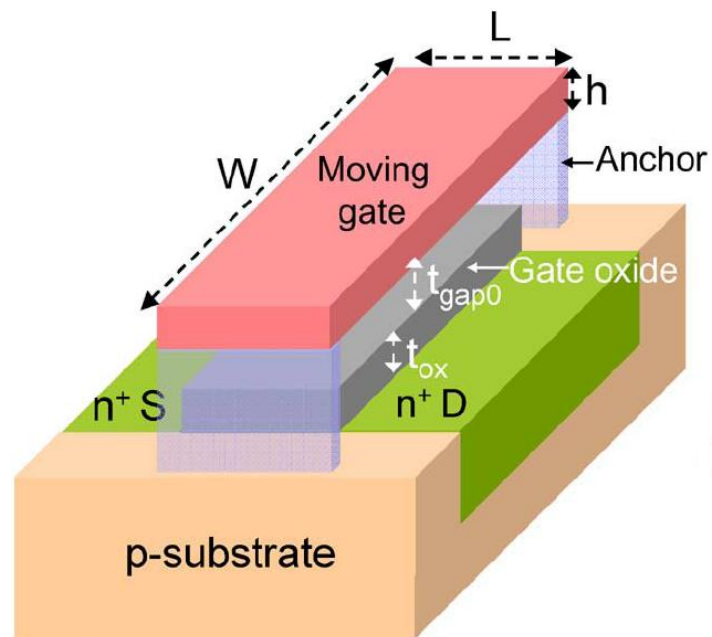


Figure 1.10. Energy band diagram for gate-controlled BTBT in T-FET with 100 nm channel length [18].



(b)

Figure 1.11. (a) Typical 3D structure of SG-MOSFET with anchors at both ends of SG suspended over the gate oxide layer [29]. (b) An equivalent electrical circuit of SG-MOSFET, *i.e.*, a combination of electrostatically actuated NEMS switch and inversion-mode MOSFET [30].

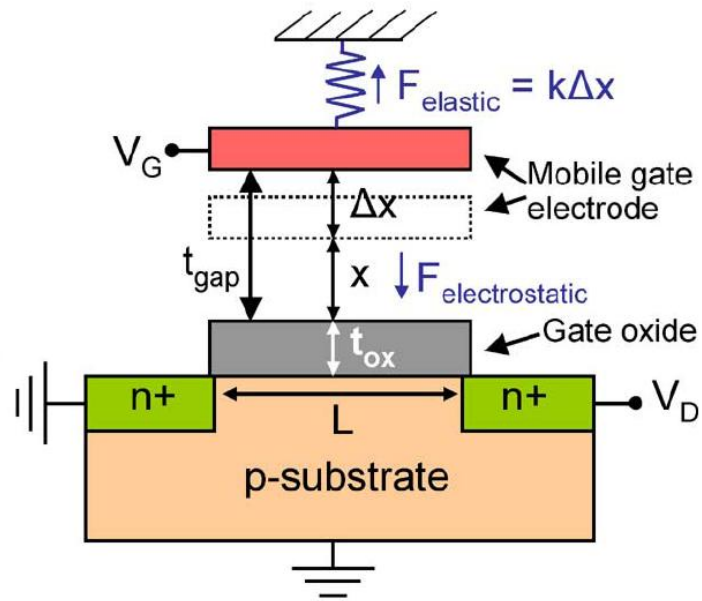


Figure 1.12. The 2D cross-section of SG-MOSFET. The SG-MOSFET is controlled by two competing forces, electrostatic force and elastic force [29].

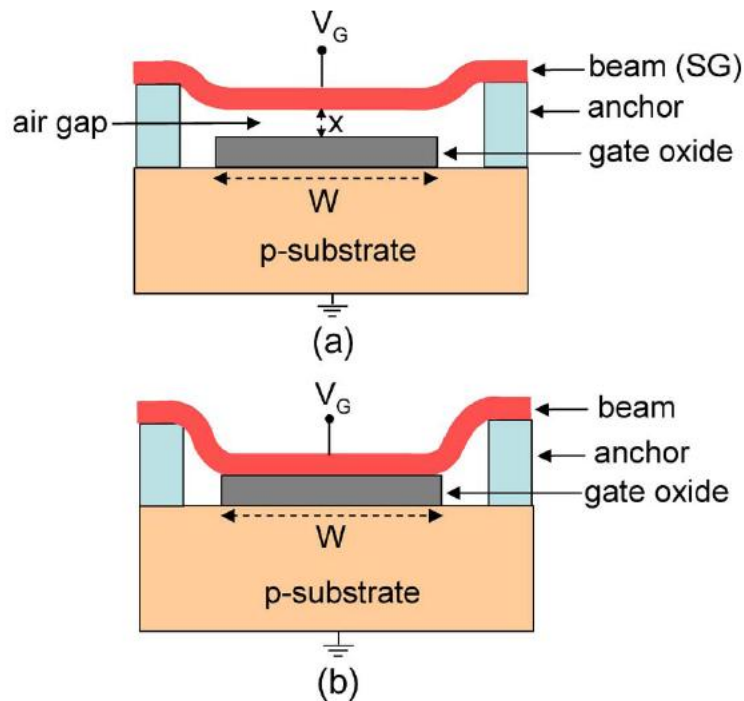


Figure 1.13. The operation principle of SG-MOSFET. (a) As  $V_G < V_{pi}$ , the electrostatic force is balanced by elastic force only. (b) As  $V_G > V_{pi}$ , the electrostatic force overcomes the elastic force and the SG will be connected with gate oxide layer. There is no air gap anymore. [29]

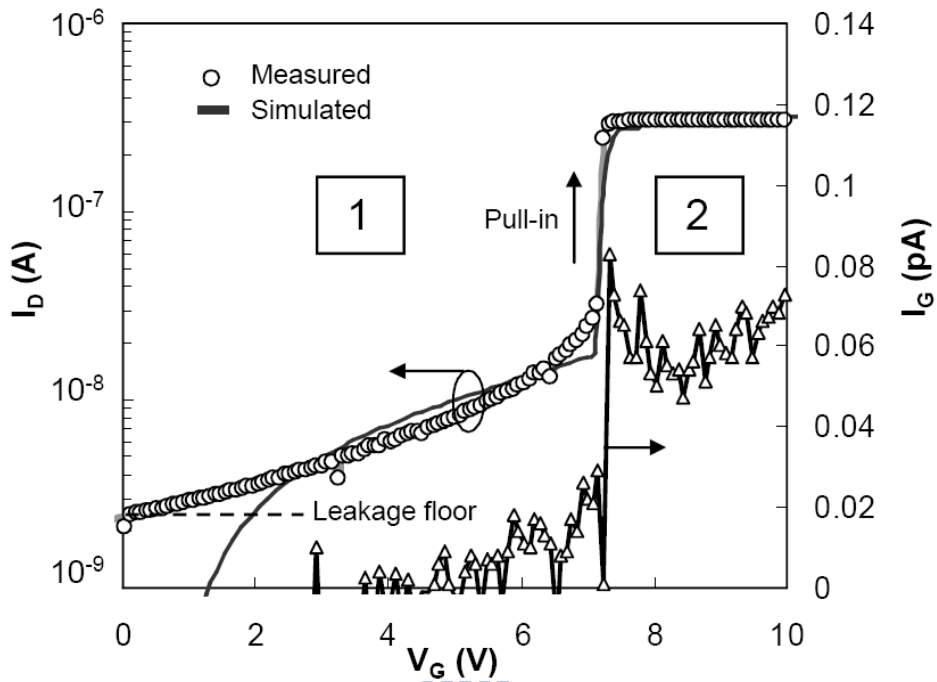


Figure 1.14. Typical  $I_D$ - $V_G$  characteristics of SG-MOSFET for  $V_D = 50$  mV. Region 1 represents the weak inversion regime and Region 2 represents the electromechanical pull-in of mobile gate after reaching the non-equilibrium point. (Symbols: measurement results; Solid Line: analytical simulation). [30]

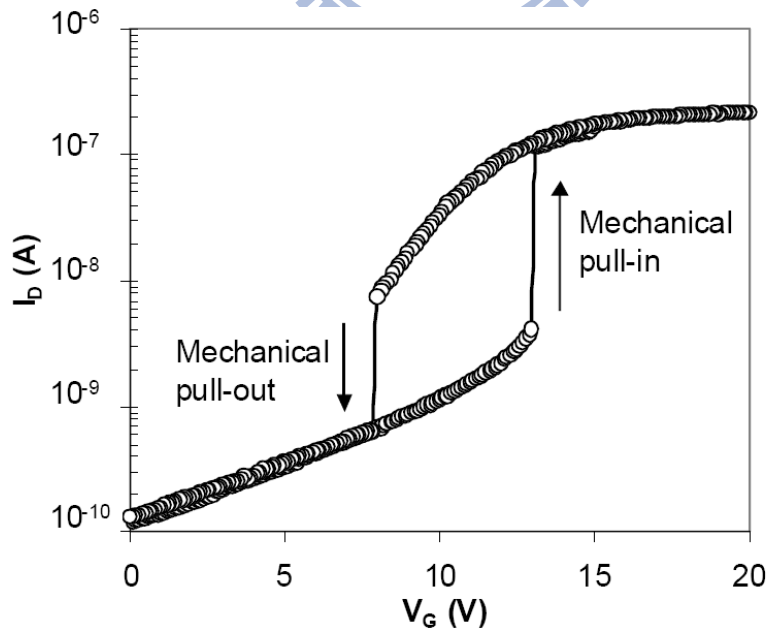


Figure 1.15. The mechanical hysteresis cycle of an SG-MOSFET [30].

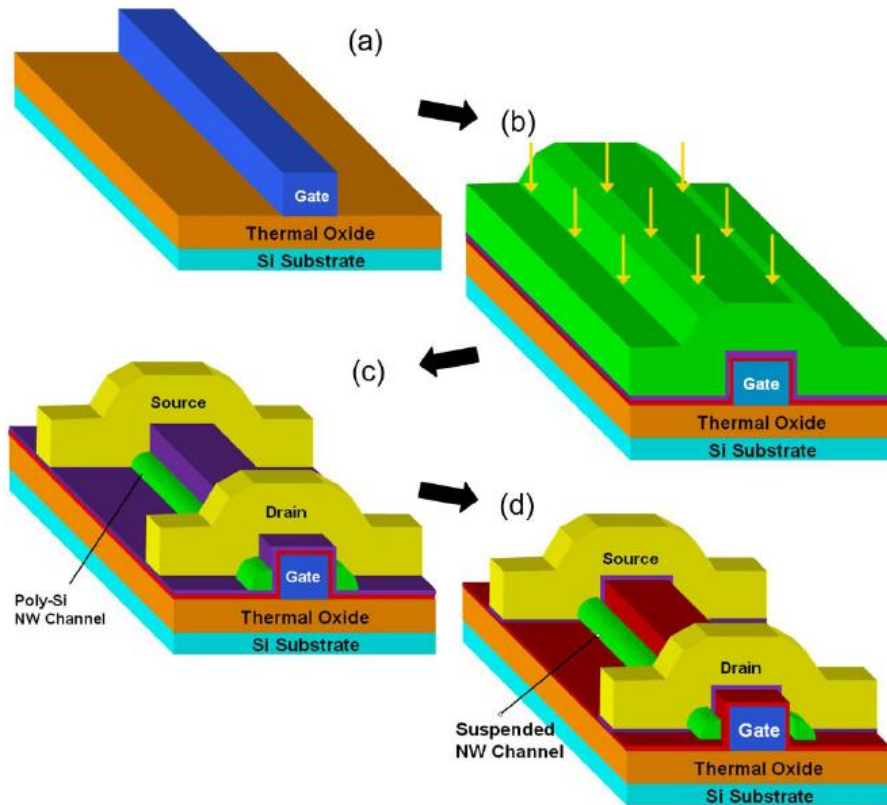


Figure 1.16. The major fabrication steps of the suspended poly-Si NW channel device with side-gated configuration [20]. (a) Gate definition. (b) Gate dielectric deposition, poly-Si channel deposition and S/D implantation. (c) S/D definition. (d) Air gap formation.

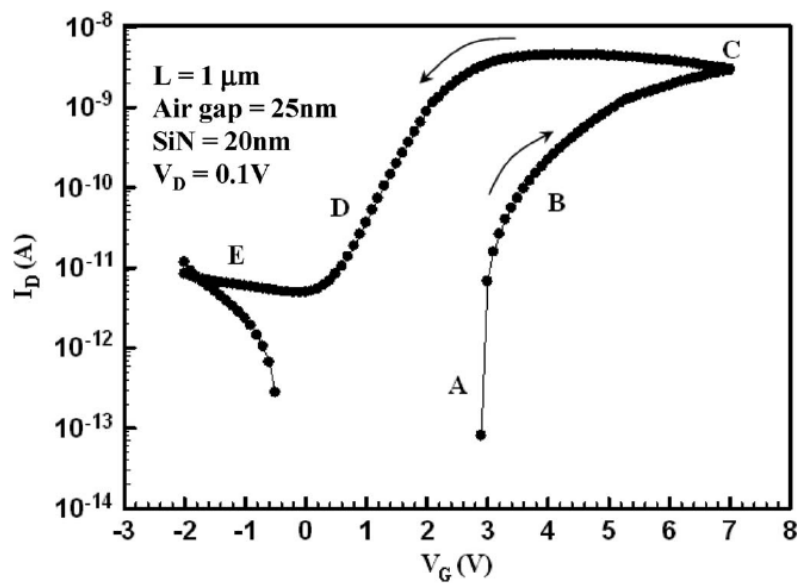


Figure 1.17. The basic electrical characteristics of suspended NW channel device [20].

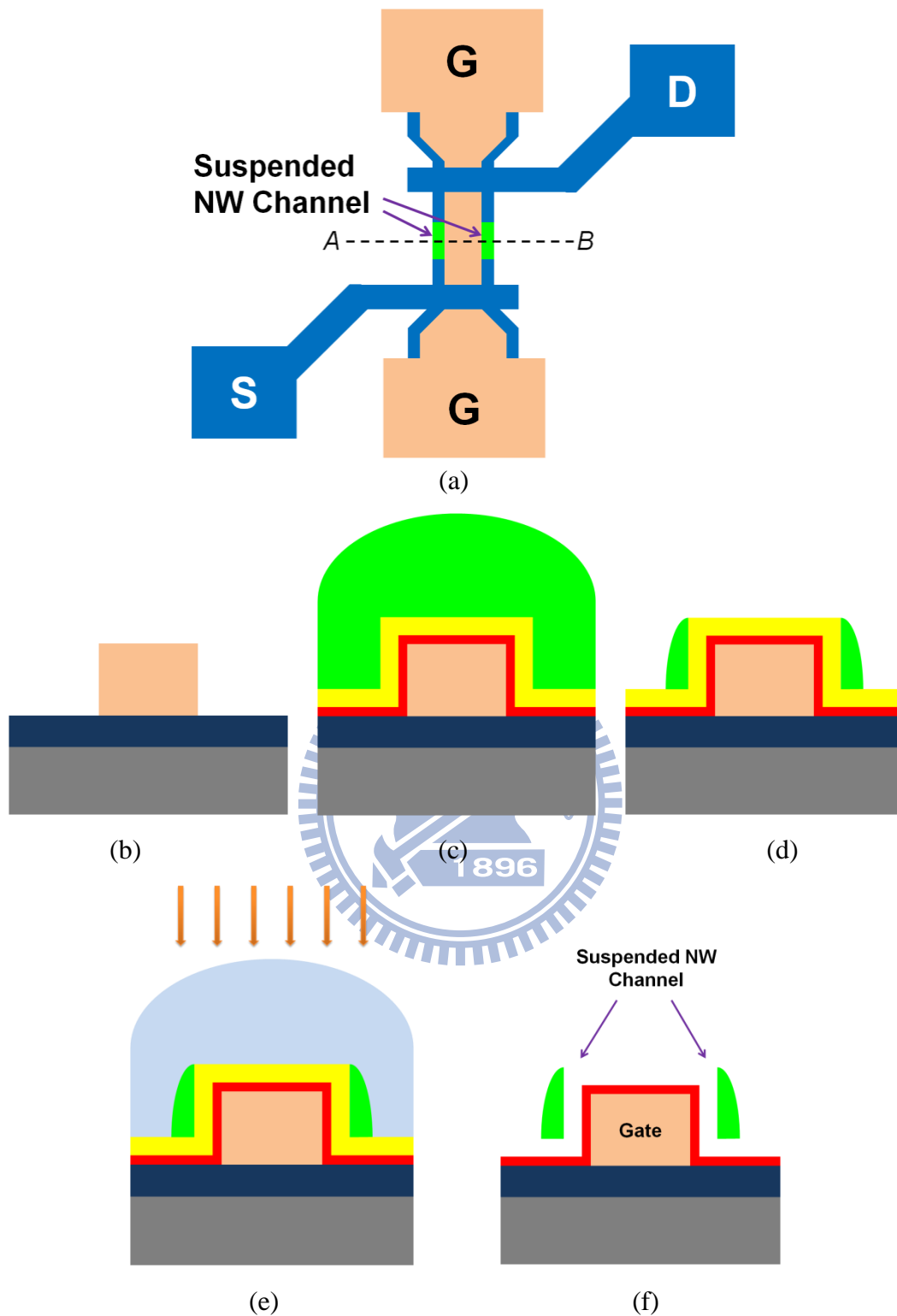
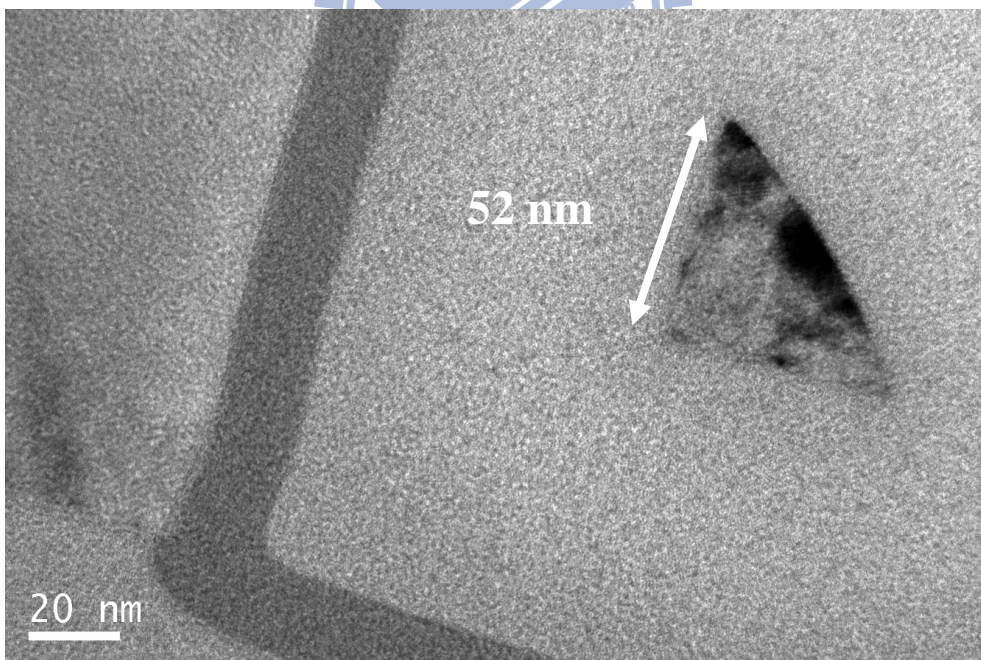
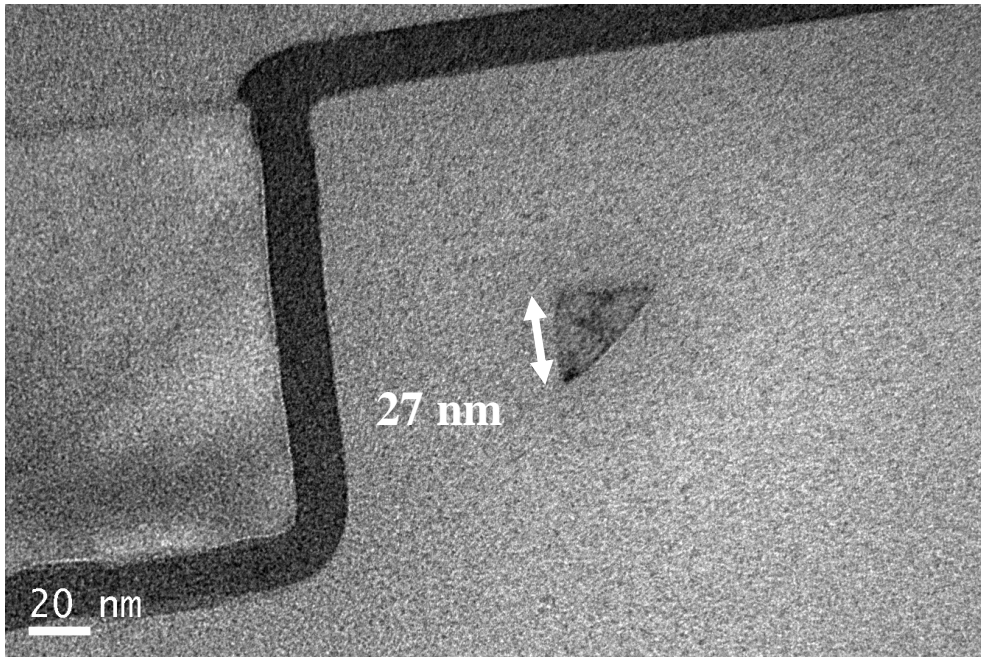


Figure 2.1. Key fabrication steps of suspended NW channel TFTs. (a) The top view of the suspended NW channel TFTs. (b) Formation of *in-situ* doped poly gate. (c) Deposition of silicon nitride, TEOS and  $\alpha$ -Si channel with SPC. (d) Formation of S/D regions and sidewall spacer NW channels by RIE. (e) Channel region definition and S/D implantation. (f) Air gap formation. Note that, figures in (b) to (f) are cross-sectional view from the cutline  $\overline{AB}$  in (a).





(b)

Figure 2.2. The cross-sectional TEM images of suspended NW channel from the outline  $\overline{AB}$  indicated in Fig. 2.1 (a) with different over-etch time. (a) 28 sec. (b) 22 sec.

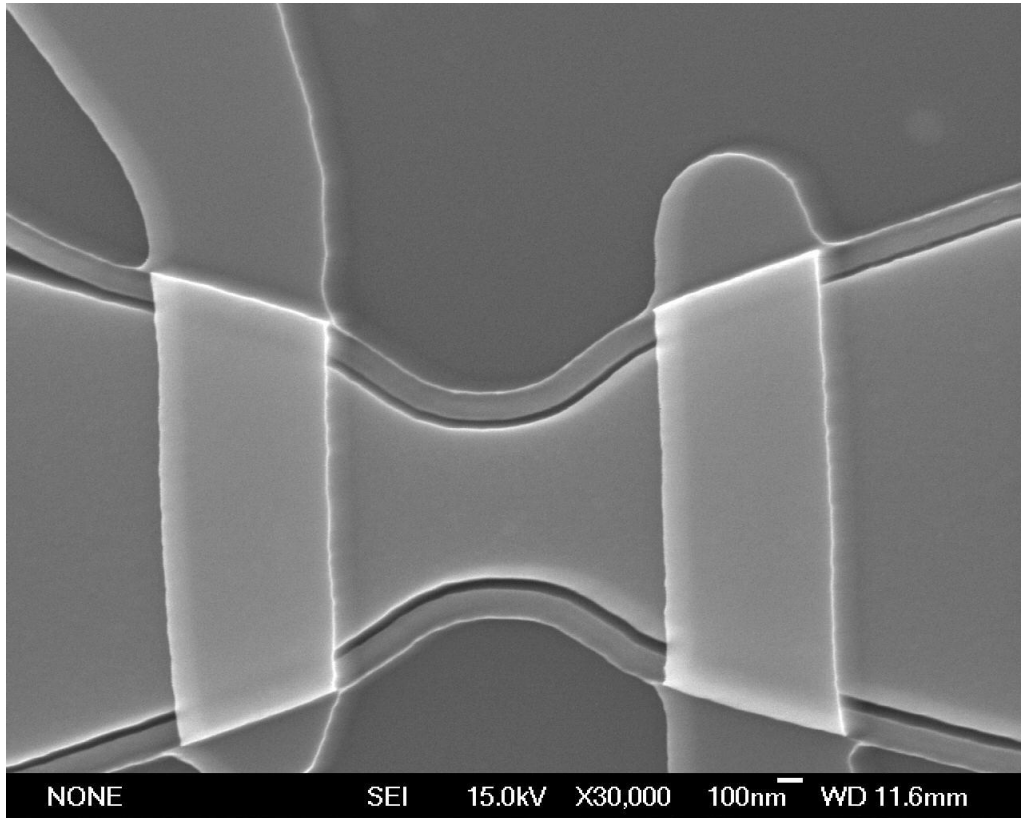


Figure 2.3. The top view of suspended-NW-channel TFT taken by SEM.

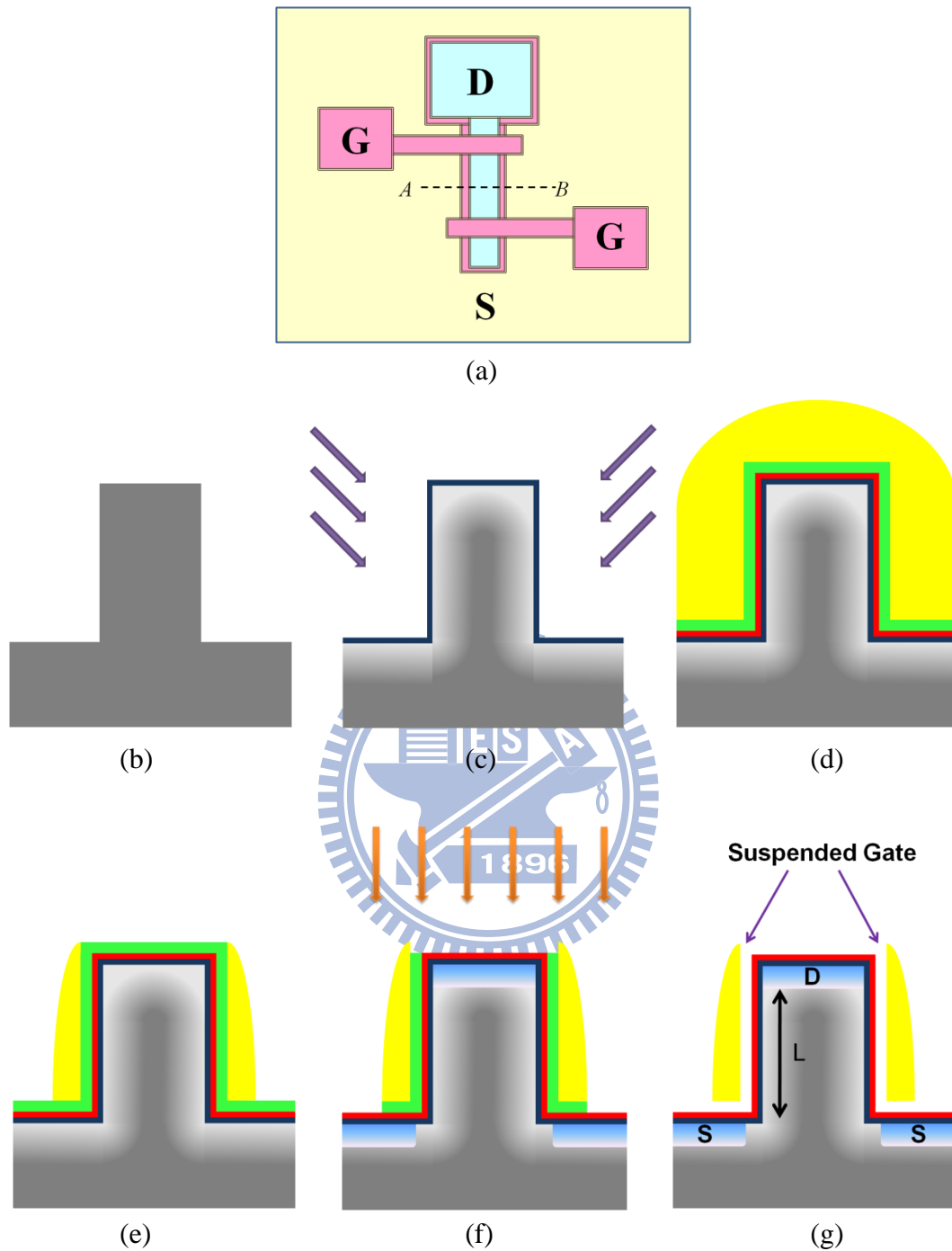
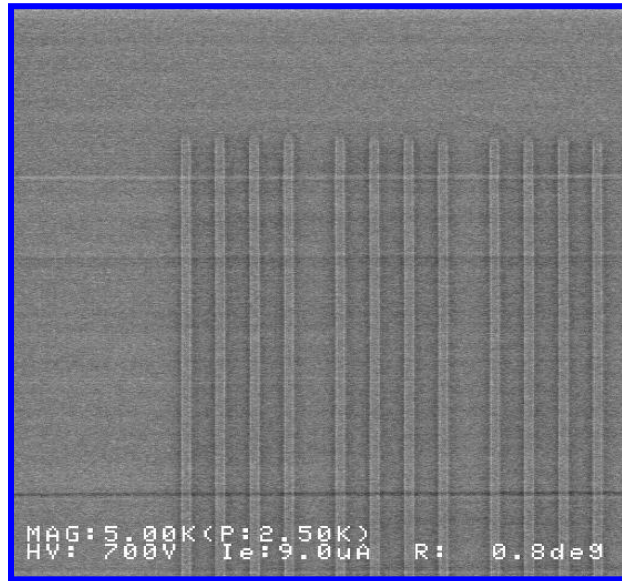
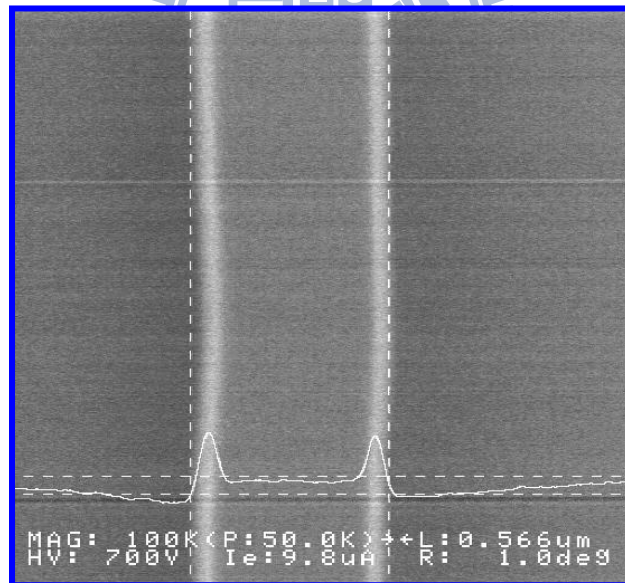


Figure 2.4. Key fabrication steps of SG-VMOS devices. (a) The top view of SG-VMOS device. (b) Vertical channel patterning by anisotropic plasma etching. (c) Re-oxidation and tilt sidewall channel implantation. (d) Formation of dry oxide, silicon nitride and TEOS gate dielectric stack and *in-situ* doped poly gate. (e) Sidewall spacer gate electrode formation by RIE. (f) Removal of exposed TEOS layer by DHF wet etching and S/D implantation. (g) Air gap formation. Note that, figures in (b) to (g) are cross-sectional view from the cutline  $\overline{AB}$  in (a).

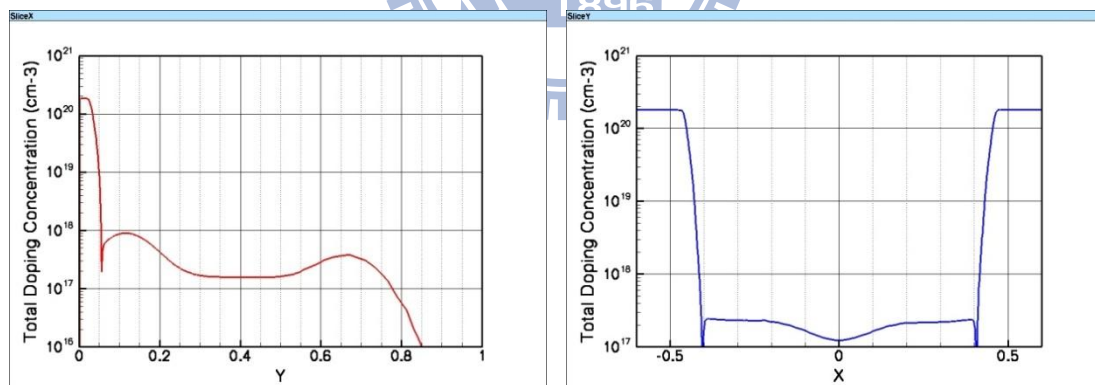
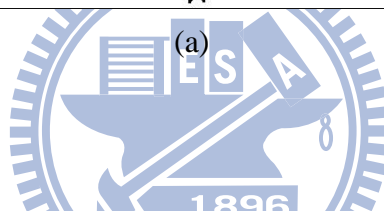
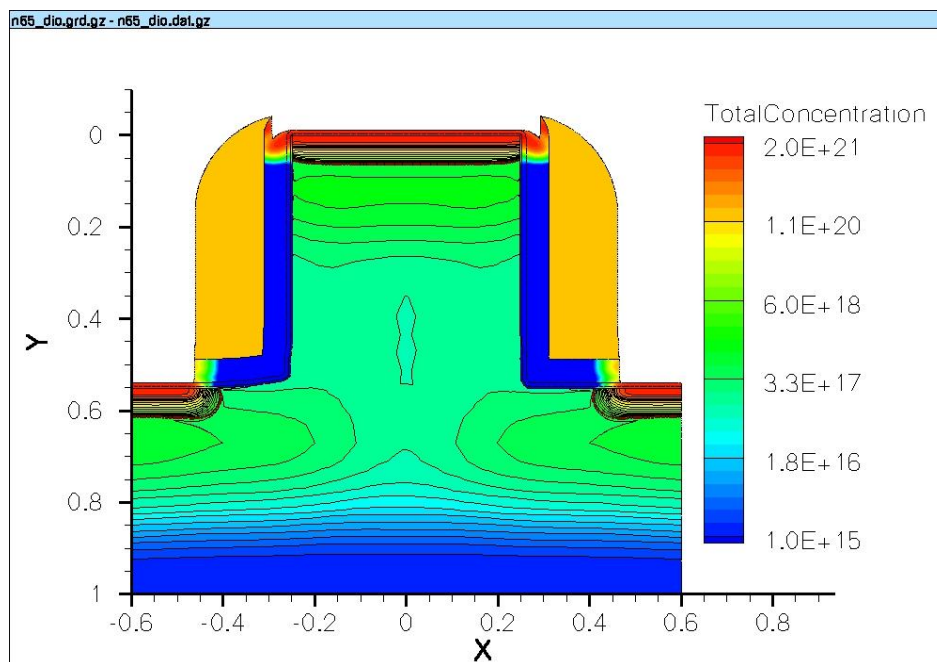


(a)



(b)

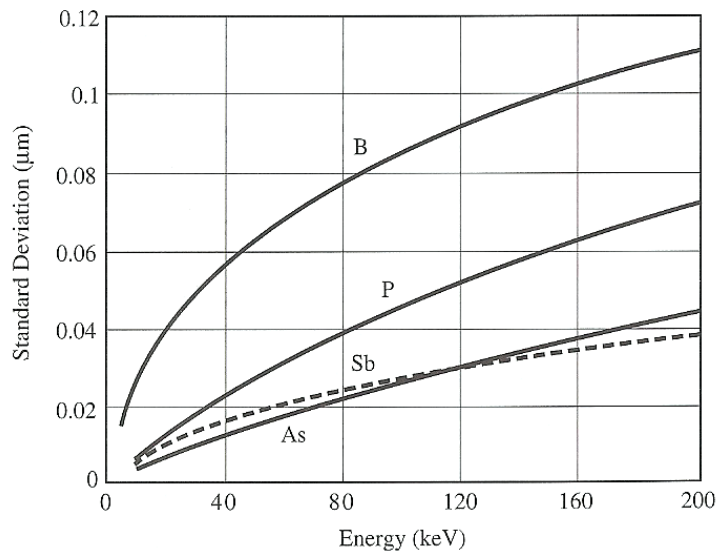
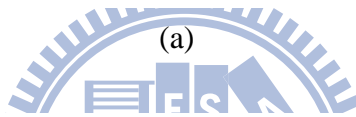
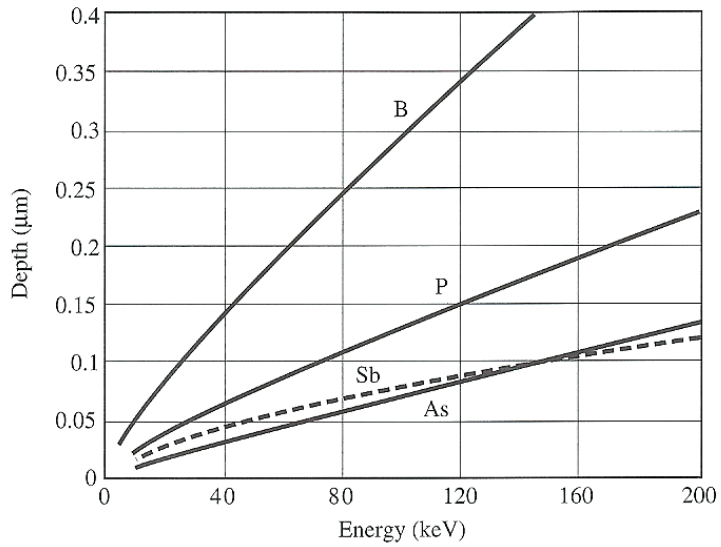
Figure 2.5. The top view of patterns in SEM bar region (a) and device region (b) after vertical channel definition taken by in-line SEM. The physical channel length is  $0.5 \mu\text{m}$ .



(b)

(c)

Figure 2.6. The simulated total doping concentration profile in our SG-VMOS with 50 nm sacrificial TEOS layer. The device channel length is 0.5 μm. (a) Along cutline  $\overline{AB}$  shown in Fig. 2.1. (b) Along y direction with x = -0.24 μm. (c) Along x direction with y = 0.57 μm.



(b)

Figure 2.7. The ion implantation projection range (a) and standard deviation of projection range (b) of various common dopants in crystalline silicon tilted and rotated to simulate a random direction [39].

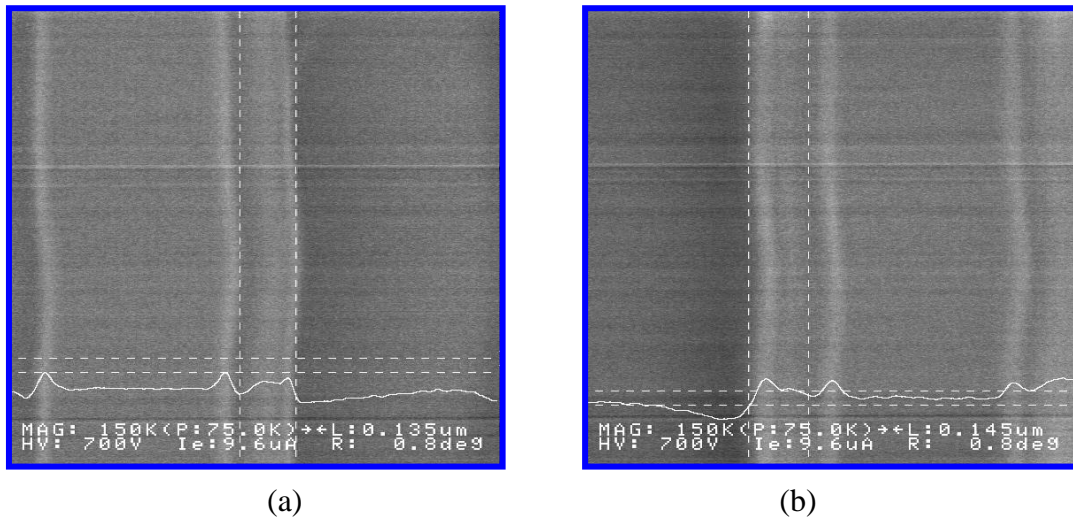


Figure 2.8. The in-line SEM images of the device patterns after sidewall spacer gate definition and DHF wet etching. (a) and (b) show the right-hand side and left-hand side images of the device structure, respectively. The device channel length is 0.5  $\mu\text{m}$ .

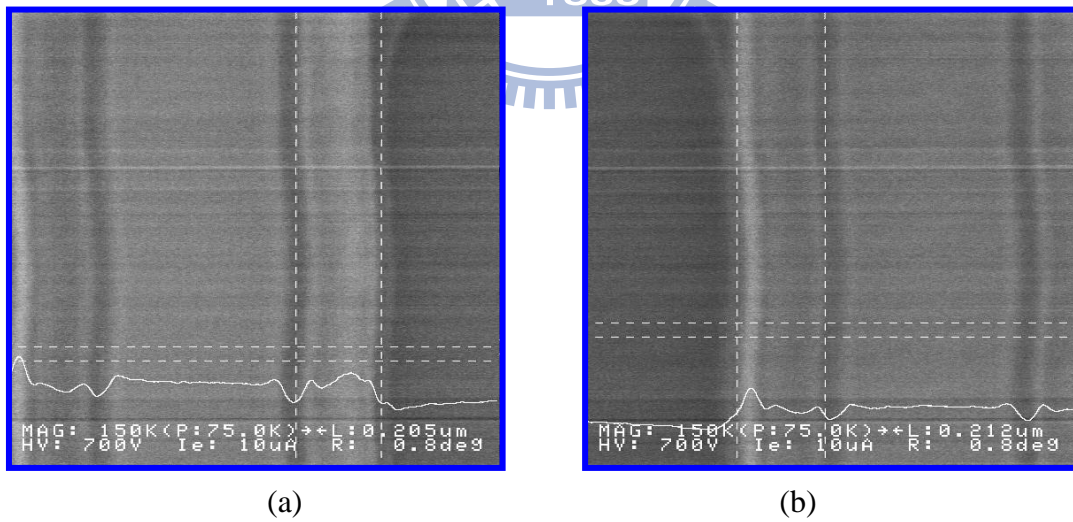


Figure 2.9. The in-line SEM images of the patterns in the device region after sidewall spacer gate definition and DHF wet etching. (a) and (b) show the right-hand side and left-hand side images of the device structure, respectively. The device channel length is 1  $\mu\text{m}$ .

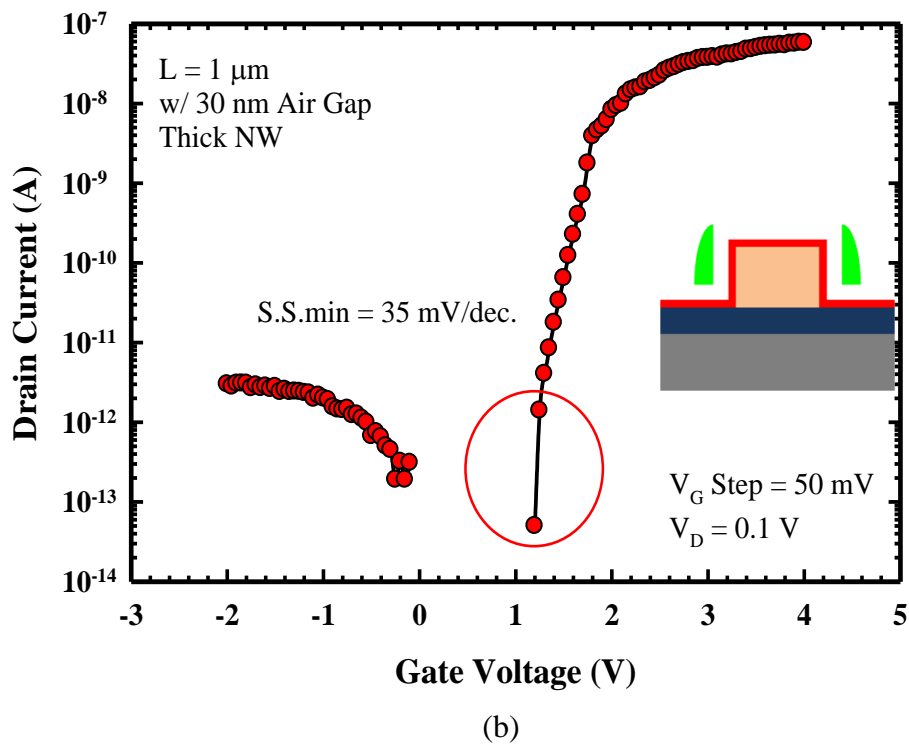
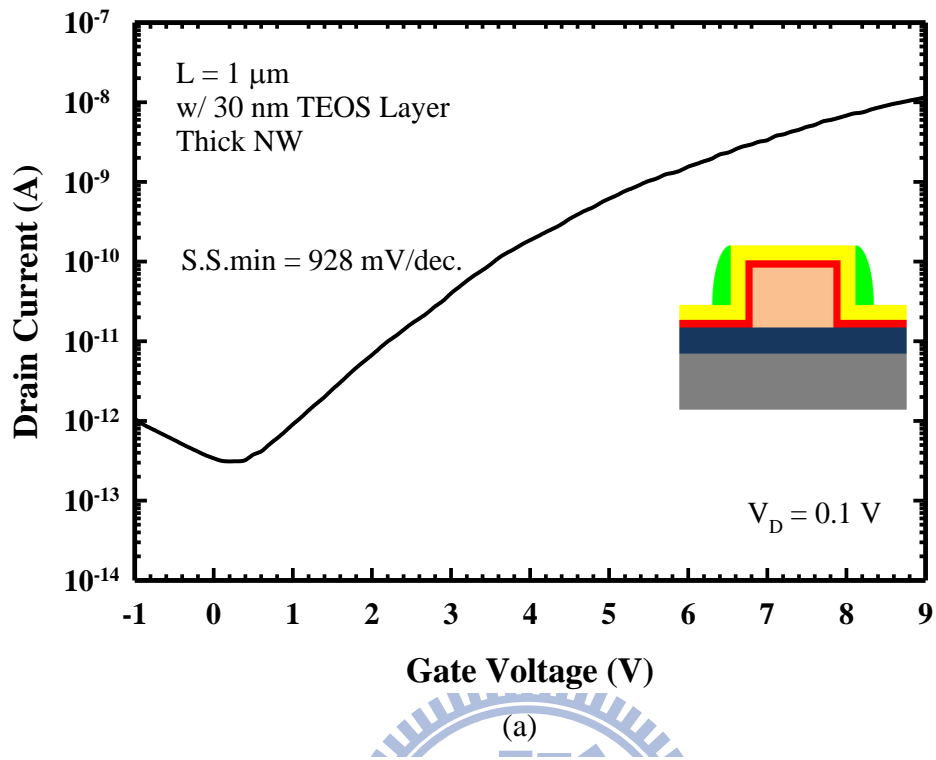


Figure 3.1.  $I_D$ - $V_G$  curves of (a) conventional TFT and (b) suspended-NW-channel TFT.



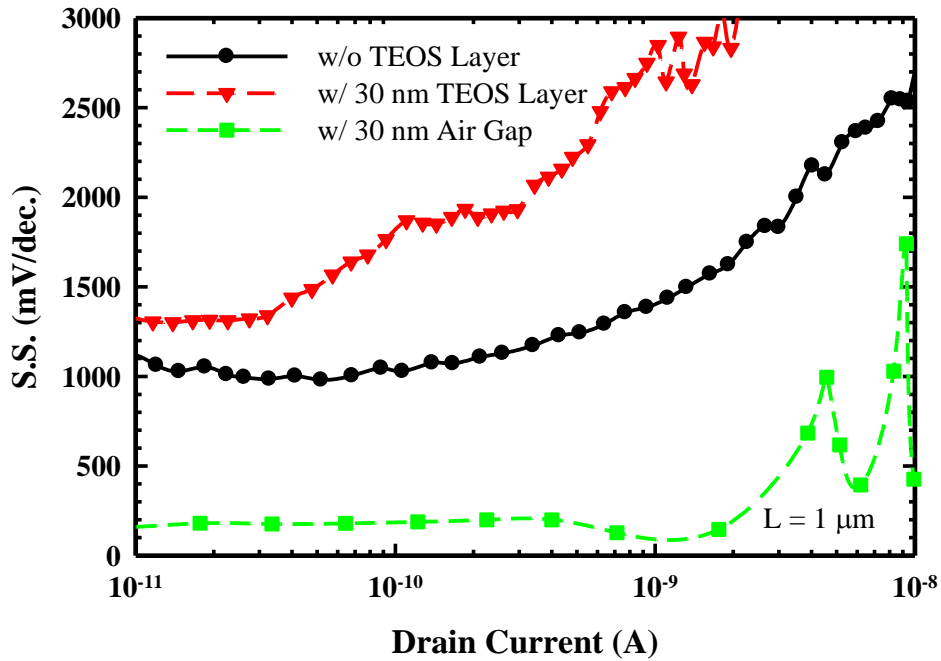


Figure 3.2. The plot of S.S. versus  $I_D$  for the devices with three different structures, *i.e.*, without sacrificial TEOS layer, before stripping the TEOS layer and after stripping the TEOS layer.

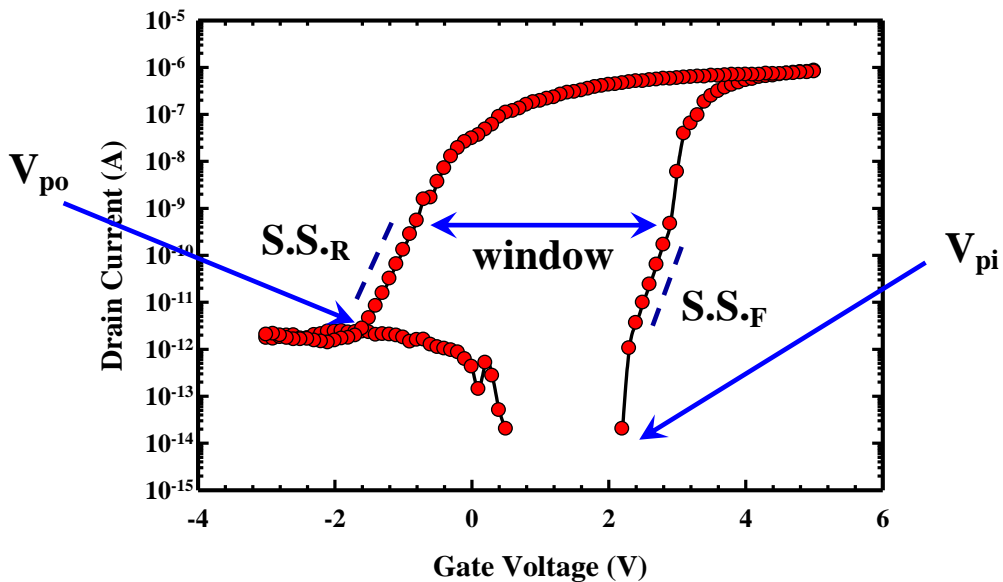


Figure 3.3. The electrical parameters of a suspended-NW-channel TFT including the pull-in voltage ( $V_{pi}$ ), the pull-out voltage ( $V_{po}$ ) and the S.S. under the forward and reverse sweeping measurements.

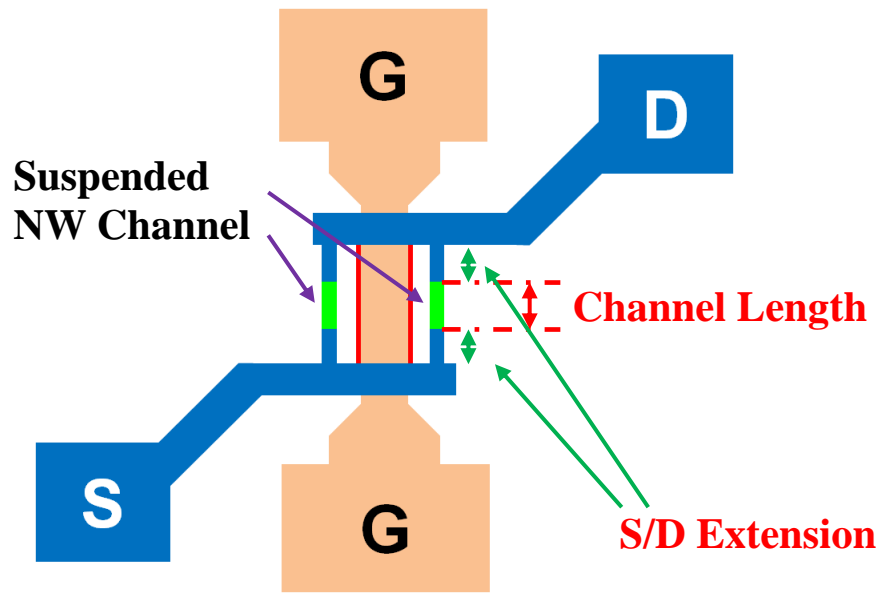


Figure 3.4. Schematic showing the definition of structural parameters of the suspended-NW-channel TFTs including the channel length and the S/D extension length.

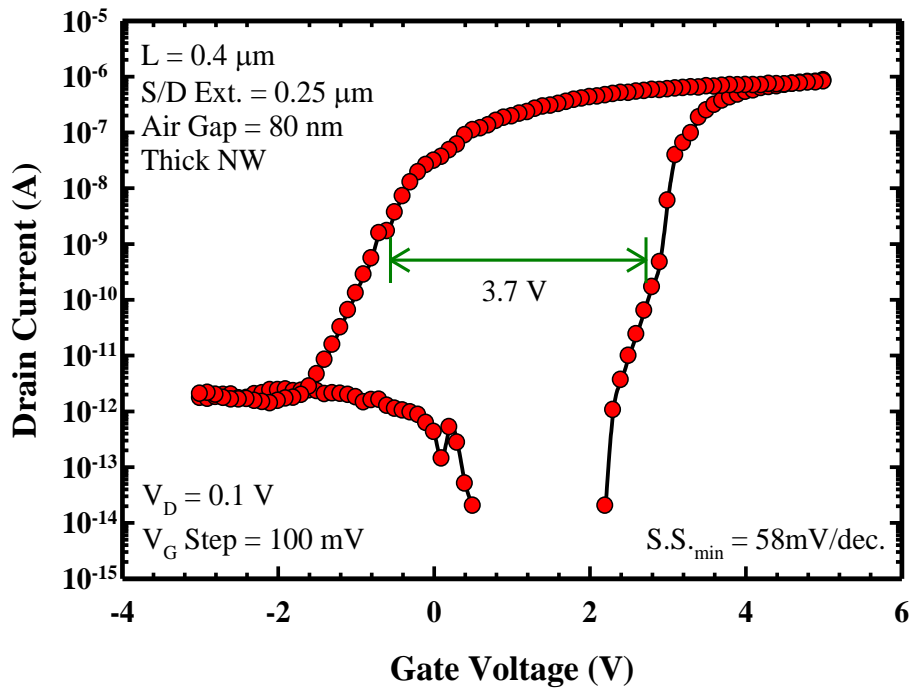


Figure 3.5. The hysteresis characteristics of a suspended-NW-channel TFT under consecutive forward and reverse sweeping measurements.

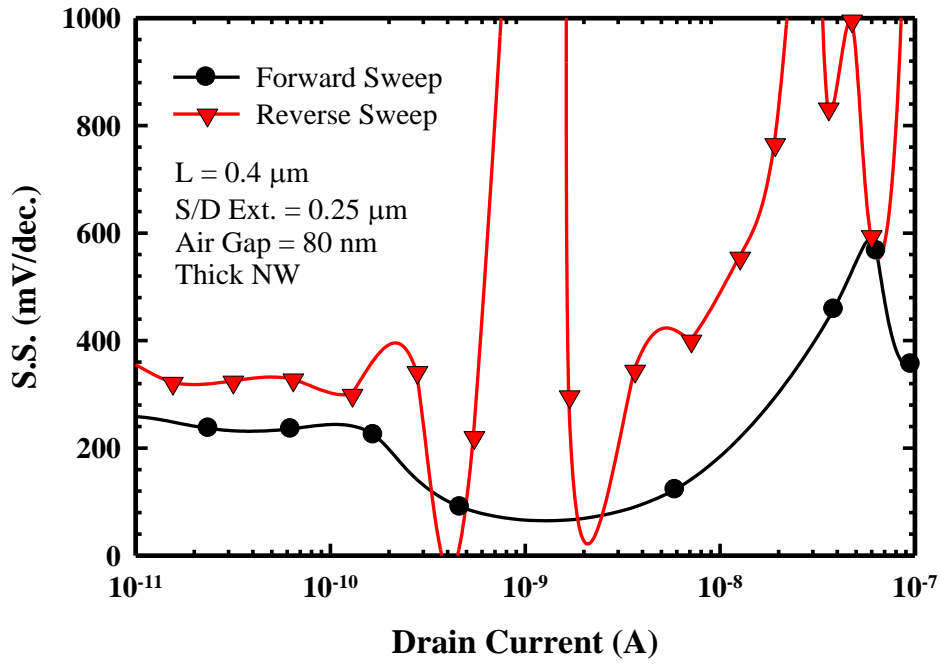


Figure 3.6. The plot of S.S. versus  $I_D$  for a suspended-NW-channel TFT under consecutive forward and reverse sweeping measurements.

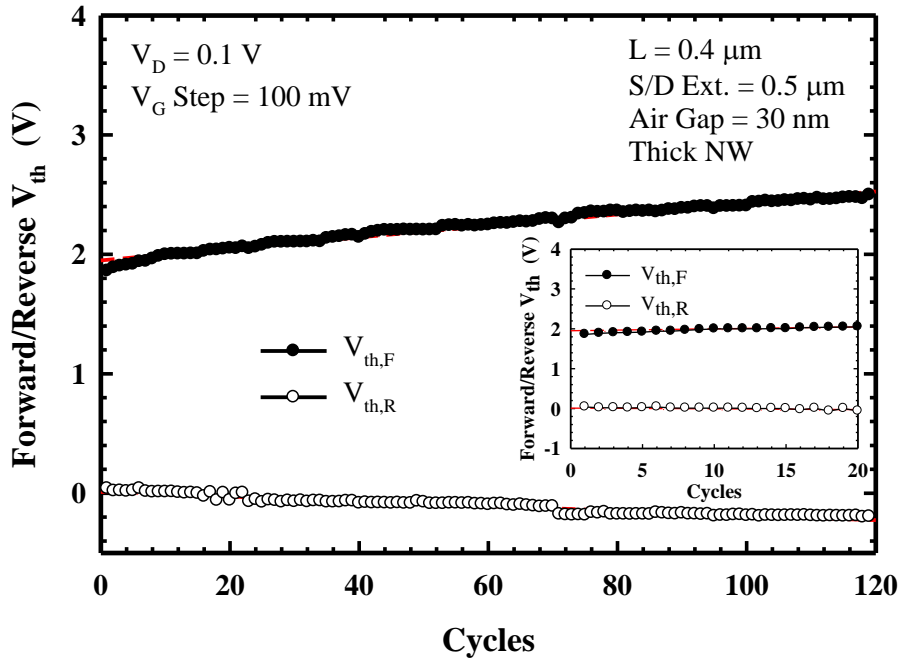


Figure 3.7. The endurance characteristics for a suspended-NW-channel TFT under consecutive cycling measurements.

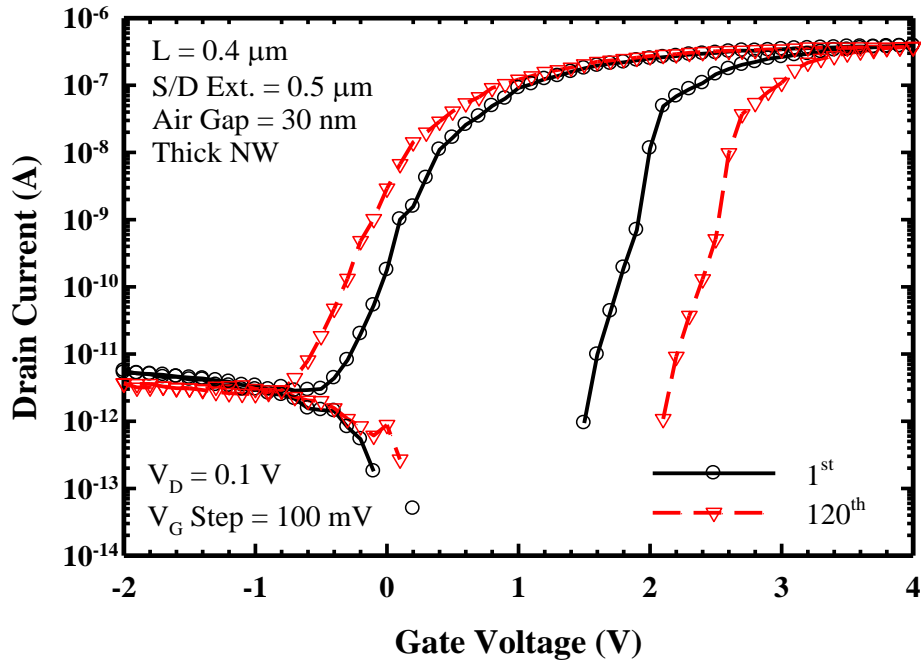


Figure 3.8. The hysteresis curves of a suspended-NW-channel TFT measured before (i.e., as fresh) and after 120 times cyclings.

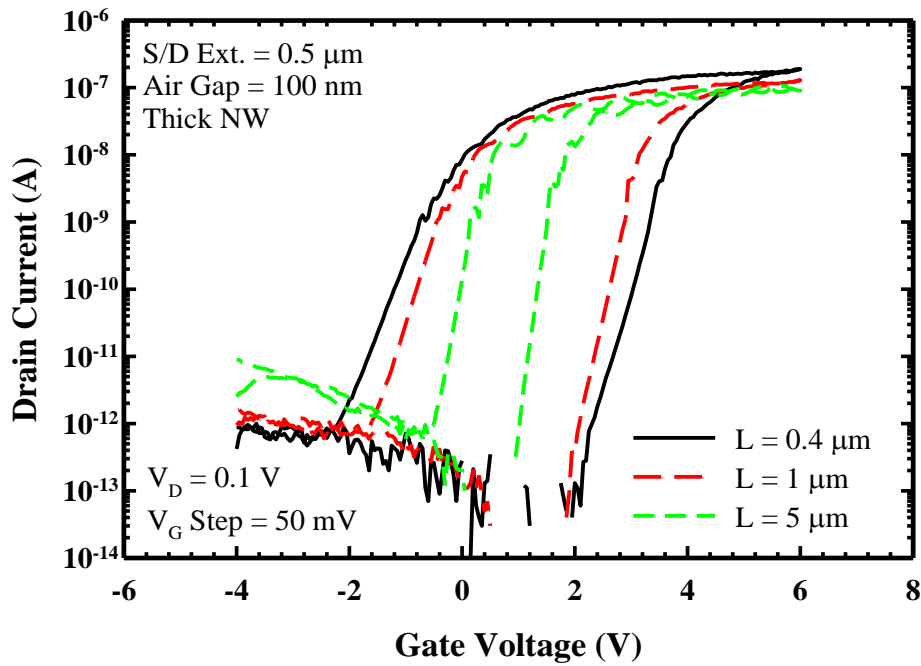


Figure 3.9. The hysteresis curves of the suspended-NW-channel TFTs with channel length of  $0.4 \mu\text{m}$ ,  $1 \mu\text{m}$  and  $5 \mu\text{m}$ , respectively.

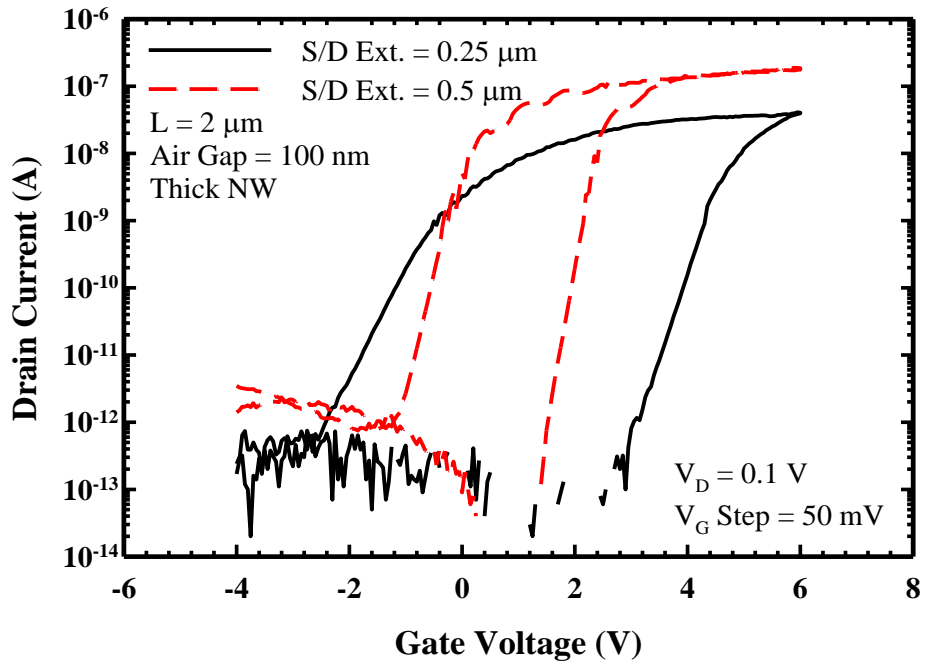


Figure 3.10. The hysteresis curves of the suspended-NW-channel TFTs with S/D extension length of  $0.25 \mu\text{m}$  and  $0.5 \mu\text{m}$ , respectively.

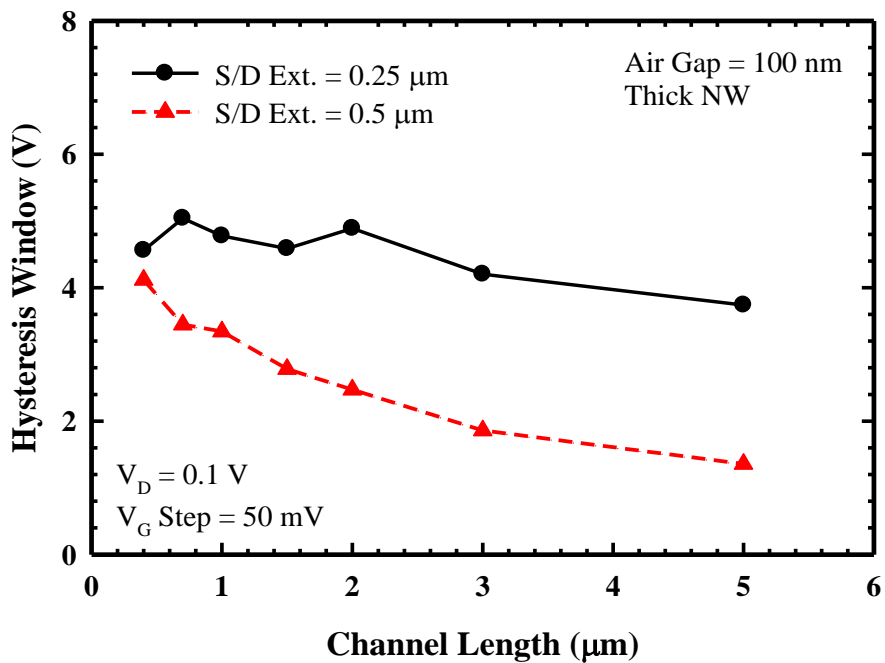


Figure 3.11. The plot of hysteresis window versus channel length for the suspended-NW-channel TFTs with S/D extension length of  $0.25 \mu\text{m}$  and  $0.5 \mu\text{m}$ , respectively.

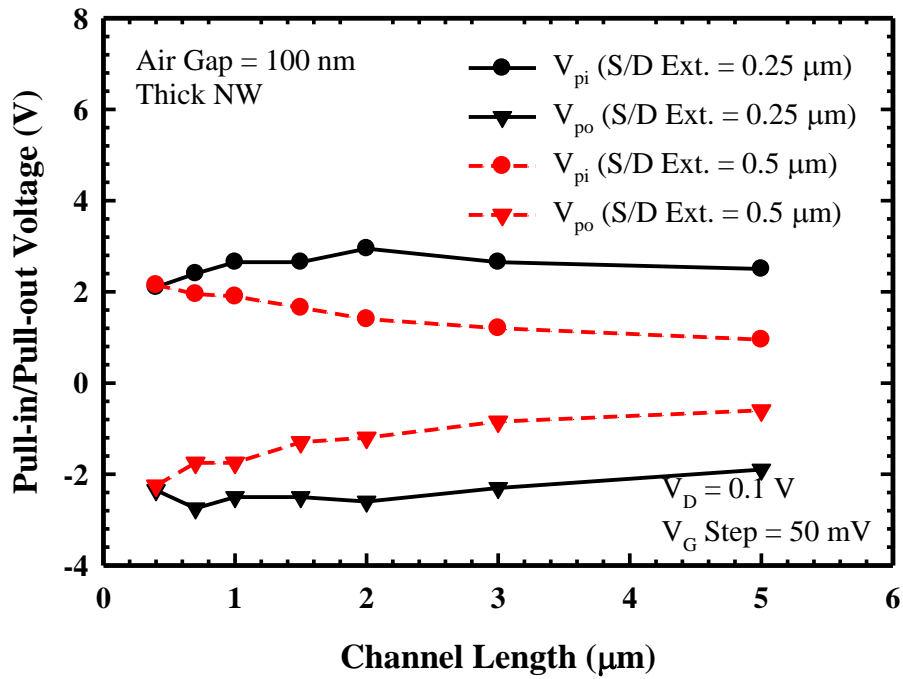


Figure 3.12. The plot of  $V_{pi}$  and  $V_{po}$  versus channel length for the suspended-NW-channel TFTs with S/D extension length of 0.25 μm and 0.5 μm, respectively.

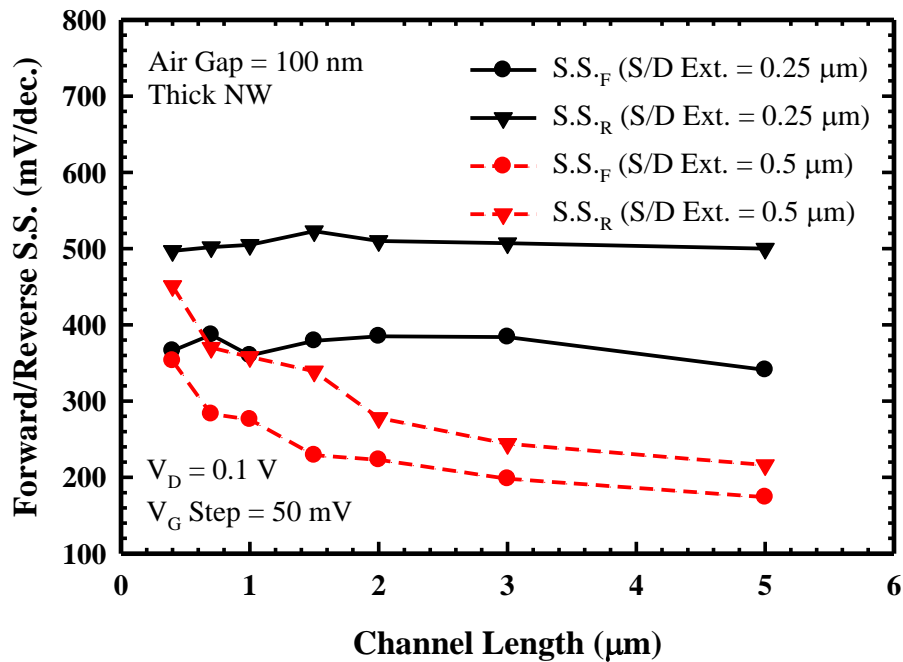


Figure 3.13. The plot of  $S.S_F$  and  $S.S_R$  versus channel length for the suspended-NW-channel TFTs with S/D extension length of 0.25 μm and 0.5 μm, respectively.

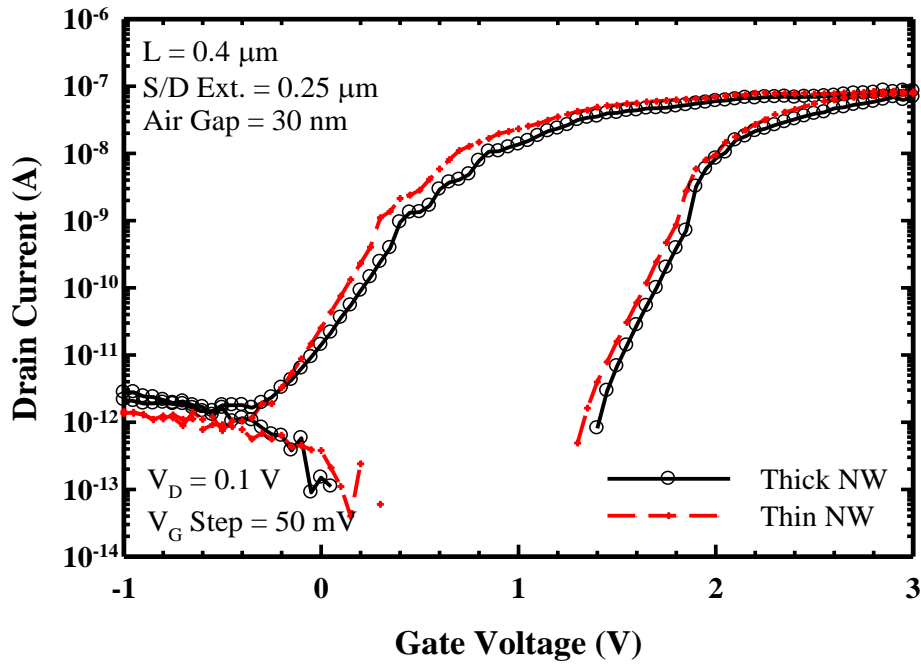


Figure 3.14. The hysteresis curves of the suspended-NW-channel TFTs with two different NW thicknesses.

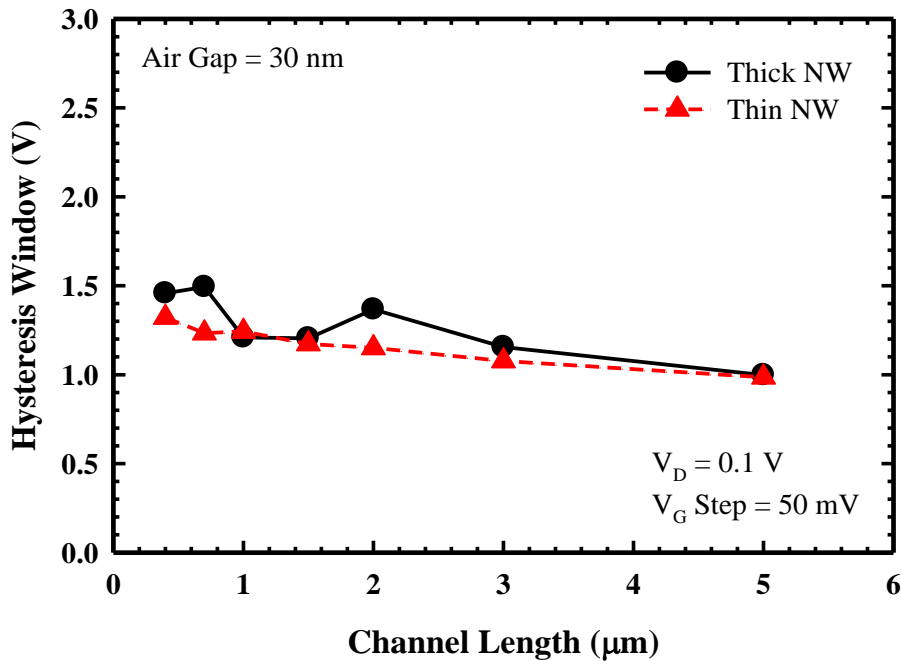


Figure 3.15. The plot of hysteresis window versus channel length for the suspended-NW-channel TFTs with two different NW thicknesses.

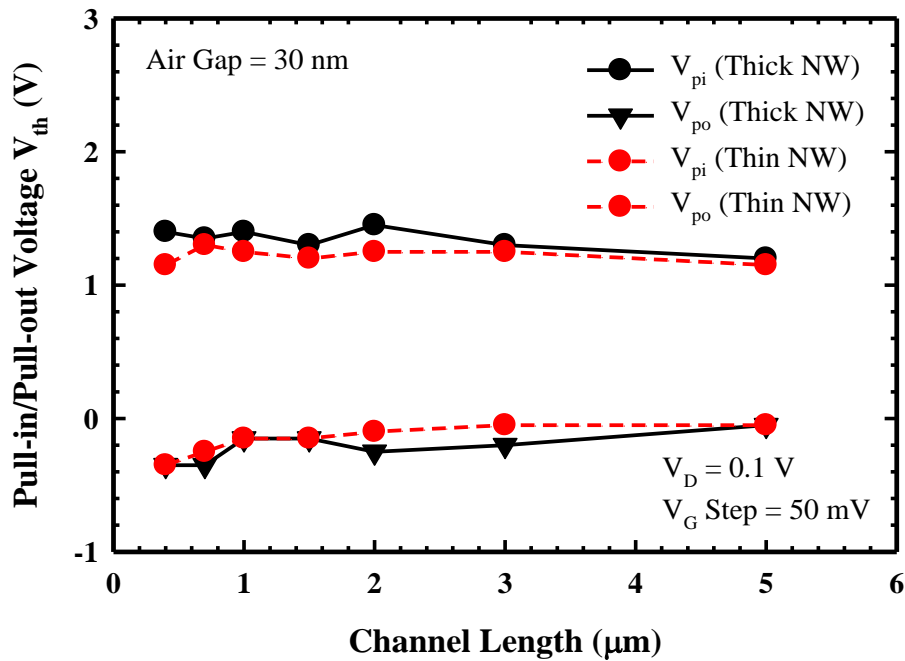


Figure 3.16. The plot of  $V_{pi}$  and  $V_{po}$  versus channel length for the suspended-NW-channel TFTs with two different NW thicknesses.

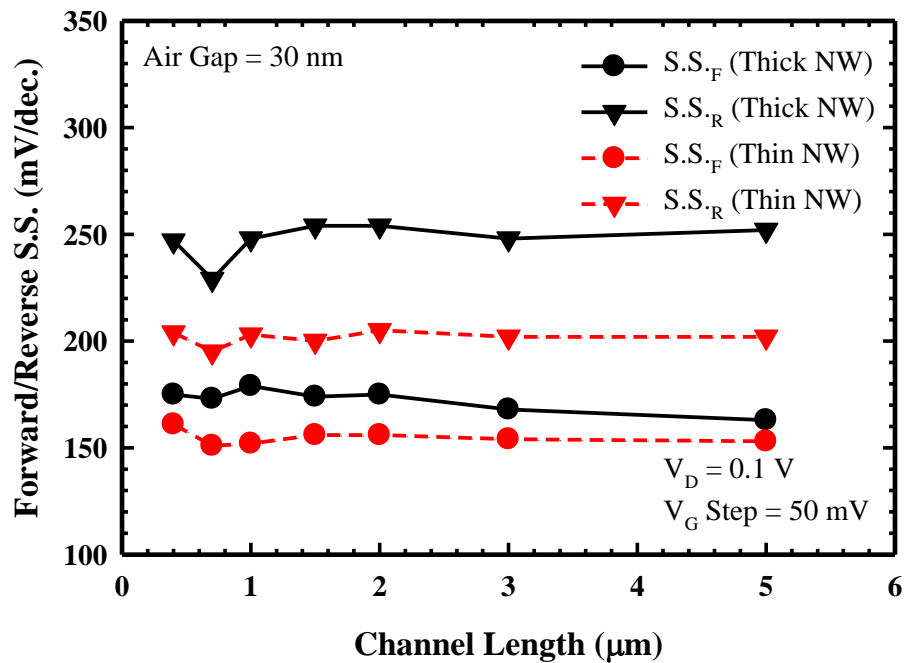


Figure 3.17. The plot of  $S.S_F$  and  $S.S_R$  versus channel length for the suspended-NW-channel TFTs with two different NW thicknesses.



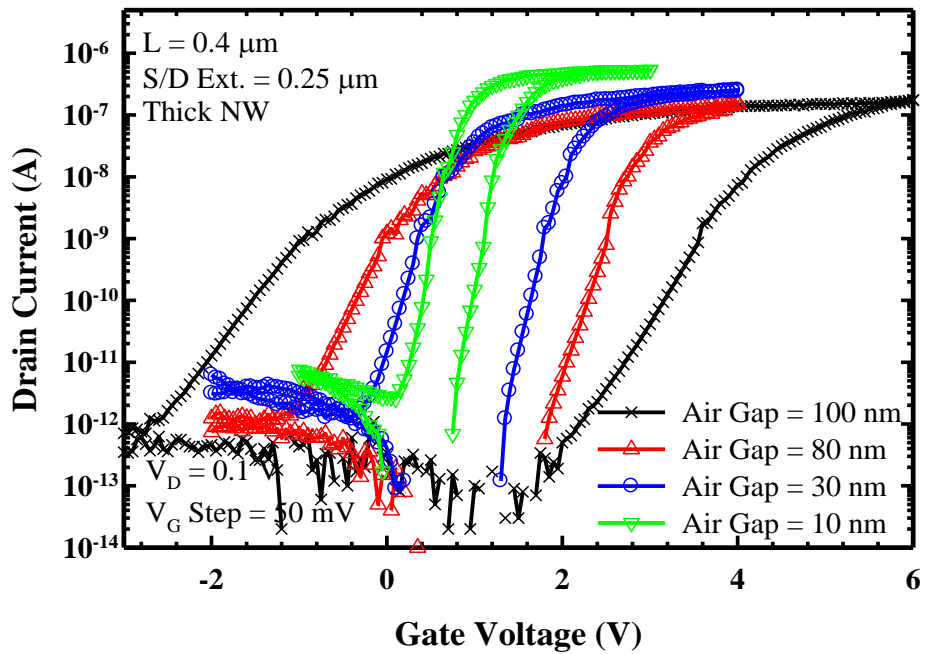


Figure 3.18. The hysteresis curves of the suspended-NW-channel TFTs with air gap thickness of 100 nm, 80 nm, 30 nm and 10 nm, respectively.

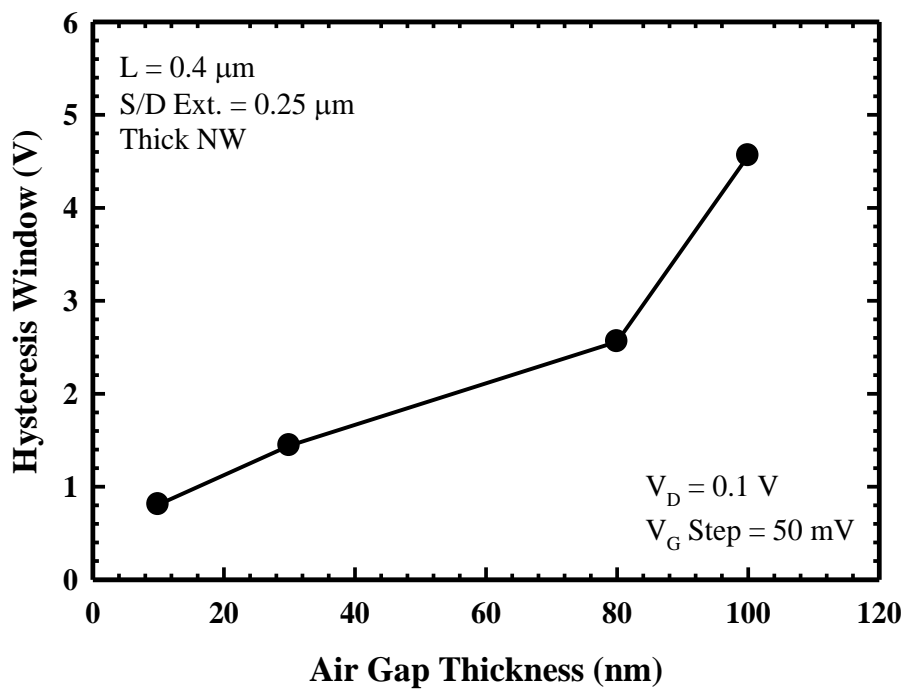


Figure 3.19. The plot of hysteresis window versus air gap thickness for the suspended-NW-channel TFTs.

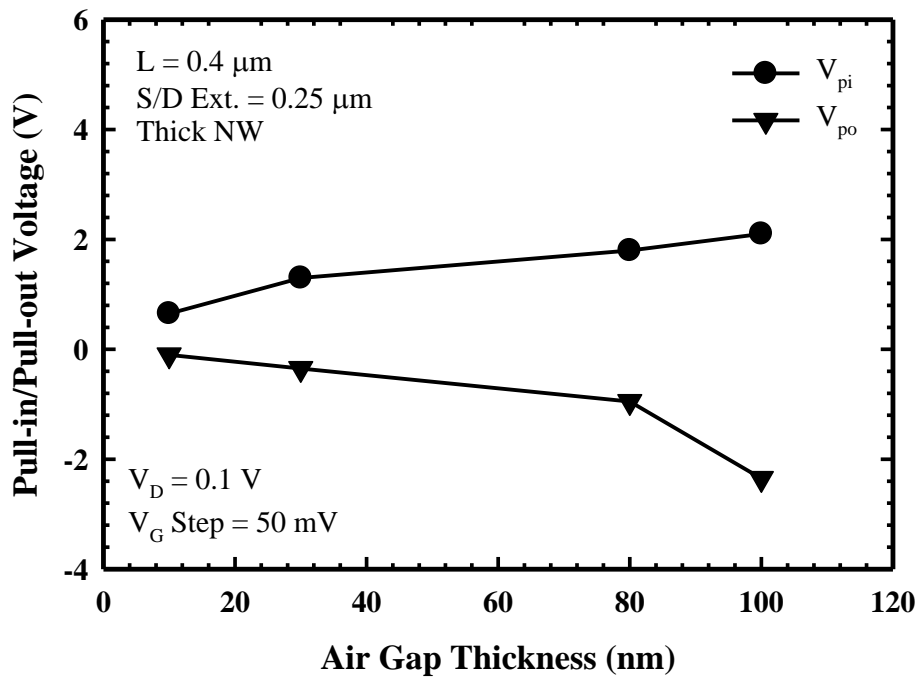


Figure 3.20. The plot of  $V_{pi}$  and  $V_{po}$  versus air gap thickness for the suspended-NW-channel TFTs.

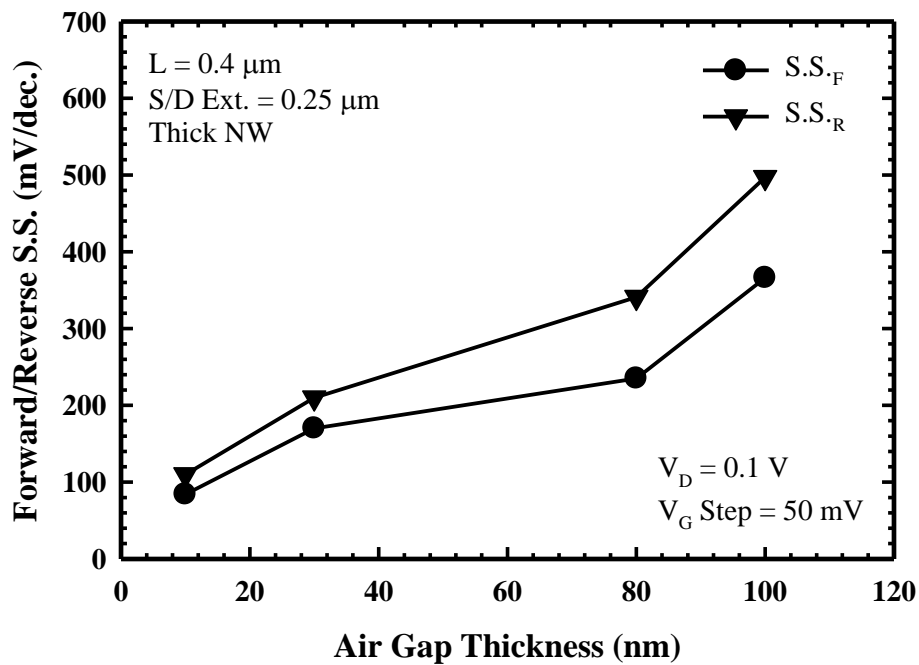


Figure 3.21. The plot of  $S.S._F$  and  $S.S._R$  versus air gap thickness for the suspended-NW-channel TFTs.

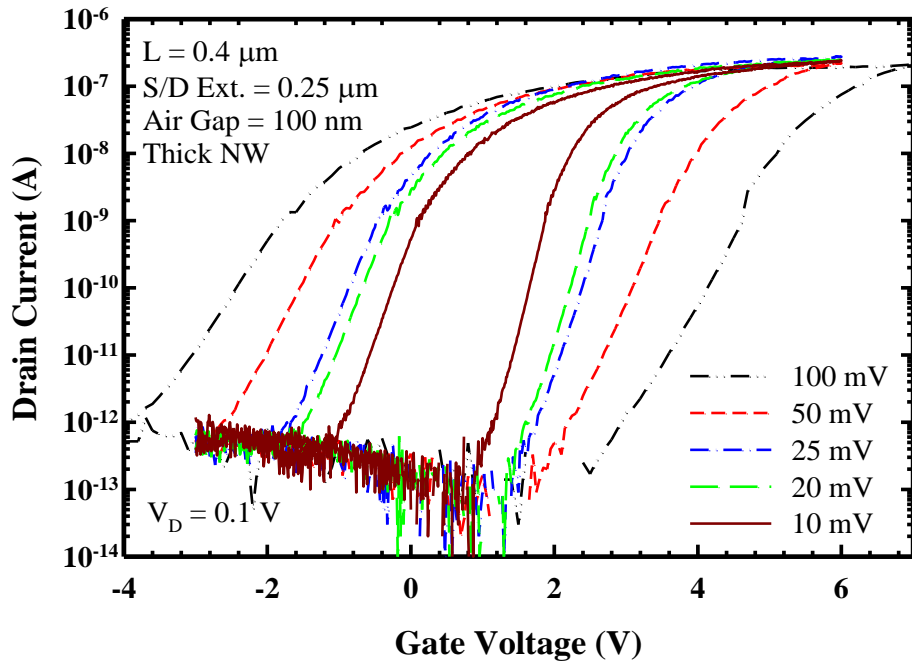


Figure 3.22. The hysteresis curves of the suspended-NW-channel TFTs operated at different sweeping speed by modulating the increment of  $V_G$  per step.

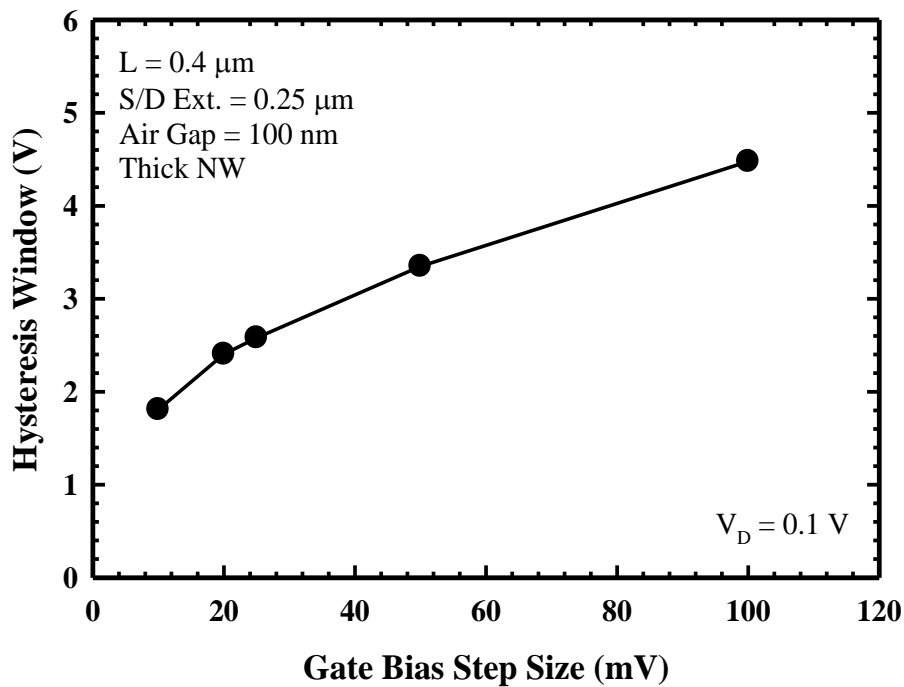


Figure 3.23. The plot of hysteresis window versus the increment of  $V_G$  per step during measurements for the suspended-NW-channel TFTs.

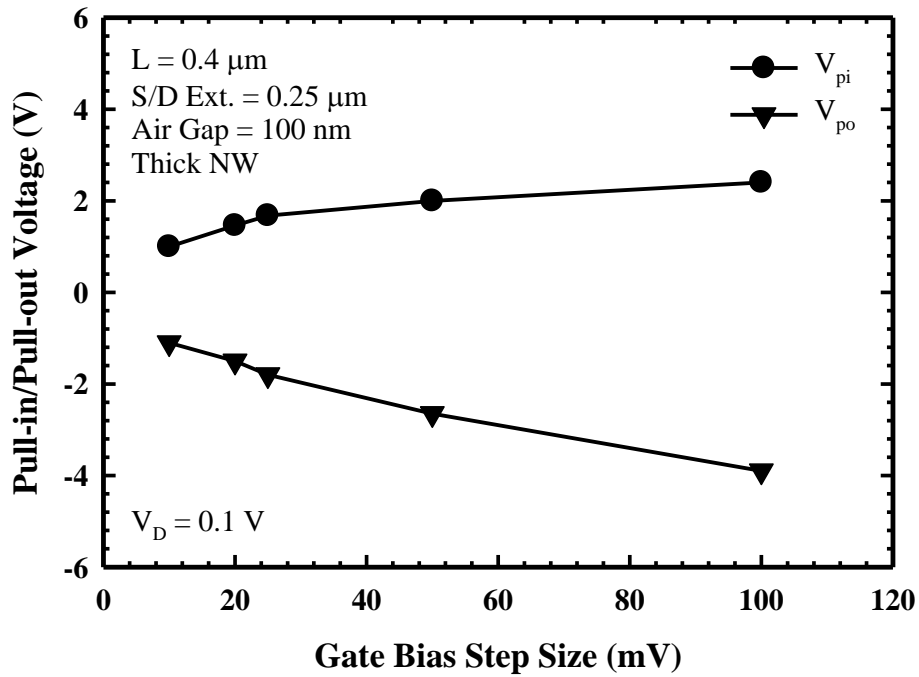


Figure 3.24. The plot of  $V_{pi}$  and  $V_{po}$  versus the increment of  $V_G$  per step during measurements for the suspended-NW-channel TFTs.

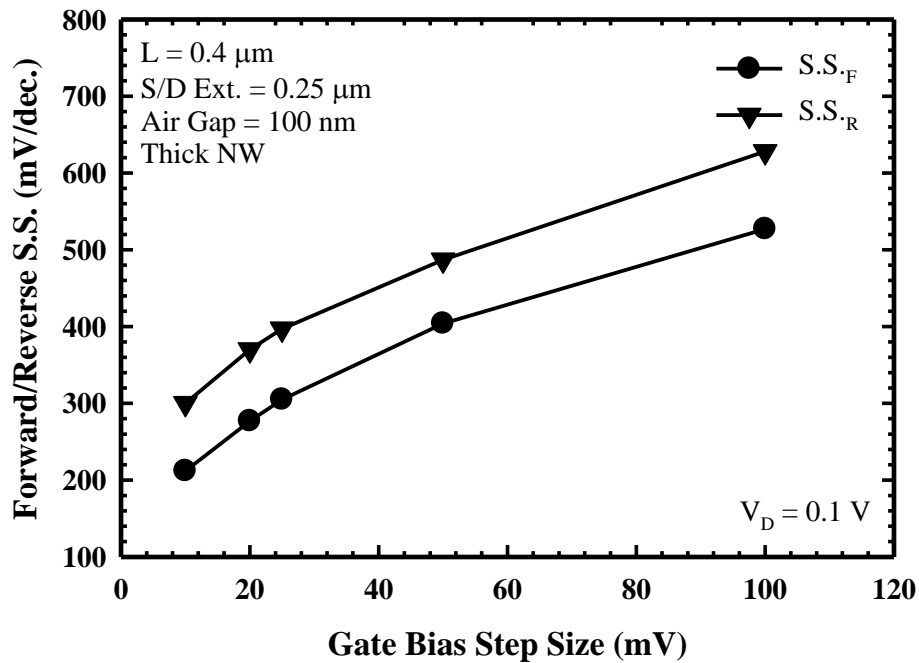


Figure 3.25. The plot of  $S.S._F$  and  $S.S._R$  versus the increment of  $V_G$  per step during measurements for the suspended-NW-channel TFTs.

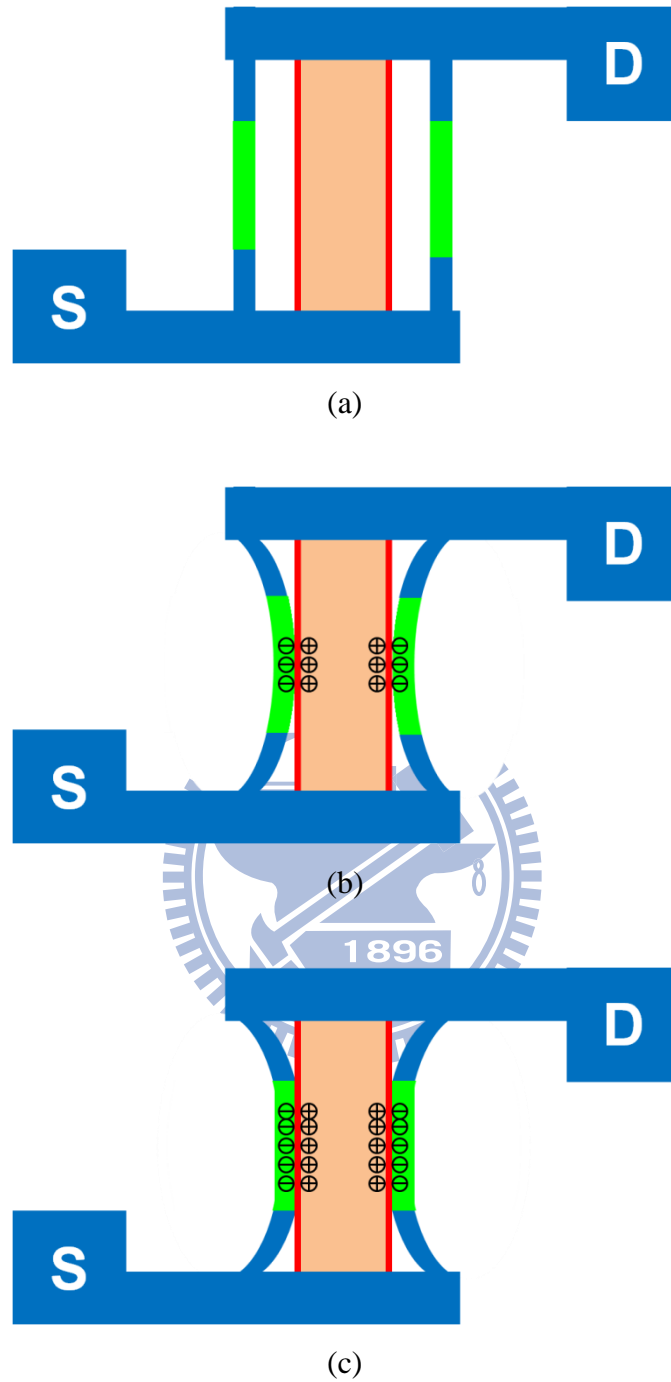


Figure 3.26. Various operation states of the suspended NW channels for the suspended-NW-channel TFTs. (a) The NW channels are suspended and separated from the gate with the air gap. (b) As  $V_G = V_{pi}$ , the central region of the NW channels begins to contact with the gate stack. (c) As  $V_G$  is further increased to turn the device into the ON state, most of the NW channels are in contact with the gate stack.

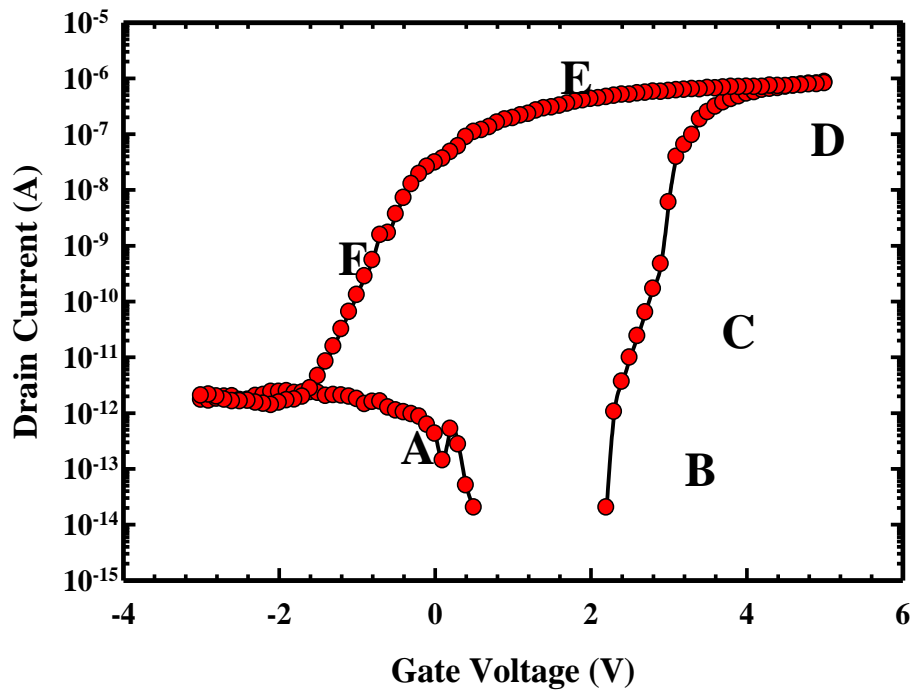


Figure 3.27. Various operation states of the suspended-NW-channel TFTs. A: The NW channels are suspended. B: The central region of NW channels begins to contact with the gate stack. C: Portion of the NW channels in contact with the gate stack gradually increases. D: ON state. E: The surface adhesion forces maintain the contact of NW channels with the gate stack, and the drain currents remains relatively high. F: The NW channels gradually detach from the gate stack.

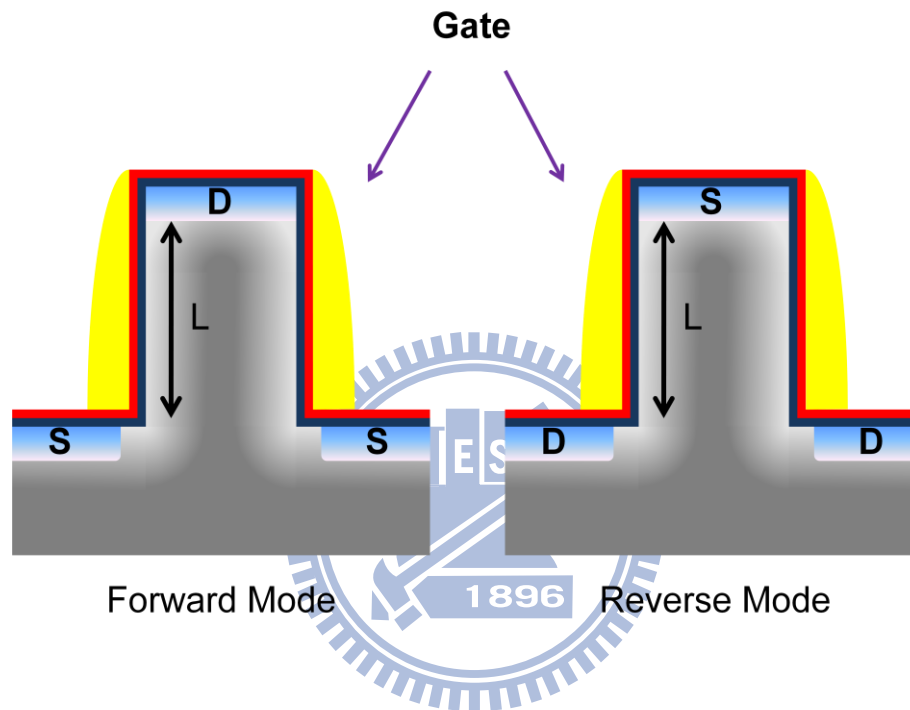
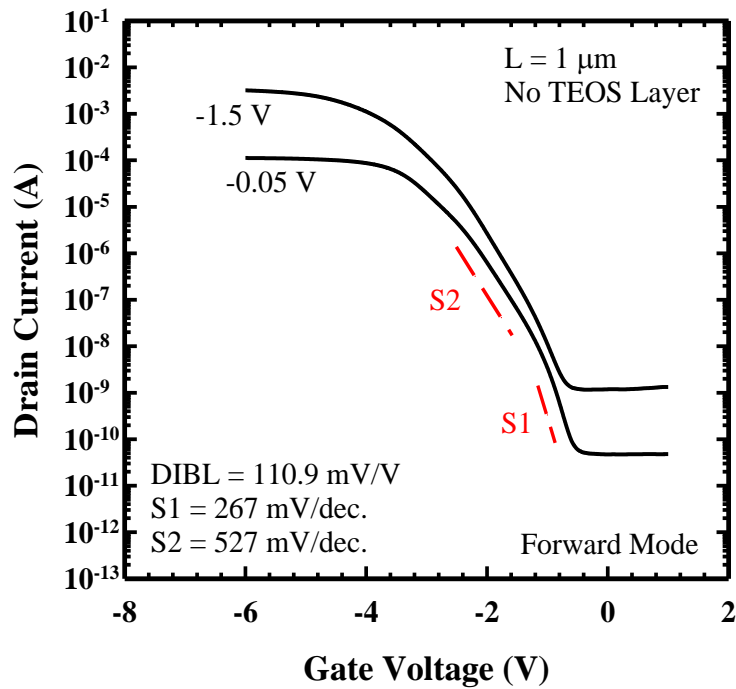
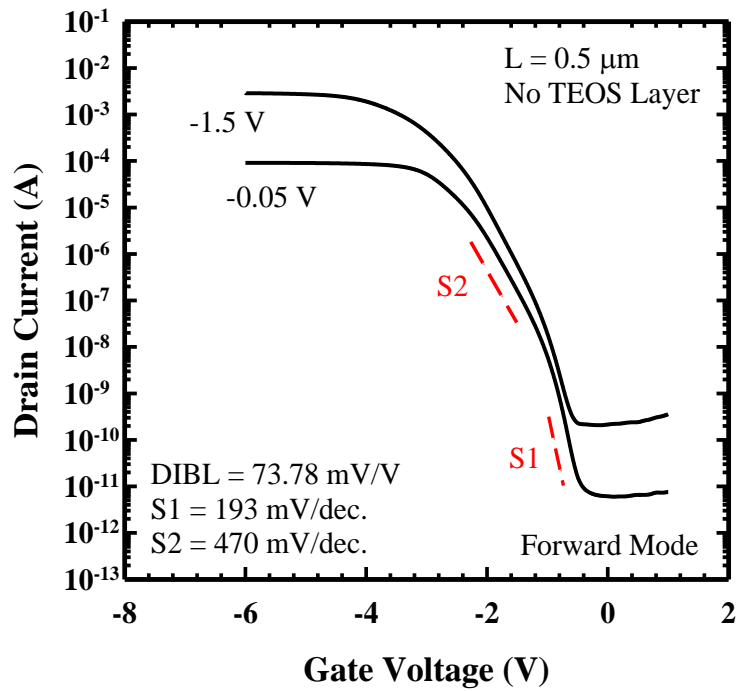


Figure 4.1. The bias configurations of our VMOS devices with no TEOS layer under the forward and reverse operation modes, respectively.



(b)

Figure 4.2.  $I_D$ - $V_G$  curves of VMOS devices under forward operation mode with nominal channel length of (a)  $0.5 \mu\text{m}$  and (b)  $1 \mu\text{m}$ .



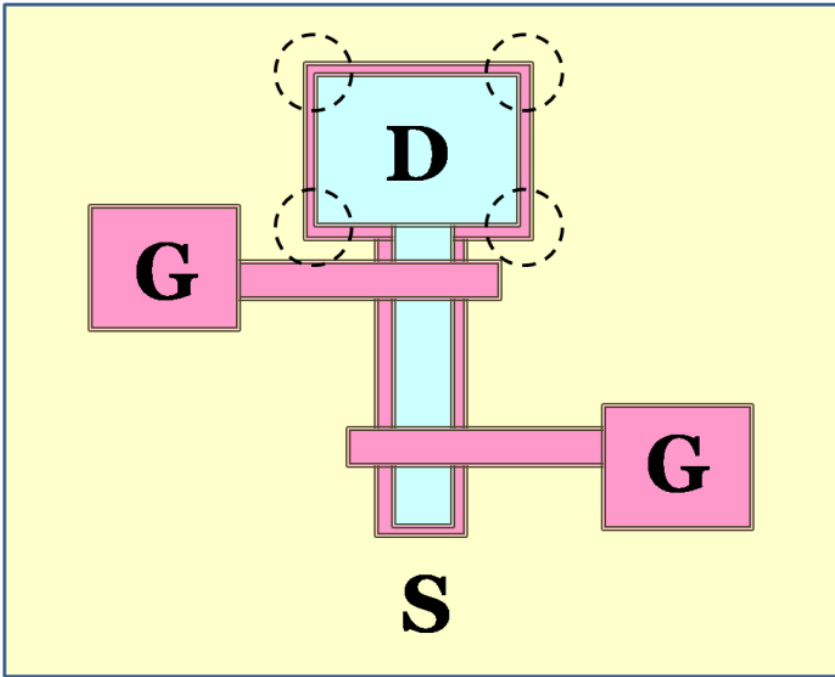


Figure 4.3. The top-view of the VMOS with convex corner regions circled.

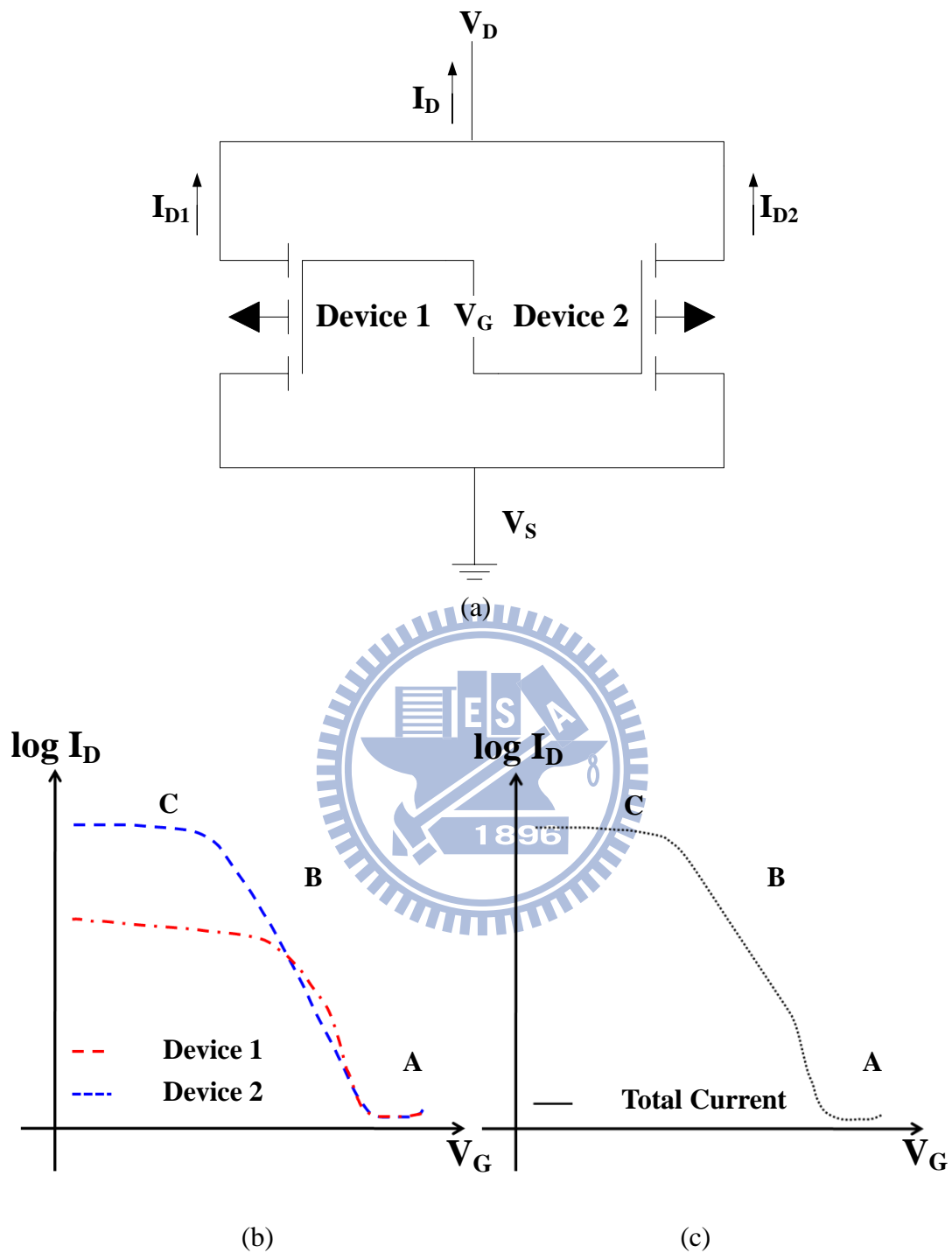
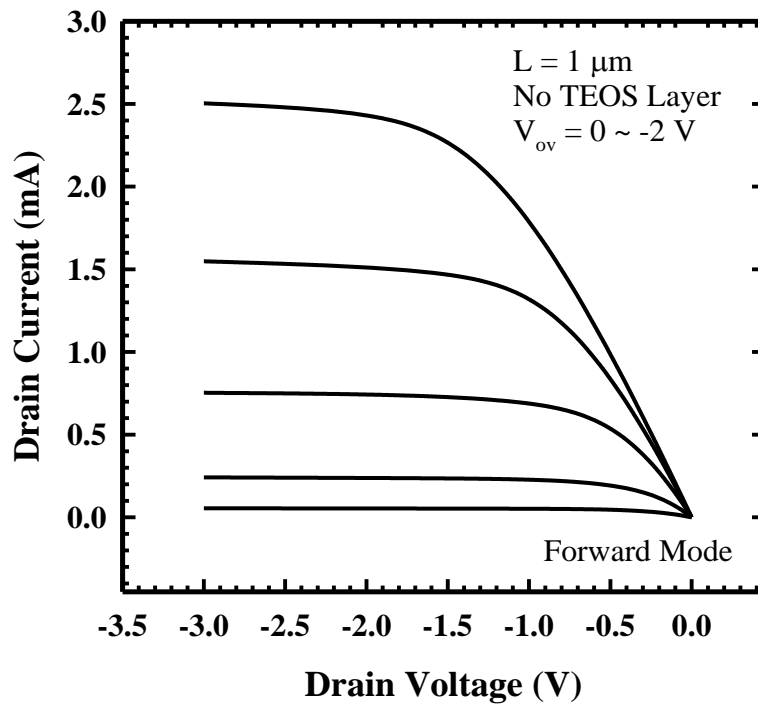
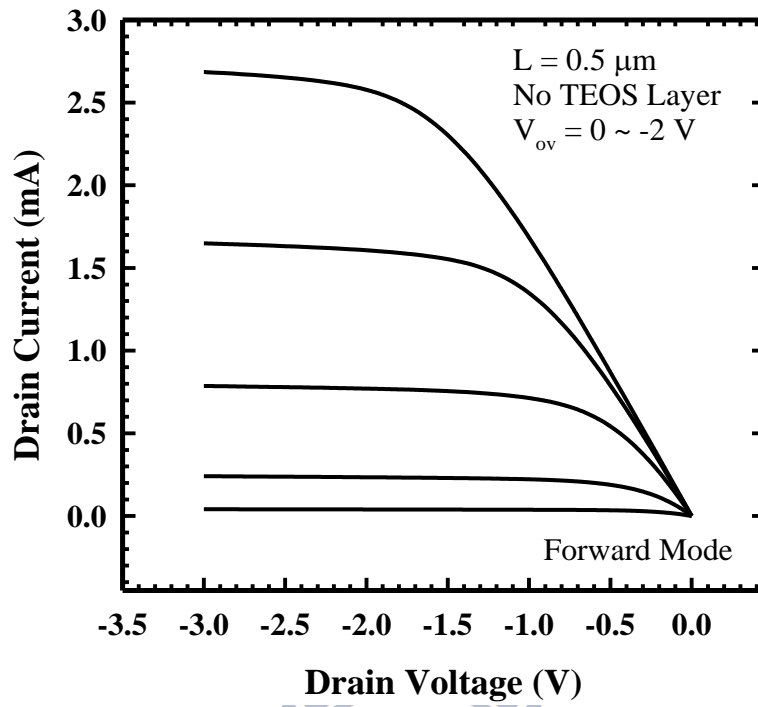


Figure 4.4. (a) The equivalent circuit of VMOS with two different MOSFETs in shunt. The device 1 is with a lower  $V_{th}$  and better S.S. than device 2. (b) The corresponding  $I_D$ - $V_G$  curves of these two shunted MOSFETs. (c)  $I_D$ - $V_G$  curves of the equivalent shunt circuit.



(b)

Figure 4.5. Output characteristics of the VMOS operated under forward mode with nominal channel length of (a)  $0.5 \mu\text{m}$  and (b)  $1 \mu\text{m}$ .

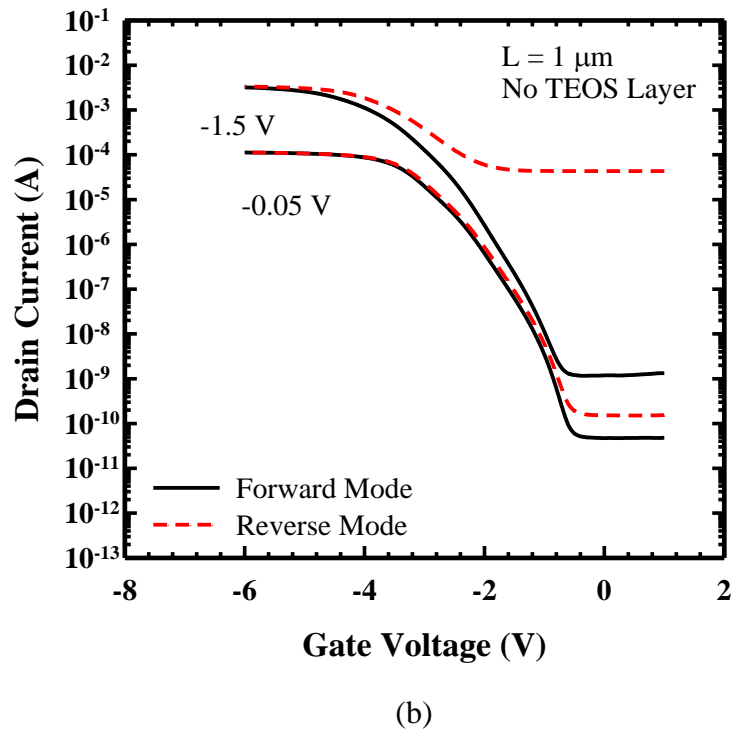
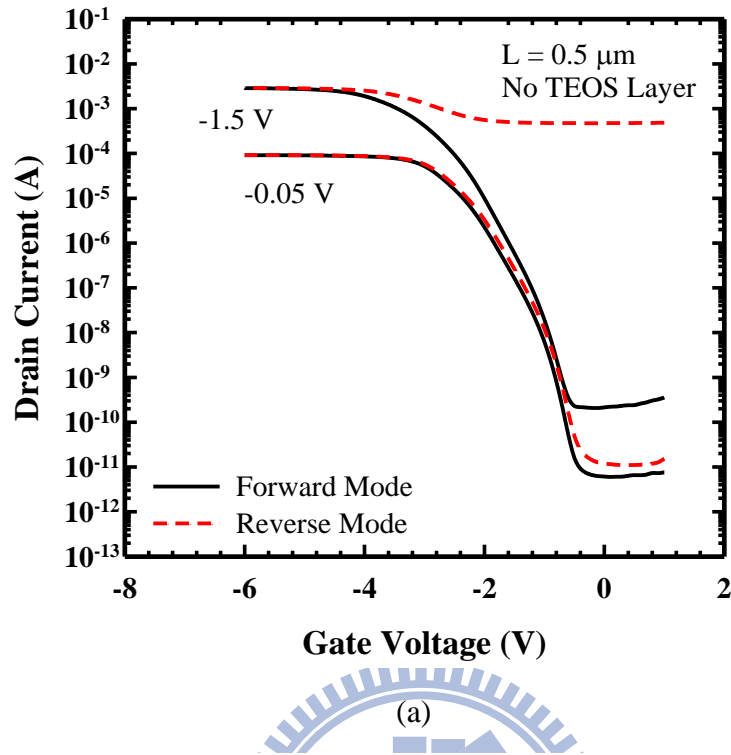
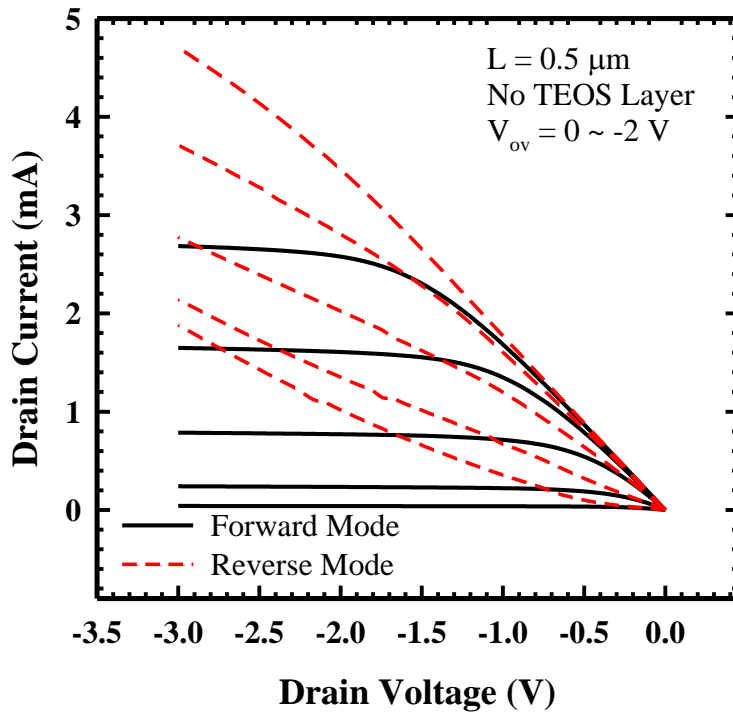
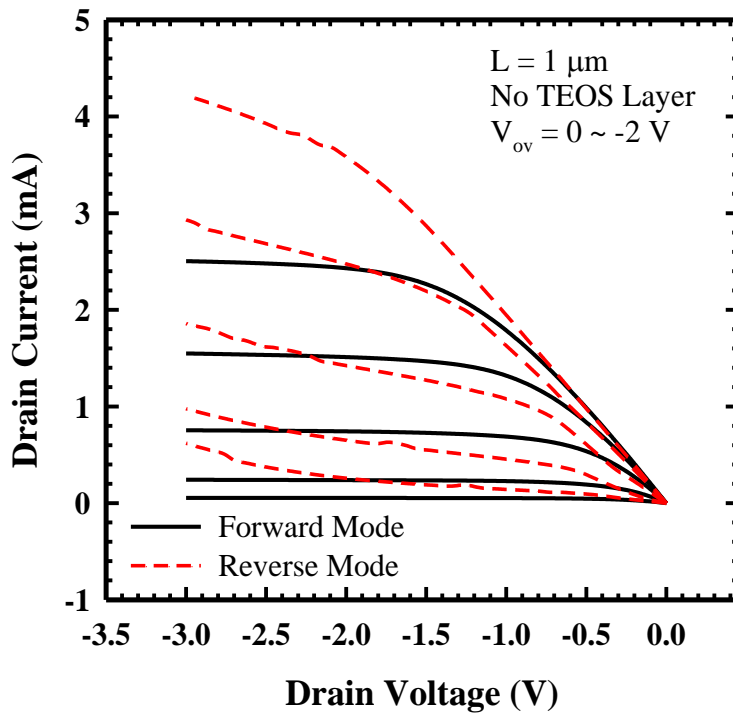


Figure 4.6.  $I_D$ - $V_G$  curves of VMOS devices under forward and reverse operation modes with nominal channel length of (a)  $0.5 \mu\text{m}$  and (b)  $1 \mu\text{m}$ .



(a)



(b)

Figure 4.7. Output characteristics of the VMOS operated under the forward and reverse modes with nominal channel length of (a)  $0.5 \mu\text{m}$  and (b)  $1 \mu\text{m}$ .

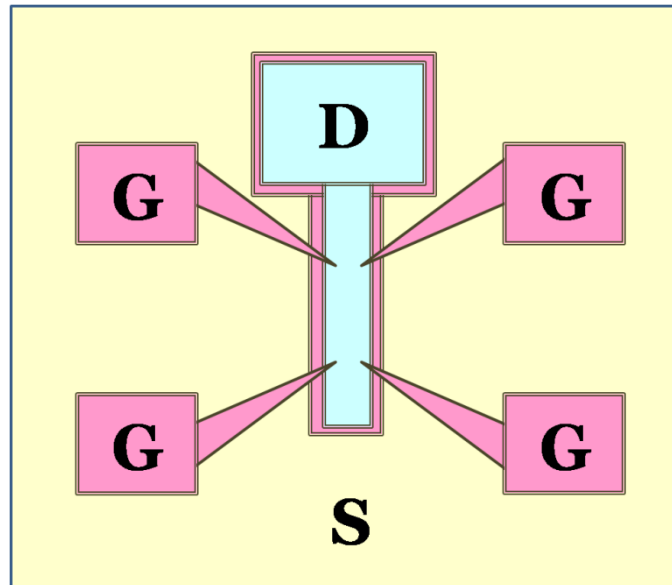


Figure 5.1. The top-view of modified SG-VMOS device layout.

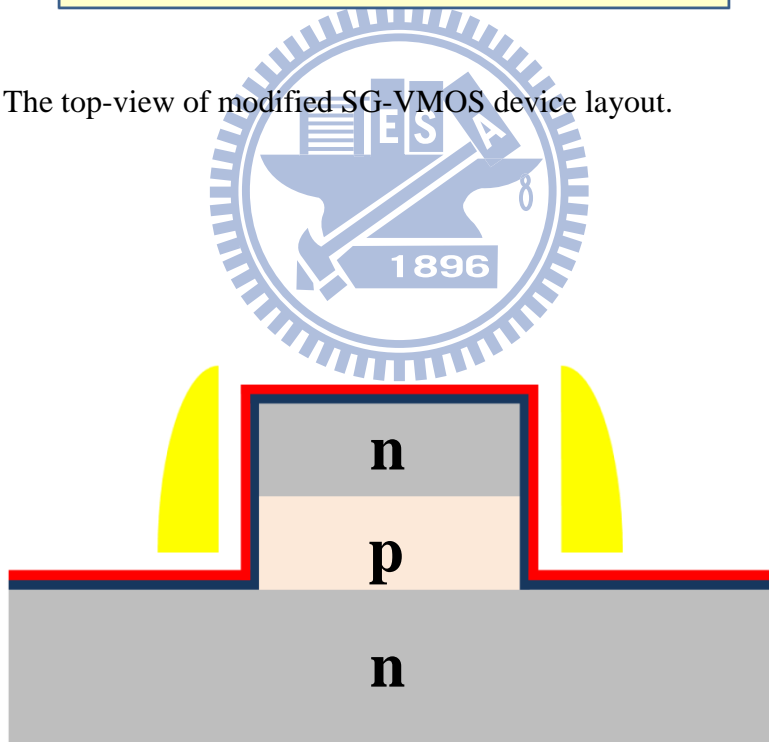


Figure 5.2. Schematic view of modified SG-VMOS device structure with epitaxial growth fabrication technique.

# Vita

姓 名： 許家維 Chia-Wei Hsu

性 別： 男

出 生： 西元 1986 年 03 月 22 日

出 生 地： 台灣 臺北市

住 址： 臺北縣新莊市龍安路266巷28號8樓

學 歷：

國立交通大學電子工程研究所 2008 年 9 月 ~ 2010 年 9 月

國立清華大學工程與系統科學系 2004 年 9 月 ~ 2008 年 6 月

國立新莊高級中學 2001 年 9 月 ~ 2004 年 6 月

臺北縣立福營國民中學 1998 年 9 月 ~ 2001 年 6 月

臺北縣立裕民國民小學 1992 年 9 月 ~ 1998 年 6 月



論文題目：

具懸浮奈米線結構之新穎元件的製作與特性分析

A Study on the Fabrication and Characterization of Novel Devices with  
Suspended Nanowire Structures

# *Publication List*

- [1] Chia-Hao Kuo, **Chia-Wei Hsu**, Hsing-Hui Hsu, Horng-Chih Lin, and Tiao-Yuan Huang, “Fabrication and analysis of various multiple-gated poly-Si nanowire thin-film transistors having identical channel shape,” *Symp. on Nano Device Technology (SNDT)*, May 4-5, 2010.
  
- [2] Chia-Hao Kuo, **Chia-Wei Hsu**, Hsing-Hui Hsu, Horng-Chih Lin, and Tiao-Yuan Huang, “Fabrication and analysis of thin film transistors with suspended nanowire channels,” *Int. Electron Devices and Materials Symp. (IEDMS)*, Nov 18-19, 2010.
  
- [3] **Chia-Wei Hsu**, Chia-Hao Kuo, Hsing-Hui Hsu, Horng-Chih Lin, and Tiao-Yuan Huang, “Fabrication and characterization of a novel suspended-nanowire-channel thin-film transistor with nanometer air gap,” submitted to *IEEE Int. Conf. on Nano/Micro Engineered and Molecular Systems (NEMS)*, 2011.

